Physico-chemical phenomena in soft monolayers: chiral recognition, microfluidics and protein interactions

Alba Pulido Companys

PHYSICO-CHEMICAL PHENOMENA IN SOFT MONOLAYERS: CHIRAL RECOGNITION, MICROFLUIDICS AND PROTEIN INTERACTIONS

Memòria que presenta *Alba Pulido Companys* per optar al títol de Doctora per la Universitat de Barcelona

Tesi doctoral dirigida per:

Dr. Jordi Ignés Mullol
Professor titular
Departament de Química Física
Universitat de Barcelona

Programa de doctorat:

Nanociències
Departament de Química Física
Facultat de Química, Universitat de Barcelona

Barcelona, març de 2014

Als meus padrins

CONTENTS

Chapter 4: Two-dimensional microfluidics

CHAPTER 1

INTRODUCTION

CHAPTER 1

INTRODUCTION

"Soft matter" or complex fluids are commonly used terms to refer to a large variety of systems involving polymers, colloids, gels, liquid crystals, surfactants, aggregating systems like micelles and vesicles, solutions of macromolecules, etc [1,2]. All these systems represent a field of study, soft materials science, which presents not only interesting challenges from a fundamental point of view, but also technological opportunities with applications in a wide range of disciplines [3-10].

In soft matter, building blocks self-assemble by means of weak intermolecular forces such as van der Waals, electrostatic, hydrophobic or hydrophilic interactions, hydrogen and coordination bonds, to spontaneously form ordered structures with different properties that can drastically change when a very mild change is introduced in the chemistry or conditions of the system [2,11]. This lability, when properly explored together with the selection and tailoring of the interactions involved in self-assembly, can lead to the design of structures with the desired pattern and functions.

Among all the soft matter systems mentioned above, one of the examples are the so-called Langmuir monolayers [12]. These date back to the early scientific experiments carried out by Benjamin Franklin (1774) on the effect of oily films on water, going through the ones performed by Agnes Pockels (1891) and Irving Langmuir (1917) that developed the experimental and theoretical concepts to understand the behaviour of molecules in insoluble monolayers. These systems, on which the present thesis is focused, are of current interest due to their relevance as two-dimensional model systems, and their applications in a wide range of scientific fields such as Nanotechnology, Biology, Chemistry or Physics [13-21]. The complex rheological properties of Langmuir monolayers is a subject of interest for the Physics community [22,23], with possible applications in medical science related to, for instance, the pulmonary surfactant layers and their viscoelastic rheological properties, which are of vital importance for the correct behaviour of the lung [24]. In the chemical context,

Langmuir monolayers are useful to study reactions in two dimensions like the one described by *M. Sastry et. al*. or *J. Jiang et. al*., where silver nanoparticles are synthesized [25,26]. In Biology, Langmuir monolayers are used as model systems for studying biomembranes [27], and finally, the transference of Langmuir monolayers onto a solid substrate (Langmuir-Blodgett films) offers a controlled method for building supramolecular assemblies with well defined molecular arrangement, creating structured materials that can be useful for optical [28], electronic [29], or biosensor applications [30].

In the following sections, Langmuir monolayers and some of their remarkable features for the purpose of this thesis will be discussed.

1.1 Langmuir monolayers

Certain organic molecules will adsorb and organize at the interface between a gaseous and a liquid phase (air/aqueous phase in the case of this thesis) to minimize their free energy, resulting in a monomolecular thick film called a Langmuir monolayer. These molecules are surfactants or amphiphiles, which are composed of two parts with different water affinity: a hydrophilic functional *head* group such as –COOH or -OH, and a hydrophobic *tail* generally involving one or more hydrocarbon chains [29]. This head-tail asymmetry is what makes these molecules to preferentially orient at the water surface, with the polar group immersed in the water subphase and the non-polar *tail* directed to the air. The balance between the water solubility and insolubility conferred to the molecule by this two differentiate parts is what determines whether a molecule will form insoluble monolayers [12].

In order to characterise the state of a Langmuir monolayer the following variables are used: surface pressure, π, molecular area, A, and temperature, T. The surface pressure is defined as the drop of the pure liquid surface tension when a monolayer is spread on its surface:

$$\pi = \gamma_0 - \gamma, \tag{1}$$

where γ_0 is the surface tension of the pure subphase liquid and γ is the surface tension of the monolayer-subphase system. The surface tension has force per unit length units, typically [mN m^{-1}], and the molecular area is defined as the surface occupied by one molecule, and has the units of [$Å^2$ $molecule^{-1}$].

When a monolayer-forming material is deposited on the surface of water, it spreads through the surface until π has risen to an equilibrium value. This *equilibrium spreading pressure* (π_e) is defined as that spontaneously generated when the bulk solid (the spreading material without a solvent) is placed in contact with a water surface, and is characteristic of the substances involved and the temperature [29]. At $\pi < \pi_e$, the monolayer is stable, but at $\pi > \pi_e$ the monolayer may collapse and the molecules reorganize through different collapse strategies such as forming three-dimensional agglomerates, flowing into the subphase, cracking, etc [31,12].

Once a known amount of material is spread on the surface of water and a monolayer is formed, it can be characterised by surface pressure (π) – molecular area (A) isotherms, obtained by compressing the monolayer and monitoring the different phase transformations it will undergo. These phase changes in analogy to 3D systems, reveal the existence of different states of aggregation that represent different degrees of molecular order resulting from the intermolecular forces in the Langmuir film and between monolayer and subphase [32].

An example of a compression isotherm is shown in Figure 1. The gaseous state of a monolayer is found at large molecular areas (in the range of hundreds of square angstroms per molecule), where the molecules are floating in the surface layer far enough to one another so that they barely interact. As the surface area of the monolayer is decreased, the hydrocarbon chains begin to interact and a phase change to a liquid expanded phase (LE) takes place. In the LE phase, the molecules are disordered with their chains randomly oriented and their polar head groups in contact with the subphase. As the molecular area is progressively reduced, a more condensed liquid phase appears (LC) with a higher degree of molecular order. This LC phase is reached after a first-order phase transition indicated by a *plateau* in the isotherm, and due to strong chain-chain interactions a closely packed arrangement of the molecules is obtained, where the hydrocarbon chains of the molecules are aligned parallel to one another but tilted with respect to the water surface [33]. As a result, this phase

features long-range orientational order of the molecules but sort-range positional order, and is characterised by a lower compressibility reflected in the isotherm by a nearly straight and very steep plot. Upon further compression, a second-order phase transition represented as a kink in the isotherm may be reached, leading to a solid phase (S) where the molecules are closely packed and untilted. This phase represents the highest packing degree a monolayer can stand before collapsing into three-dimensional structures that are usually irreversible [31].

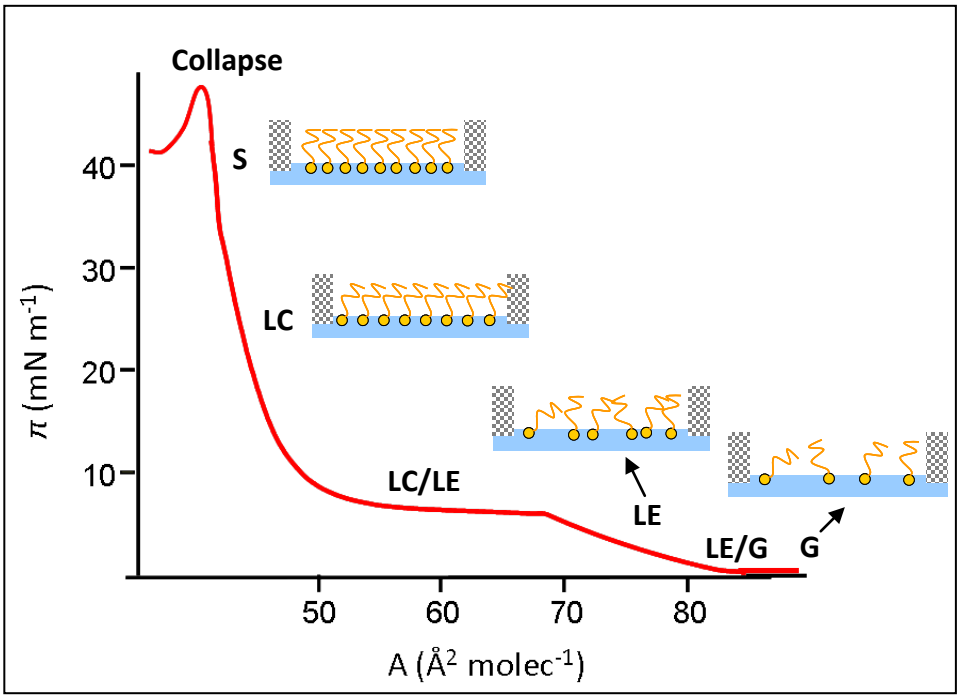

Figure 1. Conceptual π-A isotherm of a Langmuir monolayer showing the different states of molecular aggregation corresponding to different phases (G: gas, LE: liquid expanded, LC: liquid condensed, S: solid).

1.2 Chirality in Langmuir monolayers

An entity is said to be chiral when it is not superimposable to its mirror image. The two non-superimposable mirror image forms are called enantiomers in the case of molecules, and enantiomorphs in the case of macroscopic objects. In the absence of a chiral influence, if chiral substances are formed starting from achiral compounds, the product will always be obtained as a racemic mixture of the two enantiomers, that is, a 1:1 mixture of both enantiomers. Mirror-image symmetry breaking, making one of the

two enantiomers predominant, is a widely addressed phenomenon in soft-matter oriented research. It may result from several possible influences, such as the intervention of chiral chemical reagents or catalysts, or the action of a chiral physical force like a vortex motion [34-43].

Chirality, and in particular chirality in molecules of life, has attracted the interest of the scientific community during the last decades, fascinated by the origin of biological homochirality [44,45]. This absolute handedness of biomolecules is a fundamental question still not solved, and has been the motor of many investigations carried out in a two-dimensional environment [46-56]. Under these conditions, the generation and propagation of enantiomorphous structures appears to be relatively frequent since reduced dimensionality exclude some bulk symmetry elements enhancing chiral discrimination. In this context, metal surfaces have been chirally modified by adsorbed molecules to be used as heterogeneous catalysts for enantioselective reactions [57,58]. In the case of self-assembled supramolecular structures emerged at the air-liquid interface, the delicate balance of non-covalent interactions required to maintain these structures, makes them highly sensitive to chiral perturbations. Therefore, chirality has been induced and selected in these structures, and they have been used as templates for three-dimensional propagation through transference onto a solid support [59,60]. In particular, the study done by *Petit-Garrido et. al.* on the phenomenon of chiral selection in Langmuir monolayers, has been the starting point for chapter 3, where we extended the work to compounds of the same family.

1.3 Langmuir monolayers under flow conditions

The flow of Langmuir monolayers, represented as two-dimensional fluids with corresponding rheological properties, has been extensively studied from a theoretical as well as an experimental point of view. Interfacial hydrodynamics determines the behaviour of multiphase materials of large interfacial area such as foams and emulsions [61], involved in a wide range of applications going from food science to oil-

recovery technologies, and many industrial processes such as coating and spraying technologies [62,63].

In this context, the flow of a monolayer through a channel has been used to obtain viscoelastic parameters [64], or to determine its velocity profile [21, 65-68]. Specifically, *Schwartz* and *Knobler* worked with monolayers of tetradecanoic or pentadecanoic acid in a LE-LC phase flowing through a microchannel, to experimentally and quantitatively determine their velocity profile [20]. Later, *Stone* presented an exact solution for the velocity fields in the monolayer and subphase liquids, for the experiments reported by *Schwartz* and *Knobler*, suggesting that the obtained analytical solution could be used to determine the effective viscosity of the monolayer or the subphase [21].

On the other hand, the flow of Newtonian and non-Newtonian monolayers through a channel featuring abrupt changes in geometry, such as compression and expansion chambers, was used by *Fuller* and *Olson* to observe analogous behaviours between three-dimensional and two-dimensional systems. The authors demonstrated that the knowledge of the behaviour of bulk fluids can be used to understand and predict the flow behaviour of interfaces [69].

More recently, *Burriel et. al*. introduced a new system to gain control of laterally confined flows of monolayers, in order to extend the field of microfluidics into the two-dimensional scope of Langmuir monolayers and stimulate developments parallel to those in conventional microfluidics [70].

All the above mentioned works have been taken as a starting point for the development of the present thesis and specially chapter 4, which provides an extension of the newly introduced term “two-dimensional microfluidics”.

1.4 Langmuir monolayers as a model of biological membranes

The peculiar properties of the ubiquitous membranes of living organisms are fundamental to life processes. Since the early years of the first membrane models [71,72], insoluble monolayers have been considered good models of biomembranes, as they bear close resemblances in structure (Figure 2).

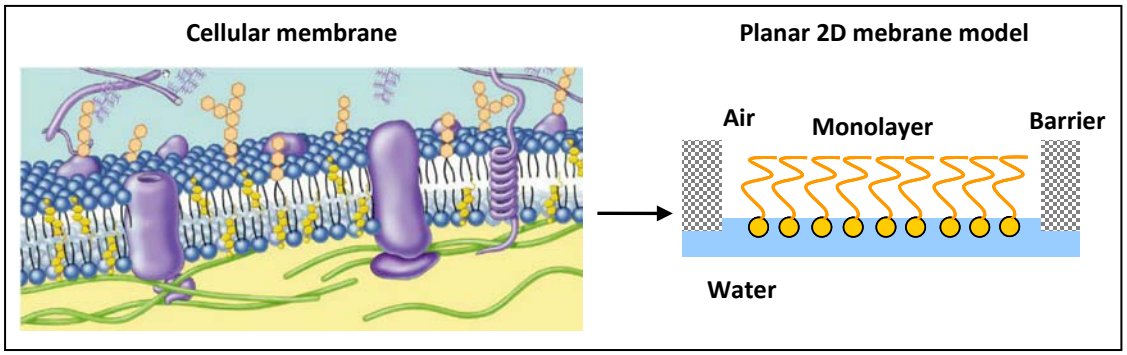

Figure 2. Representation of a cellular membrane [www.docstoc.com] (left), and planar lipid monolayer used as a biological membrane model (right).

During the last decades, the structure of Langmuir monolayers has been further characterised thanks to the advances occurred in interface sensitive techniques like X-Ray scattering, ellipsometry, fluorescence, Brewster Angle microscopy, etc. [73-78]. On the other hand, many biological membranes have unique functions that are not so well characterised, and their satisfactory performance is essential to the maintenance of life [79,80]. This has reemphasized the applicability of monolayer models in understanding those functions and processes occurring at the biological membranes [81, 82].

Some of the most commonly studied biomolecular interactions in Langmuir monolayers involve the interactions of lipids with DNA, peptides, proteins, nanoparticles, polymers, drugs, and hormones. In this sense, Langmuir monolayers allow to study the coupling of DNA to cationic lipids, which is a key step for the development of DNA-based pharmaceuticals for gene therapy, bio-sensors and nano-devices [83-86]. In the context of lipid-peptide interactions, phospholipid monolayers have been intensively used to model the eukaryotic cell membrane (generally using phosphatidylcholines, sphingomyelines and cholesterol) and the cytoplasmic bacterial membrane (combining phosphatidylglycerols and cardiopilin) [87]. In this way, the mechanism of interaction between amphipatic antimicrobial peptides and cellular membranes has been examined, since these peptides constitute interesting structures for the development of new drugs, complementing or even enhancing the standard antibiotic therapies [88]. Another use of Langmuir monolayers as model for biological membranes consists in investigating the changes in the organisation of lipids in the

monolayer produced by lipid-protein interactions [89]. In this context, for example, the mechanism of interaction of Tau protein with two-dimensional model membranes was recently investigated, since the role played by the cell membrane on inducing protein aggregation and membrane permeabilization has strong implications, for instance, in Alzheimer's disease [90]. Finally, the interactions of the cell membrane with hormones and newly synthesized drugs, as well as with new biocompatible nanoparticles and polymers for future biomedical applications, has received increased attention during the last years [92-98].

Chapter 5 of this thesis is devoted to the interaction of the myristoylated unique domain of the Src protein with phospholipid monolayers. The altered activity of Src is related with cancer development in humans [91], and we still have an incomplete picture of how the diverse aspects of cell behaviour that are controlled by Src might contribute to the development of cancer. For this reason, Src has been extensively studied during the last decades.

1.5 Objectives

The objectives of the present thesis can be summarized as follows:

1. Characterisation of Langmuir monolayers of an azobenzene derivative, and verification of the induction and selection of chirality in condensed domains by the use of a chemical and a physical chiral force that was previously reported for an analogous compound.

2. Study of heterochiral recognition in monolayers by means of the interaction of two enantiomeric chiral azobenzene derivative surfactants.

3. Use two-dimensional microfluidics to explore different transport processes occurring at the interface between two coflowing monolayers.

4. Study the formation of anomalous velocity profiles during channel flow of monolayers. Characterize subphase backflow, an unresolved issue present at the microfluidic channels, and relate it to the flow profiles.

5. Adapt the protocols used in two-dimensional microfluidics to study the insertion and diffusion of a protein in a phospholipid monolayer.

1.6 References

[1] M. Kleman, O. D. Lavrentovich. *Soft Matter Physics: An Introduction*. Springer, New York (2003).

[2] P. G. de Gennes. *Science*, **256**, 495-497 (1992).

[3] J. M. Lehn. *Science*, **295**, 2400-2403 (2002).

[4] D. Clery, M. Lavine. *Science*, **297**, 961 (2002).

[5] M. L. Carot, V. A. Macagno, P. Paredes-Olivera, E. M. Patrito. *J. Phys. Chem. C*, **111**, 4294-4304 (2007).

[6] M. El Garah, F. Palmino, F. Cherioux. *Langmuir*, **26** (2), 943-949 (2010).

[7] A. Ulman. *Chem. Rev*., **96**, 1533 (1996).

[8] J. C. Love, L. A. Estroff, J. K. Kriebel, R. G. Nuzzo, G. M. Whitesides. *Chem. Rev*., **105**, 1103 (2005).

[9] P. Samori, V. Francke, K. Müllen, J. P. Rabe. *Chem.-Eur. J.*, **5**, 2312 (1999).

[10] D. Philip, J. F. Stoddart. *Angewandte Chemie International Edition*, **35**, 1154 (1996).

[11] G. M. Whitesides, B. Grzybowski. *Science*, **295**, 2418-2421 (2002).

[12] G. L. Gaines Jr. *Insoluble Monolayers at Liquid-Gas Interfaces*. Interscience, New York (1966).

[13] G. Brezesinski, H. Möhwald. *Advances in Colloid and Interface Science*, **100-102**, 563-584 (2003).

[14] H. Möhwald. *Annual Review of Physical Chemistry*, **41**, 441 (1990).

[15] H. M. McConnell. *Annual Review of Physical Chemistry*, **42**, 171 (1991).

[16] C. M. Knobler. *Annual Review of Physical Chemistry*, **43**, 207 (1992).

[17] J. K. Kumar, J. S. Oliver. *Journal of the American Chemical Society*, **127**, 11307-11314 (2002).

[18] Y. Tabe, H. Yokoyama. *Langmuir*, **11**, 4609-4613 (1995).

[19] J. Claret, J. Crusats, R. Albalat, J. Ignés-Mullol, H. Martínez-Seara, R. Reigada, F. Sagués. *European Physical Journal E*, **21**, 111-116 (2006).

[20] D. K. Schwartz, C. M. Knobler. *Physical Review Letters*, **73** (21), 2841-2844 (1994).

[21] H. A. Stone. *Physical Fluids*, **7** (12), 2931-2937 (1995).

[22] J. Ignés-Mullol, J. Claret, R. Reigada, F. Sagués. *Physics Reports*, **448**, 163-179 (2007).

[23] J. Ignés-Mullol, D. K. Schwartz. *Nature*, **410**, 348-351 (2001).

[24] R. Wüstneck, J. Perez-Gil, N. Wüstneck, A. Cruz, V. B. Fainerman, U. Pison. *Advances in Colloid and Interface Science*, **117**, 33-58 (2005).

[25] A. Swami, P. R. Selvakannan, R. Pasricha, M. Sastry. *J. Phys. Chem. B.*, **108**, 19269-19275 (2004).

[26] H. G. Liu, F. Xiao, C. W. Wang, Y. I. Lee, Q. Xue, X. Chen, D. J. Qian, J. Hao, J. Jiang. *Nanotechnology*, **19**, 055603 (2008).

[27] A. Radhakrishnan, T. G. Anderson, H. M. McConnell. *PNAS*, **97** (23), 12422-12427 (2000).

[28] M. Ferreira, C. A. Olivati, A. M. Machado, A. M. Assaka, J. A. Giacometti, L. Akcelrud, O. N. Oliveira Jr. *Journal of Polymer Research*, **14**, 39-44 (2007).

[29] M. C. Petty. *Langmuir-Blodgett Films: An Introduction*. Cambridge University Press, United States (1996).

[30] F. Davis, S. P. J. Higson. *Biosensors and Bioelectronics*, **21**, 1-20 (2005).

[31] K. Y. C. Lee. *Annual Review of Physical Chemistry*, **59**, 771-791 (2008).

[32] V. M. Kaganer, H. Möhwald, P. Dutta. *Reviews of Modern Physics*, **71** (3), 779-819 (1999).

[33] P. Dutta. *Colloids and Surfaces A: Physicochemical and Engineering Aspects*, **171**, 59-63 (2000).

[34] J. M. Ribó, J. Crusats, F. Sagués, J. Claret, R. Rubires. *Science*, **292**, 2063-2066 (2001).

[35] R. Rubires, J. A. Farrera, J. M. Ribó. *Chemistry- A Euroopean Journal*, **7**, 436-446 (2001).

[36] J. M. Ribó, J. Crusats, J. A. Farrera, M. L. Valero. *Journal of the Chemical Society, Chemical Communications*, 681-682 (1994).

[37] R. Rubires, J. Crusats, Z. El-Hachemi, T. Jaramillo, M. López, E. Valls, J. A. Farrera, J. M. Ribó. *New Journal of Chemistry*, 189-198 (1999).

[38] J. Crusats, J. Claret, I. Díez-Pérez, Z. El-Hachemi, H. García-Ortega, R. Rubires, F. Sagués, J. M. Ribó. *Chemical Communications*, 1588-1589 (2003).

[39] C. Escudero, J. Crusats, I. Díez-Pérez, Z. El-Hachemi, J. M. Ribó. *Angewandte Chemie Internacional Edition,* **45**, 8032-8035 (2006).

[40] J. Crusats, Z. El-Hachemi, J. M. Ribó. *Chemical Society Reviews*, **39**, 569-577 (2010).

[41] T. Yamaguchi, T. Kimura, H. Matsuda, T. Aida. *Angewandte Chemie Internacional Edition*, **43**, 6350-6355 (2004).

[42] A. Tsuda, Md. A. Alam, T. Harada, T. Yamaguchi, N. Ishii, T. Aida. *Angewandte Chemie Internacional Edition*, **46**, 8198-8202 (2007).

[43] M. Wolffs, S. J. George, Z. Tomovic, S. C. J. Meskers, A. P. H. J. Schenning, E. W. Meijer. *Angewandte Chemie International Edition*, **46**, 8203-8205 (2007).

[44] L. D. Barron. *Space Science Reviews*, **135**, 187-201 (2008).

[45] A. Guijarro, M. Yus. *The Origin of Chirality in the Molecules of Life: a revision fromawarness to the current theories and perspectives of this unsolved problem*. Royal Society of Chemistry (2009).

[46] N. Nandi, D. Vollhardt. *Chemical Reviews*, **103**, 4033-4075 (2003).

[47] H. Zepik, E. Shavit, M. Tang, T. R. Jensen, K. Kjaer, G. Bolbach, L. Leiserowitz, I. Weissbuch, M. Lahva. *Science*, **295**, 1266-1269 (2002).

[48] C. J. Eckhardt, N. M. Peachey, D. R. Swanson, J. M. Takacs, M. A. Khan, X. Gong, J. H. Kim, J. Wang, R. A. Uphaus. *Nature*, **362**, 614 (1993).

[49] R. Viswanathan, J. A. Zasadzinskl, D. K. Schwartz. *Nature*, **368**, 440-443 (1994).

[50] X. Huang, C. Li, S. Jiang, X. Wang, B. Zhang, M. Liu. *Journal of the American Chemical Society*, **126**, 1322-1323 (2004).

[51] P. Guo, L. Zhang, M. Liu. *Advanced Materials*, **18**, 177-180 (2006).

[52] P. Yao, H. Wang, P. Chen, X. Zahn, X. Kuang, D. Zhu, M. Liu. *Langmuir*, **25** (12), 6633-6636 (2009).

[53] P. Chen, X. Ma, K. Hu, Y. Rong, M. Liu. *Chemistry – A European Journal*, **17**, 12108-12114 (2011).

[54] N. Petit-Garrido, J. Ignés-Mullol, J. Claret, F. Sagués. *Physical Review Letters*, **103**, 2377802 (2009).

[55] N. Petit-Garrido, J. Claret, J. Ignés-Mullol, F. Sagués. *Chemistry-A European Journal*, **18**, 3975-3980 (2012).

[56] N. Petit-Garrido, J. Claret, J. Ignés-Mullol, F. Sagués. *Nature Communications*, **3**, 1001 (2012).

[57] M. Ortega-Lorenzo, S. Haq, T. Bertrams, P. Murria, R. Raval, C. J. Baddeley. *Journal of Physical Chemistry B*, **103**, 10661 (1999).

[58] R. Raval, C. J. Baddeley, S. Haq, S. Louafi, P. Murray, C. Muryn, M. Ortega Lorenzo, J. Williams. *Studies in Surface Science and Catalysis*, **122**, 11-22 (1999).

[59] I. Kuzmenko, H. Papaport, K. Kjaer, J. Als-Nielsen, I. Weissbuch, M. Lahav, L. Leiserowitz. *Chemical Reviews*, **101**, 1659-1696 (2001).

[60] N. Petit-Garrido, R. P. Trivedi, J. Ignés-Mullol, J. Claret, C. Lapointe, F. Sagués, I. I. Smalyukh. *Physical Review Letters*, **107**, 177801 (2011).

[61] D. A. Edwards, H. Brenner, D. T. Wasan. *Interfacial Transport Processes and Rheology*. Butterworth-Heinemann, Stoneham, MA, 1991.

[62] E. Van der Linden, L. Sagis, P. Venema. *Curr. Opin. Colloid Interface Sci*., **8**, 349-358 (2003).

[63] U. Oxaal, M. Murat, F. Boger, A. Aharony, J. Feder, T. Jossang. *Nature*, **329**, 32-37 (1987).

[64] M. Sacchetti, H. Yu, G. Zografi. *J. Chem. Phys*., **99**, 563 (1993).

[65] P. Burriel, J. Claret, J. Ignés-Mullol, F. Sagués. *Physical Review Letters*, **100**, 134503 (2008).

[66] D. K. Schwartz, C. M. Knobler, R. Bruinsma. *Physical Review Letters*, **73**, 2841 (1994).

[67] M. L. Kurnaz, D. K. Schwartz. *Physical Review E*, **56**, 3378 (1997).

[68] A. Ivanova, M. L. Kurnaz, D. K. Schwartz. *Langmuir*, **15**, 4622 (1999).

[69] D. J. Olson, G. G. Fuller. *Journal of Non-Newtonian Fluid Mechanics*, **89**, 187-207 (2000).

[70] P. Burriel, J. Ignés-Mullol, J. Claret, F. Sagués. *Langmuir*, **26** (7), 4613-4615 (2010).

[71] Görter, F. Grendel. *J. Exp. Med*., **41**, 439 (1925).

[72] S. J. Singer, G. L. Nicolson. *Science*, **175**, 720-731 (1972).

[73] K. Kjaer, J- Als-Nielsen, C. A. Helm, L. A. Laxhuber, H. Möhwald. *Physical Review Letters*, **58**, 2224-2227 (1987).

[74] P. Dutta, J. B. Peng, B. Lin, J. B. Ketterson, M. Prakash, P. Georgopoulos, S. Ehrlich. *Physical Review Letters*, **58**, 2228-2231 (1987).

[75] R. Reiter, H. Motschmann, H. Orendi, A. Nemetz, W. Knoll. *Langmuir*, **8**, 1784-1788 (1992).

[76] M. Lösche, E. Sackmann, H. Möhwald. *Ber Bunsenges Phys. Chem*., **87**, 848-852 (1983).

[77]S. Henon, J. Meunier. *Rev. Sci. Insrtum*., **62**, 936-939 (1991).

[78] D. Hönig, D. Möbius. *J. Phys. Chem*., **95**, 4590-4592 (1991).

[79] H. Davson, J. F. Danielli. *Permeability of Natural Membranes*, Cambridge University Press, Second Edition (1952).

[80] Society for Exptl. Biology Symposium Nº8, *Active Transport and Secretion*, Academic Press, New York (1954).

[81] M. Blank. *J. Phys. Chem*., **66**, 1911 (1962).

[82] C. Stefaniu, G. Brezesinski, H. Möhwald. *Advances in Colloid and Interface Science*, doi:10.1016/j.cis.2014.02.013 (2014).

[83] M. N. Antipina, I. Schulze, M. Heinze, B. Dobner, A. Langner, G. Brezesinski. *ChemPhysChem*, **10**, 2471-2479 (2009).

[84] M. Heinze, G. Brezesinski, B. Dobner, A. Langner. *Bioconjugate Chem*., **21**, 696-708 (2010).

[85] M. Dittrich, M. Böttcher, J. S. L. Oliveira, B. Dobner, H. Möhwald, G. Brezesinski. *Soft Matter*, **7**, 10162-10173 (2011).

[86] I. Sigal-Batikoff, O. Konovalov, A. Singh, A. Berman. *Langmuir*, **26**, 16424-16433 (2010).

[87] K. Lohner. *Development of Novel Antimicrobial Agents: Emerging Strategies*. Norfolk: Horizon Scientific Press (2001).

[88] O. G. Travkova, J. Andrä, H. Möhwald, G. Brezesinski. *Langmuir*, **29**, 12203-12211 (2013).

[89] E. B. Watkins, C. E. Miller, J. Majewski, T. L. Kuhl. *P. Natl. Acad. Sci. USA*, **108**, 6975-6980 (2011).

[90] E. M. Jones, M. Dubey, P. J. Camp, B. C. Vernon, J. Biernat, E. Mandelkow, J. Majewski, E. Y. Chi. *Biochemistry*, **51**, 2539-2550 (2012).

[91] M. C. Frame. *Biochimica et Biophysica Acta*, **1602**, 114-130 (2002).

[92] C. Stefaniu, G. Brezesinski, H. Möhwald. *Soft Matter*, **8**, 7952-7959 (2012).

[93] D. L. Leiske, B. Meckes, C. E. Miller, C. Wu, T. W. Walker, B. H. Lin, M. Meron, H. A. Ketelson, M. F. Toney, G. G. Fuller. *Langmuir*, **27**, 11444-11450 (2011).

[94] B. Grazyl-Malcher, M. Filek, G. Brezesinski. *Langmuir*, **25**, 13071-13076 (2009).

[95] M. Lucio, F. Bringezu, S. Reis, J. L. F. C. Lima, G. Brezesinski. *Langmuir*, **24**, 4132-4139 (2008).

[96] M. Broniatowski, M. Flasinski, P. Wydro. *Journal of Colloids and Interface Science*, **381**, 116-124 (2012).

[97] A. A. Torrano, A. S. Pereira, O. N. Oliveira Jr, A. Barros-Timmons. *Colloids and Surfaces B: Biointerfaces*, **108**, 120-126 (2013).

[98] F. N. Zakanda, L. Lins, K. Nott, M. Paquot, G. M. Lelo, M. Deleu. *Langmuir*, **28**, 3524-3533 (2012).

CHAPTER 2

IMAGING TECHNIQUES

SECTION 2.1

BREWSTER ANGLE MICROSCOPY (BAM)

2.1.1 Principles of the Brewster Angle Microscopy

Brewster Angle Microscopy allows the *in situ* study of thin films lying on an interface [1,2]. It is based on the Brewster law, which states that for every interface between two dielectric mediums there is a characteristic angle, the Brewster angle (θ_B), where only the light polarised perpendicularly to the plane of incidence is reflected (the plane of incidence contains the incident beam, the reflected beam and the normal to the interface). Figure 1 shows the Brewster angle between the incident light and the surface normal, and illustrates the light polarisation phenomenon occurring to the reflected beam. The electric field vectors in the incident light vibrate in all planes perpendicular to the direction of propagation, although only two vector vibrations are represented in Figure 1, and the reflected ray electric vectors are oriented parallel to the surface and perpendicular to the plane of incidence.

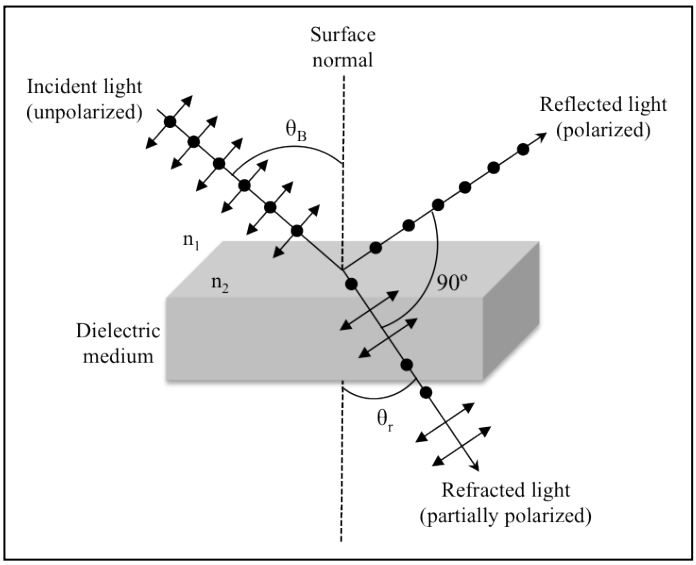

Figure 1. Representation of the reflected light polarisation when light is striking at the Brewster angle in a dielectric medium.

The reflectivity of light from an interface depends on the polarisation and the angle of incidence of the incident light. For a Fresnel interface (an ideal flat interface for which the refractive index changes abruptly from the refractive index of the upper phase, to the refractive index of the lower phase), when the incident ray is p-polarised (in the plane of incidence) and striking at the Brewster Angle, reflectivity vanishes (see Figure 2). For real interfaces, where the refractive index does not change abruptly and which are more or less rough, the reflection is minimum at the Brewster angle but does not vanish [3].

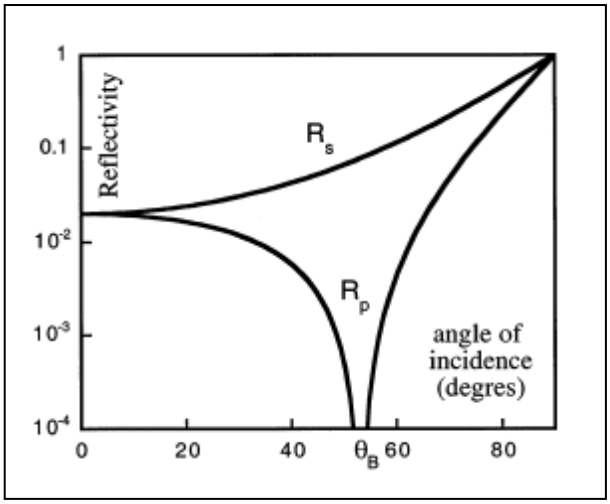

Figure 2. Reflectivity of a Fresnel interface between air and water (refractive indexes n=1 and n=1.33 respectively), for the polarisation p (Rp, in the plane of incidence), and the polarisation s (Rs, perpendicular to the plane of incidence). At the Brewster angle θ_B and for p-polarised light, the reflectivity vanishes. [3]

Taking into account the above described system, the Fresnel equation for the reflectivity of p-polarised light (1), and the Snell's equation (2),

$$R_p = \left(\frac{\tan(\theta_i - \theta_r)}{\tan(\theta_i + \theta_r)} \right)^2 \quad (1)$$

$$n_1 \sin\theta_i = n_2 \sin\theta_r \quad (2)$$

one can obtain a relation between the refractive indexes of the two media, and determine the Brewster angle.

In the equations above, θ_i is the angle of incidence, θ_r is the angle of refraction, n_1 is the refractive index of the first medium and n_2 is the refractive index of the second medium. The Brewster angle is the angle at which R_P decreases and reaches a minimum value, and the condition for that is $(\theta_i + \theta_r) = \pi/2$ according to equation (1). Writing θ_r in terms of θ_i , one can obtain an incident angle at which no light is reflected, the Brewster angle θ_B , and substituting $\theta_r = 90 - \theta_B$ in equation (2), and after rearrangement,

$$\theta_B = \arctan\left(\frac{n_2}{n_1}\right) \tag{3}$$

when the refractive indexes of the two media are known, the Brewster angle can be easily determined. For the case of an air-water interface, which is the common system used in Langmuir monolayers, the Brewster angle is 53.2° at 20°C.

Experimentally, the BAM uses incident linearly p-polarised light at the Brewster angle to obtain images of an interface. In this configuration, when the incident light is directed towards a clean water surface, reflectivity vanishes and this results in an image showing a dark background. When a surfactant monolayer is spread on the air-water interface, a layer of a different refractive index is introduced in the path of light, breaking the no-reflection condition and giving well-contrasted images showing distinguishable structures formed by the monolayer (Figure 3). Moreover, the difference in reflectivity between a two-dimensional gaseous phase and a condensed phase of a Langmuir monolayer is high enough to be detected. In fact, reflectivity changes depending on the layer thickness, the aggregation state of the monolayer and the molecular orientation of the birefringent medium forming the monolayer, giving rise to images showing a grey level or reflectivity distribution (see figure 3C).

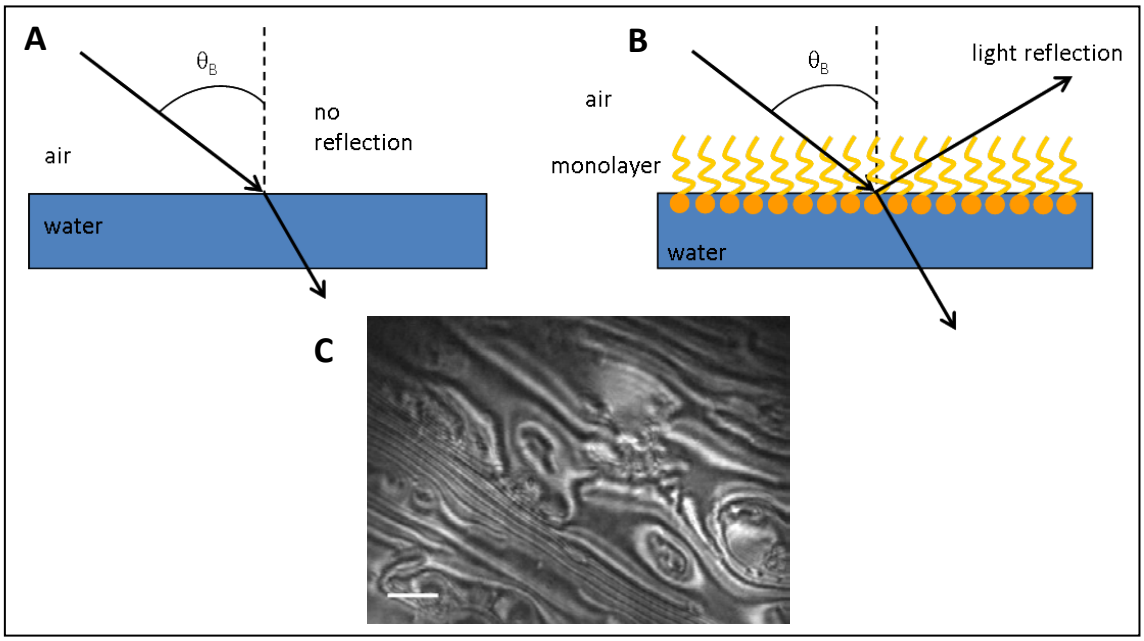

Figure 3. (A) A clean water surface is illuminated with linearly p-polarised light at the Brewster angle and no light is reflected. (B) A monolayer spread on the surface of water breaks the no-reflection condition. (C) Example of a BAM image of the surfactant *trans* 8Az5COOH monolayer (see chapter 3) at low surface pressure and T=30°C. Ruler is 100µm long.

2.1.2 Components of a Brewster Angle Microscope

The light used in a Brewster Angle Microscope has to come from a laser beam, in order to satisfy the following requirements:

- High intensity (> 25mW), since the reflectivities involved are very small.
- Monochromatic, since n_1 and n_2 depend on the wavelength, and we need to have a well-defined θ_B value.
- Collimated: the beam must have a well-defined direction (parallel beam).
- Linearly p-polarised, in order to achieve a minimum of reflected light on clean water, at the Brewster angle. A polariser placed on the beam trajectory is used to provide the required p-polarised light.
- Appropriate beam size (1-5 mm^2), to perfectly illuminate the observation area.

The light coming from the source, which is parallel, monochromatic and p-polarised after crossing a polariser, is directed to the surface of water (which is the subphase used in this thesis), at the Brewster angle. The reflected beam is captured by the microscope objective (f~40 mm), which plays an important role in determining the resolution of the obtained images. Then, an analyser may be placed after the objective in order to select the s-polarised reflected light, allowing to detect the optical anisotropy in the monolayer due to the molecular tilt or the molecular organisation. Finally, the selected light is sent to a charge-coupled device (CCD) camera, to capture the images. In order to avoid the saturation of the signal due to an excess of stray light, a non-reflecting glass plate is laid inside the subphase where the laser spot illuminates, to absorb the refracted beam light and to prevent it to reach the detector. To facilitate the instrument alignment, a mirror may be used to combine the incident and the reflected beam into a single optical arm (Figure 4).

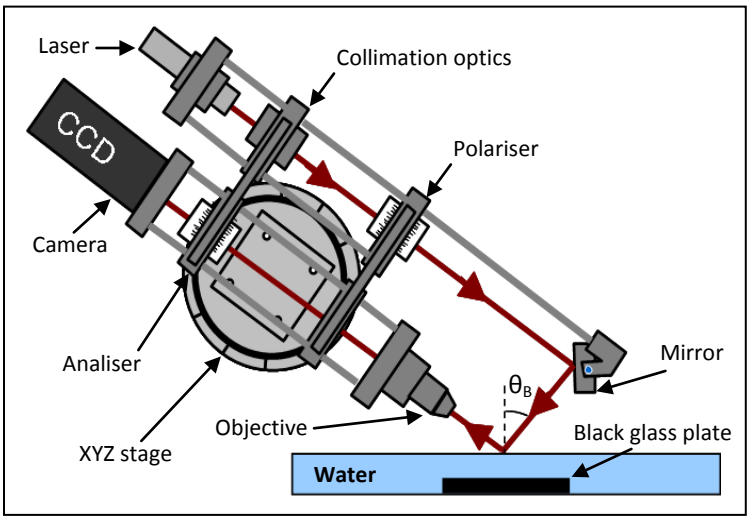

Figure 4. Schematics of a Brewster Angle Microscope. Red arrows indicate the trajectory of the laser beam.

One of the limitations of the BAM image quality, apart from the parasite light coming from the scattering created by the optics present on the trajectory of the beam, and that would result in a loss of contrast in the images, is the inclined position of the microscope. As a consequence, only a small strip of the surface is in focus, since the focal plane of the objective does not coincide with the water surface. To overcome such limitation, the instrument is equipped with an XY translation stage to be able to scan the monolayer and bring into focus the whole field of view.

2.1.3 Quantitative analysis of the BAM images

As mentioned above, BAM images show a grey level distribution that can be correlated to the reflectivity, which depends on different material parameters such as the tilt angle of the molecules (inclination), θ, the azimuthal angle (orientation), ϕ (Figure 5), thickness of the monolayer, and instrumental parameters like the orientation of the analyser.

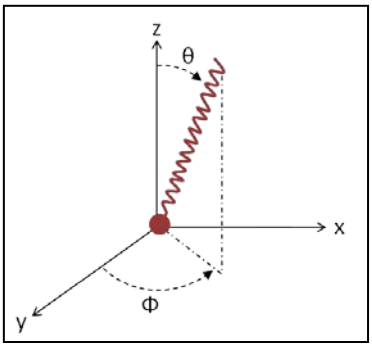

Figure 5. Schematic representation of the orientation of an amphiphilic molecule at the air-water interface.

It is assumed that for a CCD camera there is a linear dependence between the observed grey level and the intensity of light, according to:

$$Grey\ level = R_O + \Delta R \times I(\theta, \phi, thickness, instrumental\ parameters\ldots), \quad (4)$$

where R_0 and ΔR are unknown constants and I is the reflectivity function that can be obtained analytically [4]. Equation (4) is especially useful for the analysis of Langmuir monolayers presenting highly symmetric domains, such as the ones formed by the *trans* isomer of the azobenzene derivatives studied in this thesis. In its analysis, one considers that only a spatial variation in the azimuthal angle ϕ exists, and the rest of the parameters are assumed uniform. This is reasonable because θ is directly related to the local monolayer density, which we assume homogeneous in equilibrium configurations. Therefore, BAM textures can be represented by spatial distributions of the azimuthal angle ϕ (Figure 6).

The analysis of digitized images in 256 grey levels is performed with the public domain software ImageJ [5], and permits to study changes in the molecular orientation.

As mentioned in the previous section, due to the microscope inclination, BAM images appear distorted and have to be corrected. This is done using a glass stage micrometer of known dimensions and with graduated lines, which is recorded oriented according to the X and Y-axis to obtain a relation between µm and pixels in each axis. Knowing this relation, images are corrected scaling one of the axes with respect to the other.

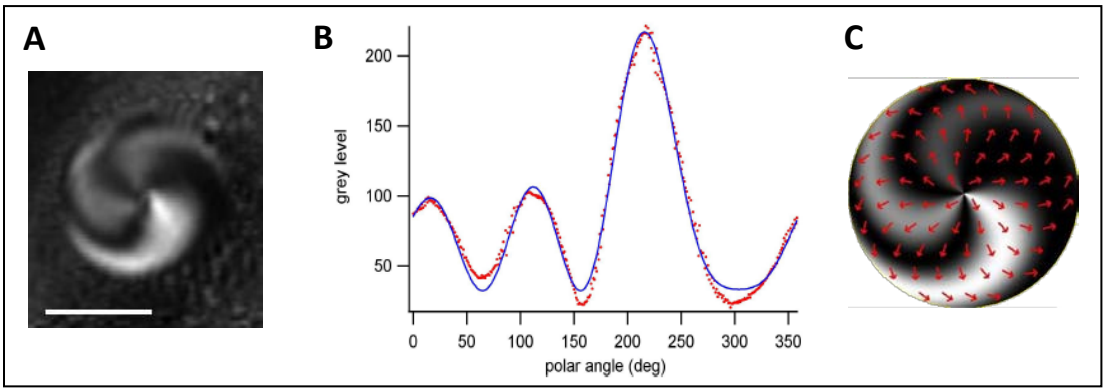

Figure 6. (A) BAM image of a circular splay domain of the *trans*-8Az5COOH amphiphile, surrounded by a *cis*-rich matrix. The line segment is 100 µm long. (B) Grey level as a function of the polar angle, ϕ, for the domain in (A). The solid line is a fit to the reflectivity data (see chapter 3). (C) Distribution of the azimuth field and its corresponding BAM texture that matches the experimental image in (A) [6].

SECTION 2.2

FLUORESCENCE MICROSCOPY

2.2.1 Principles of the Fluorescence Microscopy

Fluorescence microscopy has become an essential tool in different scientific disciplines such as biology, biomedical sciences, physics or material sciences, and it is used to introduce optical contrast between structures that appear homogeneous through traditional optical microscopy [7]. In general terms, a fluorescence microscope can be explained as an optical microscope that uses fluorescence to generate an image to study the properties of organic or inorganic fluorophores. The basic function of a fluorescence microscope is to irradiate the sample with light of a specific wavelength, which is absorbed by the fluorophores causing them to emit light of longer wavelengths. This weak emitted fluorescence has to be separate from the excitation light, and should be the only light reaching the detector so that the resulting fluorescence images have high contrast.

The fluorescence microscope used in this thesis is an epifluorescence microscope (commonly used in Langmuir monolayer visualisation [8-10]), where light of the excitation wavelength is focused on the sample through the objective lens, and the fluorescence emitted by the sample is directed to the detector by the same objective that is used for the excitation.

2.2.2 Components of an Epifluorescence microscope

Fluorescence microscopy requires intense, near-monochromatic, illumination. For this purpose, a high-energy short arc-discharge mercury lamp is the light source used in this system. In order to select the light of a specific wavelength, the multispectral light produced by the arc-discharge lamp is directed through a wavelength selective excitation filter, which blocks the unwanted wavelengths. The selected wavelengths reach a dichroic mirror, which is a specialised interference filter

that reflects shorter wavelength light and efficiently passes longer wavelength light. It is tilted at a 45° angle with respect to the incoming excitation beam, and reflects it at a 90° angle, pointing it directly to the sample through the microscope objective (which acts as a condenser). If the specimen fluoresces, the emission light gathered by the objective is able to cross through the dichromatic mirror because emitted light consists of longer wavelengths than the excitation light, and it is directed to an emission filter, which blocks the unwanted residual excitation wavelengths. After the latter selection process, the emitted fluorescence can reach the detector (Figure 2).

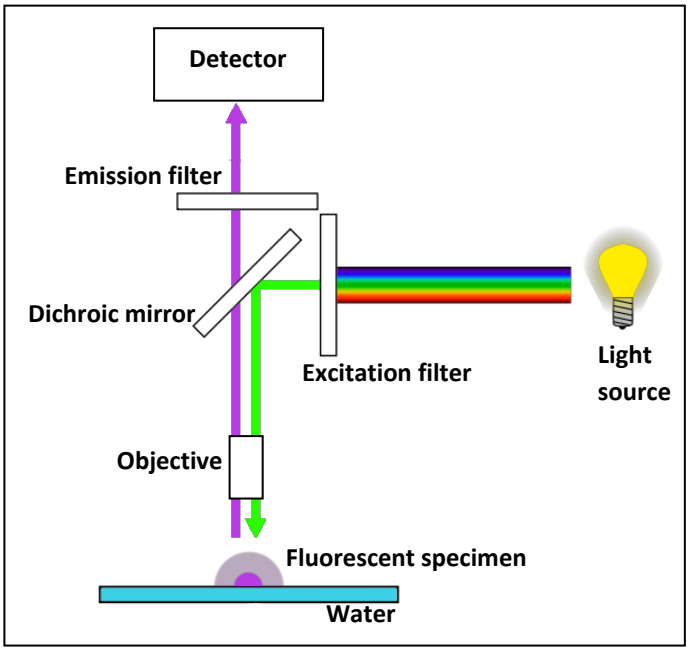

Figure 2. Schematics of an Epi-fluorescence microscope.

Factors that reduce the quality of fluorescence images and need to be taken into account are: not enough or too much concentration of fluorophore, low excitation intensity, arc lamp not well aligned, low-Numerical Aperture objective, bleaching and degradation of the fluorophore, background fluorescence, and low detector sensitivity [11].

SECTION 2.3

ATOMIC FORCE MICROSCOPY (AFM)

2.3.1 Principles of the Atomic Force Microscopy

Atomic force microscopy is a very high-resolution type of Scanning probe microscopy (SPM), with demonstrated resolution on the order of a fraction of a nanometre. SPM devices have the ability to sense the surface of a sample in a wide variety of ways (mechanically [12, 13], electrically [14, 15, 16], magnetically [17], etc.), offering the possibility to explore different kinds of surface properties, and making them useful in a wide variety of fields, going from materials science to physics and biology [18-21].

The AFM consists of a cantilever with a sharp tip (probe) that is used to scan the surface of the sample of study. During this process, the cantilever senses the interaction forces existing between the probe and the sample, that depending on the situation can be mechanical contact forces, van der Waals, electrostatic forces, etc., leading to a deflection of the cantilever. During this “contact” of the cantilever with the sample, the cantilever bends upwards while a certain force is applied to the sample. Typically, this deflection is measured using a laser spot reflected from the top surface of the cantilever into an array of photodiodes, and it is transformed into an electric signal, which is processed and delivered as topographic information of the sample point where the tip is placed. Since the system has the ability to scan the surface, a topographic image of all the scanned area is obtained. A simplified AFM schematic is depicted in Figure 1.

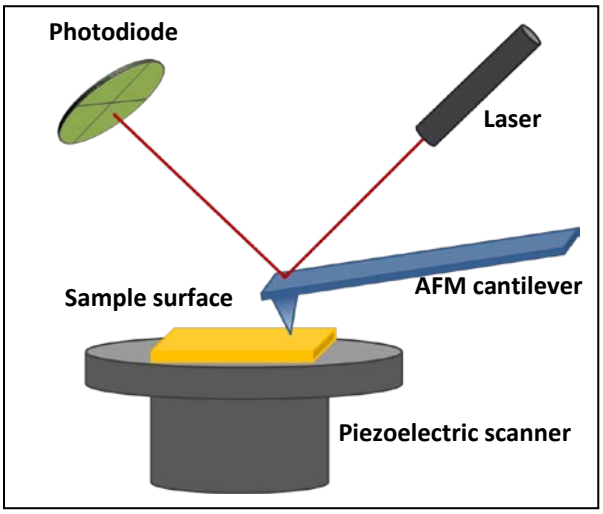

Figure 1. Schematics of an AFM. The sample is mounted on a piezo stage that allows movement on the X, Y and Z coordinates.

2.3.2 Components of an Atomic force microscope

The probe

An AFM probe consists of a micro-fabricated, extremely sharp tip on the free swinging end of a cantilever which is protruding from a holder plate, with a typical length of 50-200 µm. The tip apex, which is the part of the probe that contacts the sample, has an initial radius in the scale of nanometres (5-30 nm).

There are two basic cantilever shapes as shown in Figure 2, ones are fabricated with a triangular geometry, usually made of Si_3N_4 and with a wider back-plated zone, and others are fabricated with a rectangular geometry, usually made of SiO_2 .

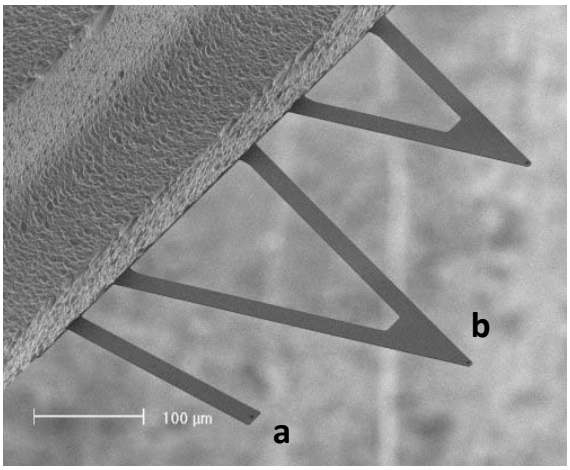

Figure 2. Si_3N_4 straight (a) and V-shape (b) cantilevers, mounted on the same chip [22].

Depending on the sample topography, there are limitations in achieving atomic resolution due to the physical probe not being ideally sharp. In order to perform accurate measurements in trenches for instance, it is necessary to use a high aspect ratio tip, that is, the ratio between the total tip length and its central width. When the tip is not sharp enough, the AFM images do not reflect the true sample topography, but rather represent the interaction of the probe with the sample surface (tip convolution phenomenon) (Figure 3). For standard measurements or flat surfaces, a low aspect ratio tip should be enough.

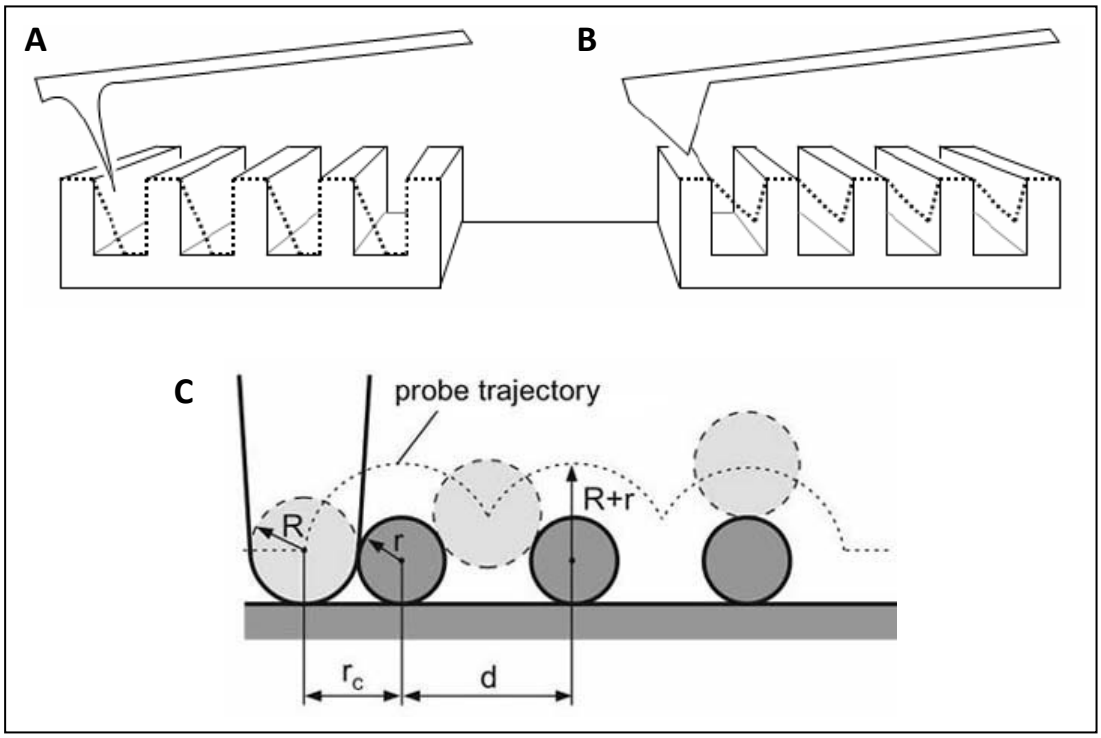

Figure 3. A) High-aspect ratio tip, suitable for imaging deep trenches. Notice that in this case, even though the trench depth is well measured by the tip, it does not track its real shape. B) Low-aspect ratio tip, which measures an incorrect depth and shape. The dotted lines in A) and B) represent the topographic image recorded by each tip. C) Tip convolution during the scanning of the sample surface with a thick tip. The scanned topographic profile differs much from the real surface geometry [23].

In order to calculate the force (F_v) needed to be exerted by the tip on the sample, the cantilever is considered as a spring. In this way, each cantilever has an elastic constant (k_v) which depends on the geometry and composition of the probe, and to which the force (F_v) is related through Hooke's law:

$$F_v = -k_v \cdot x \tag{5}$$

where *x* is the cantilever deflection (distance between the probe and the sample surface).

Detector

The most common method for cantilever deflection measurement is the beam deflection method, where a laser beam is used. First, the laser must be micro positioned to impact in the back-plated surface of the cantilever, and then on the photodetector, which usually consists of two closely spaced photodiodes whose output signal is collected by a differential amplifier. Then, when the tip scans the sample and deflects due to its topography, this movement is detected as a laser spot displacement by the photodetector. In this way, the mechanical movement of the cantilever is transformed into an electrical signal in the photodetector. If the photodiodes have two segments, they can transmit vertical information of the tip deflection, and if four segments are present, lateral deflection of the tip can also be sensed. The measured cantilever deflections are used to generate a map of the surface topography. After the detector receives the signal, it is sent to the feedback electronics, which maintain a constant deflection.

Piezoelectric scanners

AFM scanners are made from piezoelectric material, which expands and contracts proportionally to an applied voltage. The piezoelectric is responsible for the scanning movement in X-Y axes with nanometric resolution, as well as moving the sample in the Z axis as a response to the sample topography with extreme precision [24, 25]. Nevertheless, piezo scanners exhibit more sensitivity at the end than at the beginning of the scan, and this causes the forward and reverse scans to behave differently and display hysteresis between the two scan directions. There are different ways to correct this behaviour, although it can be considered negligible for small scanning areas. Usually, the piezo is set beyond the sample, so it is the sample that moves while the cantilever deflection remains stationary.

2.3.3 AFM operation modes

In the present section only the AFM topographic modes will be explained, since they are the ones used in this thesis. To understand them, it is useful to first analyze a Force vs. tip-surface distance curve (Figure 4) [26,27]. Basically, it consists on a vertical displacement of the cantilever towards the sample, and, what is first seen when the tip is far from the surface, is that no interaction between the cantilever and the sample exists (no cantilever deflection is detected, Figure 4a). As the tip approaches the surface, several interactions begin to build up between the tip and the surface, such as Van der Waals, electrostatic and capillarity forces. During this process, the cantilever bends suddenly and contacts the surface (jump-to-contact, Figure 4b). As the cantilever continues moving towards the surface, at very small tip-sample distances (a few angstroms), a strong repulsive force appears between the tip and the surface atoms, causing the cantilever to bend upwards, in what is considered the "real contact" (Figure 4c).

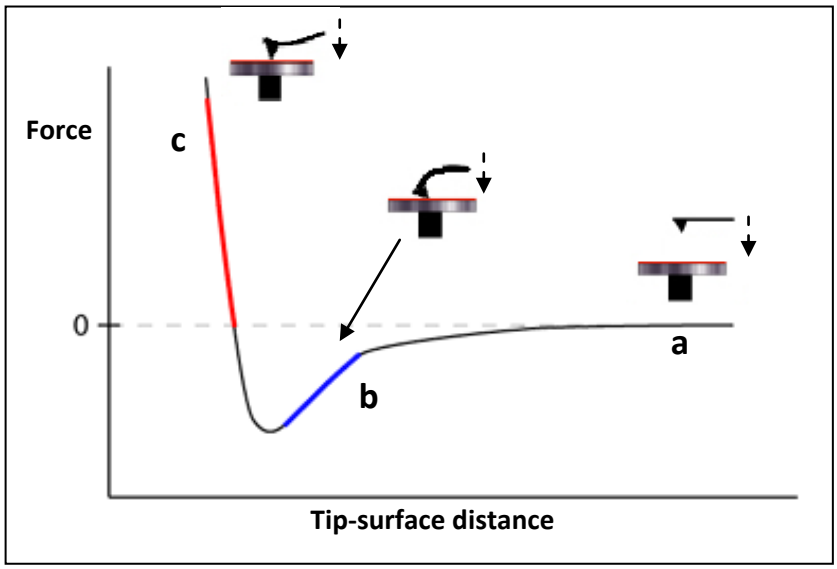

Figure 4. Typical force curve where the different contact regimes that the tip-sample undergo are represented. In (a), the tip is far from the surface and no interaction between both bodies is detected. As the tip approaches the surface, it bends downwards due to attractive forces (b). The blue line represents the attractive regime. When the tip becomes closer to the surface (c), it bends upwards due to the hard contact with the sample (a repulsive regime appears, represented by the red line).

Contact mode

In this mode, the tip and the sample are in real contact during the scanning of the surface, meaning that the cantilever is bent upwards up to a certain extent. During the acquisition of a topographic image, Δx and F_v are kept constant providing the best topographic resolution, but usually causing a physical modification of the sample surface that changes its topography and properties. As a consequence, this mode is adequate to scan hard materials such as metals, oxides, minerals, etc. It can be used with biological samples as long as F_v is carefully minimized.

Non-contact mode

In this mode the tip is oscillated at its own resonance frequency, and the amplitude of the oscillation is remained constant to maintain a constant distance from the surface. Although this mode is considered a non-contact mode, it has been demonstrated that the tip randomly jumps from non-contact to contact regimes [28]. Compared to contact mode, this mode has a poorer resolution due to the larger distance between the tip and the surface and that mechanical contact is minimal, but on the other hand artifacts are reduced as well as sample degradation. It is suitable for soft organic surfaces.

Tapping mode

It is similar to the non-contact mode, but the oscillation amplitude is set as ~ 50-60% of the "free" amplitude. In this way, resolution is higher than in non-contact mode and the sample damage is minimum. Frictional forces typical from the contact mode are eliminated by intermittently contacting the surface and oscillating with sufficient amplitude to prevent the tip from being trapped by adhesive meniscus forces from a water layer on the sample surface (all samples unless in a controlled UHV or environmental chamber have some liquid adsorbed on the surface). It is suitable for samples that are easily damaged or loosely held to a surface, such as biological samples. Tapping mode is the mode used in the topographic AFM image acquisition in

this thesis, working with an AFM commercial system combined with a custom-built polarizing reflection microscope mounted on the AFM header. The header originally contains two beam splitters and one of them has been replaced by a nonpolarising splitter, in order to allow the pass of linearly polarized light coming from the reflection optical microscope without perturbing it. In this way, combined optical and atomic force microscopy of samples with thin aggregates can be done, when the samples are deposited on engineered silicon substrates that reflect light with normal incidence without changing its state of polarization.

SECTION 2.4

REFERENCES

[1] S. Hénon, J. Meunier. *Review of Scientific Instruments*, **62**, 936 (1991).

[2] D. Hönig, D. Möbius. *The Journal of Physical Chemistry*, **95**, 4590-4592 (1991).

[3] J. Meunier. *Colloids and Surfaces A*, **171**, 33-40 (2000).

[4] A. Pulido-Companys, J. Ignés-Mullol. *Journal of Colloid and Interface Science*, **352** (2), 449-455 (2010).

[5] C. A. Schneider, W. S. Rasband, K. W. Eliceiri. *Nature methods*, **9** (7), 671-675 (2012). http://rsb.info.nih.gov/ij/

[6] J. Ignés-Mullol. BAM images generator: http://www.ub.edu/socsam/jordi/researchpage.html

[7] F. S. Wouters. *Contemporary Physics*, **47**, 239-255 (2006).

[8] A. K. Dutta, H. Lavoie, K. Ohta, C. Salesse. *Langmuir*, **13**, 801-807 (1997).

[9] Z. I. Lalchev, A. R. Mackie. *Colloids and Surfaces B*, **15**, 147-160 (1999).

[10] P. Viswanath, K. A. Suresh. *Physical Review E*, **67**, 061604 (2003).

[11] J. Lichtman, J. A. Conchello. *Nature Methods*, **2**, 910 (2005).

[12] W. Z. Rong, A. E. Pelling, A. Ryan, J. K. Gimezewski, S. K. Friedlander. *Nano Letters*, **4**, 2287-2292 (2004).

[13] S. Garcia-Manyes, G. Oncins, F. Sanz. *Biophysical Journal*, 236 A (2007).

[14] D. J. Wold, C. D. Frisbie. *Journal of the American Chemical Society*, **123**, 5549-5556 (2001).

[15] J. V. Macpherson, P. R. Unwin, A. C. Hillier, A. J. Bard. *Journal of the American Chemical Society*, **118**, 6445-6452 (1996).

[16] P. S. Dobson, J. M. R. Weaver, M. N. Holder, P. R. Unwin, J. V. Macpherson. *Analytical Chemistry*, **77**, 424-434 (2005).

[17] H. Cui, S. V. Kalinin, X. Yang, D. H. Lowndes. *Nano Letters*, **4**, 2157-2161 (2004).

[18] X. H. Li, G. N. Mu. *Applied Surface Science*, **252**, 1254-1265 (2005).

[19] C. Kleber, J. Weissenrieder, M. Schreiner, C. Leygraf. *Applied Surface Science*, **193**, 245-253 (2002).

[20] R. Stomp, *et al*. *Physical Review Letters*, **94**, (2005).

[21] H. T. A. Brenning, *et al*. *Nano Letters*, **6**, 937-941 (2006).

[22] http://www.nanotechweb.org

[23] www.ntmdt.com/spm-basics

[24] G. A. G. Cidade, G. Weissmuller, P. M. Bisch. *Review of Scientific Instruments*, **69**, 3593-3597 (1998).

[25] Q. X. Huang, *et al*. *Sensors and Actuators A-Physical*, **125**, 590-596 (2006).

[26] K. K. M. Sweers, M. L. Bennink, V. Subramaniam. *Journal of Physics: Condensed matter*, **24**, 243101 (2012).

[27] B. Cappella, G. Dietler. *Surface Science Reports*, **34**, (1999).

[28] R. Garcia, R. Perez. *Surface Science Reports*, **47**, 197-301 (2002).

CHAPTER 3

MONOLAYERS OF PHOTOSENSITIVE AZODERIVATIVES

SECTION 3.1

EXPERIMENTAL SYSTEM

3.1.1 Langmuir monolayers of azobenzene derivatives

In this chapter we study Langmuir monolayers of the following azobenzene amphiphiles: 4-octyl-4'-(5-carboxy-pentamethyleneoxy)azobenzene, 8Az5COOH in shorthand notation, and the chiral *(R/S)*-4-[4-[(4-(1-methylheptyloxyphenyl)azo] phenoxy]butanoic acid, or (*R/S*)-7'Az3 [1] (Figure 1A). The presence of the *azo* moiety (-N = N-) in the alkyl chain of these compounds allows a *cis-trans* isomerisation, which can be photo-induced (Figure 1B) [2]. When the compound is irradiated with UV light (λ = 365 nm) a *trans* to *cis* isomerisation takes place, whereas the *cis* to *trans* isomerisation occurs under exposure to visible light or by thermal isomerisation.

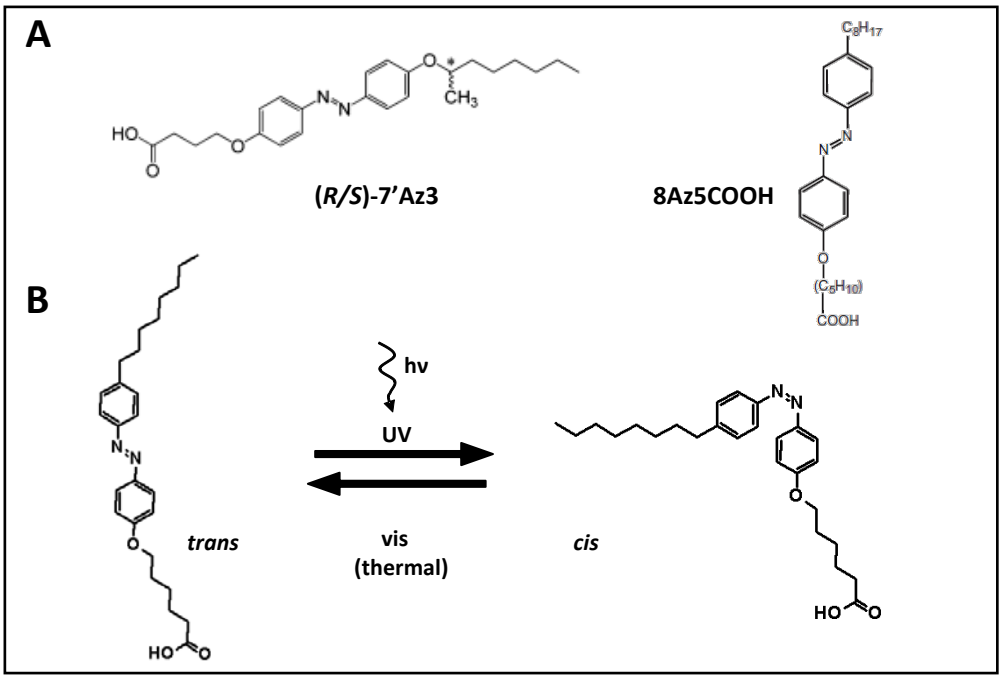

Figure 1. A) Chemical structure of (*R/S*)-7'Az3 and 8Az5COOH. B) Photoisomerisation between the *trans* and *cis* isomers

It is worth mentioning that both isomers have different dielectric properties, so a different amphiphilic behaviour. The bent configuration of the *cis* isomer confers a high dipolar moment to the molecule, whereas in the *trans* form molecules are stretched and have a negligible dipolar moment [3]. Consequently, both isomers organise differently at the air/water interface and form monolayers with different properties.

Cis-rich monolayers have not been studied in the present work since they are similar to the ones observed for the analogue compound 8Az3COOH [4], which present an expanded isotropic phase and do not show any phase transition. In order to obtain a *cis*-rich monolayer, the system has to be irradiated with UV light, or the spreading solution has to be exposed to UV light prior to the spreading step. As a result of the *cis* conversion the dipolar moment of the amphiphiles increases substantially, and so does their solubility in water.

The 8Az5COOH *trans* isomer, when confined in a two-dimensional environment, forms mesophases with long-range orientational order but positional disorder, just like its shorter homologue 8Az3COOH. If one compares this behaviour with the observed in lipid monolayers, a clear difference in the organisation of the mesogens is found. Lipid monolayers feature hexatic phases with long-range orientational order and short-range positional order. This different behaviour can be attributed to the ability of the *trans* molecules to self-aggregate. These aggregates result from a head-to-tail interaction (J-aggregates) or a face-to-face interaction (H-aggregates) (Figure 2) [5-9]. The presence and nature of these aggregates can be evidenced by means of UV/Vis absorption spectroscopy, giving a shift of the adsorption band to higher wavelengths with respect to the monomer adsorption band in the case of J-aggregation, and a shift to shorter wavelengths in the case of H-aggregation. In our system, the *trans* molecules associate keeping their molecular axis parallel to each other and perpendicular to the stacking direction, forming H-aggregates, even in the case of (*R/S*)-7'Az3 *trans* monolayers, where no mesophases are found.

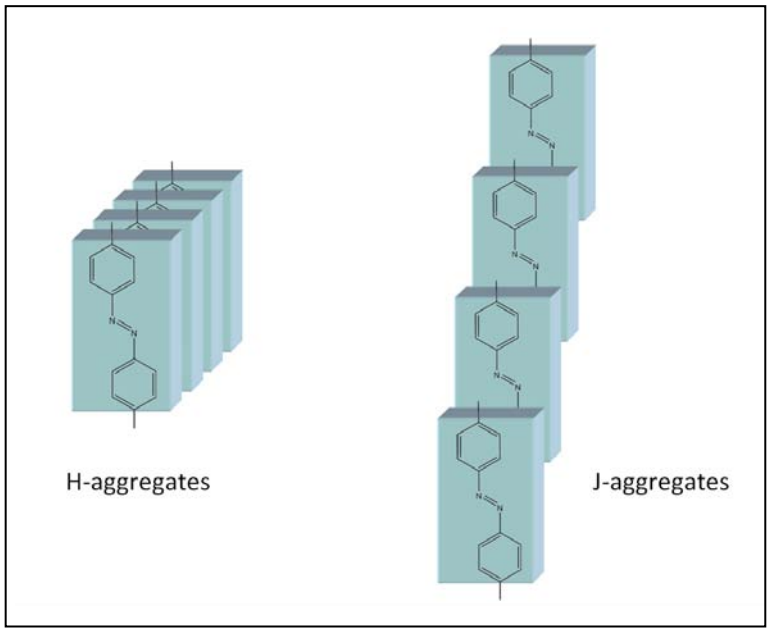

Figure 2. Schematic representation of the molecular organisation in H-aggregates (left) and J-aggregates (right).

When working with 8Az5COOH nearly pure *trans* monolayers or *cis-trans* monolayers, it is possible to obtain different morphologies and textures depending on the temperature and surface pressure conditions chosen, and they can be visualized by Brewster Angle Microscopy (BAM). By this technique, *trans* 8Az5COOH Langmuir monolayers show extended domains with smooth reflectivity gradients and high lability, at low surface pressures and large molecular areas (at around 35 $Å^2$ $molecule^{-1}$). At larger molecular areas, the monolayer presents coexistence between the gas phase and a mesophase, and when the molecular area is decreased, the gas phase disappears and the mesophase remains until a first-order phase transition is reached (*plateau*). After the phase transition, a more rigid mesophase with higher order is obtained [10], and further compression leads to the collapse of the monolayer.

In the case of (*R/S*)-7'Az3 *trans* monolayers, no mesophases are observed at optical length-scales and at any pressure until collapse takes place, when domains with multilayer thickness grow if compression is maintained. Such domains, reflect the quirality of the compound.

Temperature is a key parameter that needs to be carefully controlled due to its great effect in the morphology and fluidity of these monolayers. The higher the temperature is, the more labile is the mesophase.

If the 8Az5COOH azobenzene solution is exposed to room light, a mixture of the two isomers is obtained, reaching a photostationary composition. When this solution is spread at the air/water interface, the two isomers spontaneously phase separate due to its immiscibility and form circular *trans*-rich domains, surrounded by a *cis*-rich matrix. The same configuration is obtained when a *cis* monolayer is spread under room light conditions and photoisomerization to the *trans* form occurs. These circular domains formed, present different orientational configurations of the molecules, characterised by a constant polar tilt angle with respect to the monolayer normal [11], and a varying azimuth (distribution of the molecular orientation). Molecules organise around a defect (point singularity), which can be centred in the domain or located at the boundary, and the different textures observed depend on the control parameters of the monolayer, surface pressure and temperature, and the domain size [12]. At low temperatures (T = 15°C) the obtained configuration for small domains (< 100 μm) is type *bend*. In this configuration, the azimuthal field is organised around a central defect perpendicularly to the radial direction (Figure 4a, 4b). Bigger domains feature a *double-boojum* configuration, displaying two diametrically opposite defects on the boundary (Figure 4c). At higher temperatures (T≥ 25 °C), bigger domains are found, performing *bend*, *double-boojum* and *splay* configurations. In the latter, a *bend* type configuration is maintained in the vicinity of the core, but when approaching the domain boundary the molecular azimuths tend to the radial direction [13-15]. When the azimuths point inwards it is called a *splay-in* configuration, if they point outwards, it is a *splay-out* configuration (Figure 4d-4g) [8, 12]. When the temperature is increased up to 35 °C, *splay* and *double boojum* domains of variable size are obtained, but if the domain exceeds ~500 μm of diameter, the texture does not have any symmetry and it appears similar to the texture observed in pure *trans* monolayers.

The photostationary (*R/S*)-7'Az3 solution is probably presenting such a phase separation, but the arrangement of the two isomers is too similar to be detected by BAM (see section 3.3).

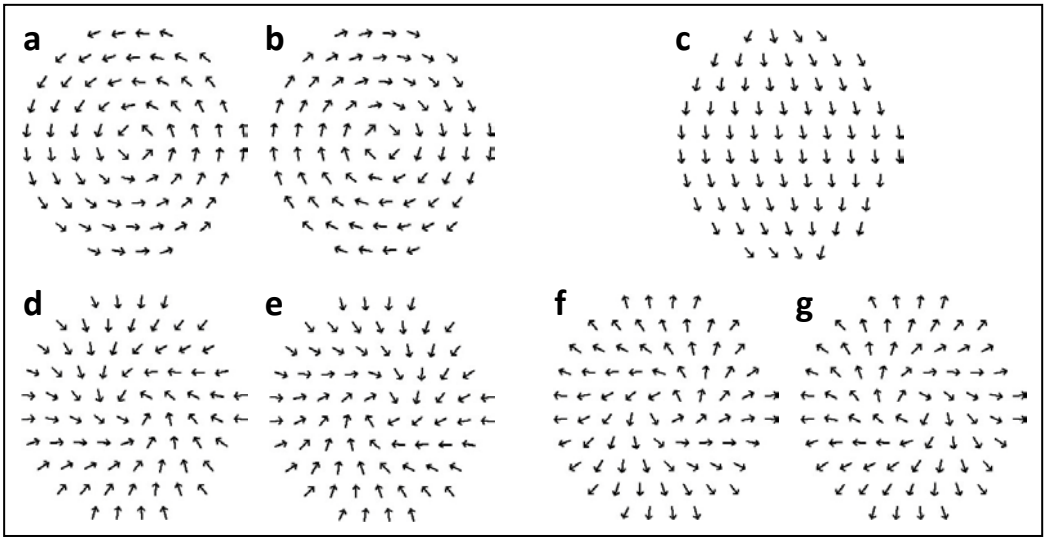

Figure 4. Schematic representation of the azimuthal field in type *bend* domains (a, b), counterclockwise texture (left), clockwise texture (right), *double-boojum* domains (c), and type *splay* domains (d-g), where the bend configuration is preserved in the core of the domain and evolves towards splay (inwards (d, counterclockwise) and (e, clockwise), and outwards (f, conterclockwise) and (g, clockwise).

3.1.2 Experimental protocols

3.1.2.1 Surface pressure-molecular area (π – A) isotherms of the *trans* isomer

Experimental setup

The experimental setup consists of a custom-made Teflon trough that contains the water subphase. The temperature in the subphase is regulated with a thermostatic aluminium block, which is attached to the trough, with a variation of 0.2K. The aluminium block contains a coil through which water coming from a thermostatic bath is circulated. A Teflon-encapsulated miniature bead thermistor is placed inside the subphase to monitor and control its temperature. The surface area can be adjusted by means of two spring-loaded, motorised Teflon or Delrin barriers, which provide a leak-free enclosure. The surface pressure is monitored using a filter paper Wilhelmy plate attached to an electrobalance (Riegler and Kirstein, GmbH) (Figure 5). Brewster angle microscopy is performed using a custom-built instrument, where the light from a 30-mW 650-nm diode laser (Monocrom, Spain) is spatially filtered and collimated to the desired beam size prior to being p-polarised by a prism and is directed towards the air-

water interface. A mirror placed perpendicularly to the water surface, and held on the same mechanical arm that the laser is, deflects the incident beam prior to reflection on the interface. The laser beam is directed towards the interface at an angle close to the Brewster angle (53.1°), and the reflected light passes through a second polarising prism prior to being focused on a CCD camera. The instrument is equipped with an XY translation stage that makes following a specific region possible.

The setup is seated on an optical table (ScienceDesk, Active Frame type, Thorlabs) to isolate vibrations from the surroundings, and is placed inside an enclosure to avoid air currents that would induce the drift of monolayers, and to enable working in the dark, since azobenzene derivatives are photosensitive. The system is computer-controlled with a National Instruments DAQ board and customised software signed with LabView.

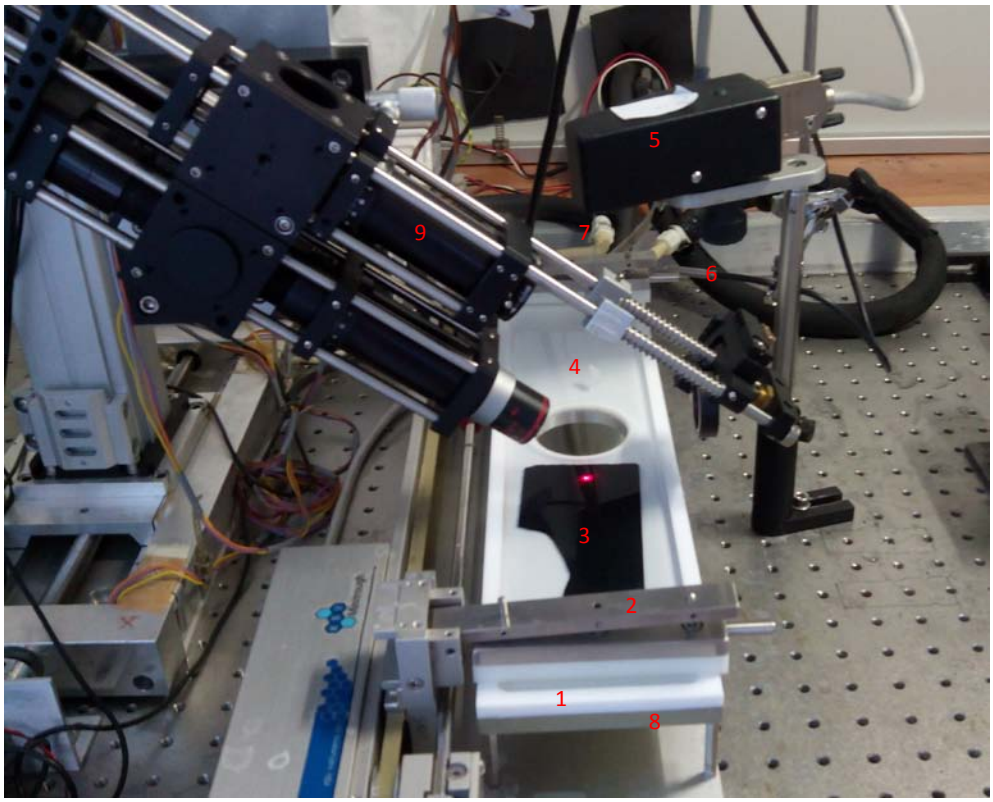

Figure 5. Picture of the experimental setup for the preparation of Langmuir monolayers, and for surface pressure-molecular area isotherms recording. (1) Teflon trough, (2) movable barriers, (3) dark glass to avoid laser beam reflection at the bottom of the trough, (4) filter paper Wilhelmy plate, (5) electrobalance, (6) thermistor, (7) tubes for water circulation inside the aluminium block, (8) thermostatic aluminium block, (9) BAM.

Materials

The amphiphilic compounds (*R/S*)-7'Az3 were custom synthesized by the *Grup de nous Materials Orgànics, IN2UB, Departament de Química Orgànica* [1], and 8Az5COOH was commercially obtained from Dojindo Labs. The subphase is ultrapure water (resistivity ~ 18.2 MΩ cm) from a Millipore MilliQ system. Spreading solutions are prepared using chloroform (Baker, p.a.) as solvent, and in the absence of light in order to ensure a nearly pure *trans* composition of the monolayer. Solutions are stored in the fridge and inside a dark box when not in use, in order to minimize the evaporation of chloroform. In addition, due to the high volatility of chloroform, it is convenient to seal the stopper of the solution flask with Teflon tape.

The glass material used to prepare the solutions is previously cleaned soaking it into hot chromic mixture, a saturated solution of potassium dichromate in sulphuric acid. Extreme caution has to be taken when handling the hot mixture, since it can cause serious burnt. The material is left in contact with the mixture until it reaches room temperature, and then it is rinsed with ultrapure water. After rinsing, the glass material is dried on a heater. The volumetric material needed to prepare the solutions is cleaned with cold chromic mixture during several hours, then rinsed with ultrapure water and dried with pure nitrogen.

Methods

When working with Langmuir monolayers, the cleanliness is a key step for the success of an experiment. It is very important to clean all the materials needed for the experiment before being in contact with the monolayer, and the cleaning process must be repeated every time a new compound is used.

The through and barriers are cleaned with an easily removable soap, such as a diluted solution in ultrapure water of concentrated Micro-90 soap (Sigma Aldrich). The water subphase has to be changed several times until its surface is clean when observed by BAM, sucking the water surface with a Pasteur pipet connected to a vacuum pump. This process is enough to clean the water surface between experiments when the same compound is used. If a new compound is to be used, the cleaning step

has to be repeated from the beginning with soap and pure water. The filter paper Wilhelmy plate has to be cut and rinsed with pure water every time a new compound is used.

Once the water subphase is clean and has reached the desired temperature, the balance is properly calibrated, and one can proceed to spread the monolayer on top of the water. Taking into account that working with the nearly pure *trans* isomer means working in the dark, all the process is carried out inside the dark enclosure with the doors closed, and in the presence of only a dim red light. The *trans* solution is stored inside a box to avoid the contact with ambient light and ensure the presence of a nearly 100% of *trans* molecules, and is spread on the interface by means of a clean Hamilton syringe, up to a pressure $\pi<0.5$ mN/m. After the deposition, a period of 10 minutes is left to allow chloroform evaporation, and compression isotherms are recorded. Barriers are compressed at a constant rate until the collapse of the monolayer, and BAM images are recorded for subsequent analysis. All the process is repeated for different temperatures ranging from 15 °C to 35 °C.

3.1.2.2 Monolayers of a *cis-trans* mixture

Experimental setup

Monolayer deposition on a quiescent subphase

The setup used for these experiments consists in the same experimental system described in the previous section, but in this case, as we are working with a mixture of both isomers, working in the dark is not required so the monolayer is exposed to room light.

Monolayer deposition under vortical flow

In order to study the effect of a vortical flow in the chirality of a 8Az5COOH monolayer, the following system has been used (Figure 6): a black Delrin (polyoxymethilene) circular trough (6 cm diameter, 1.7 cm depth), is embedded in a custom-made thermostatic Teflon cuvette. (The circular trough has two holes through which the water subphase in both cuvettes is connected. Both are placed on top of a

reversible magnetic stirrer (Agimatic-RevS, J.P. Selecta, Spain), with a range of stirring rates of 0 to 1600 rpm. A cylindrical Teflon-coated magnetic bar is placed at the centre of the Delrin cuvette, and is the responsible for the vortex flow created in the subphase. The temperature is monitored and controlled by means of a Teflon-encapsulated miniature bead thermistor. The whole system is seated on an anti-vibration table and placed inside a closed chamber, and is computer-controlled with customised software designed with LabView.

Materials

For experiments on a quiescent subphase, the studied solutions consist on pure 8Az5COOH, pure *R* or *S*-7'Az3, and 8Az5COOH doped with a 6% of *R* or *S*-7'Az3. The solvent is chloroform (Baker, p. a.). In order to obtain a *cis-trans* mixture, the monolayer has been spread using a room-light photostationary solution of either compound, or first a pure *trans* or *cis* monolayer has been spread, followed by UV light or ambient light irradiation respectively, to favour the appearance of the complementary isomer.

For experiments involving a vortical flow, solutions of pure 8Az5COOH and 8Az5COOH doped with a 6% of *R* or *S*-7'Az3 are used. In this case, all the experiments have been conducted starting from a nearly pure *cis* monolayer (irradiating the solution for 10 minutes with UV light), spreading the monolayer and letting the *trans* isomer domains grow.

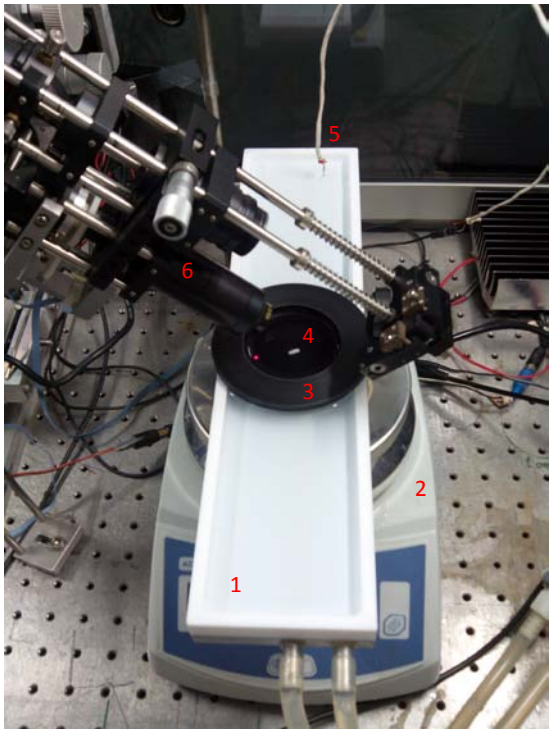

Figure 6. Picture of the experimental setup for the preparation of Langmuir monolayers under a vortical flow. (1) custom-made Teflon trough, (2) reversible magnetic stirrer, (3) black Delrin circular trough, (4) Teflon-coated magnetic bar, (5) thermistor, (6) BAM.

Methods

On what follows, different studies using the setups shown in Figures 5 and 6 are detailed. In order to characterise the domains found when the two isomers separate, monolayers of the *cis-trans* mixture of the pure 8Az5COOH and pure *R* or *S*-7'Az3 compounds are spread. In addition, 8Az5COOH monolayers have been doped with a 6% of the chiral compound (*R/S)*-7'Az3, in order to study its effect in the formation of *trans* domains during the phase segregation. Moreover, the effect of a vortical flow as a chiral force has been tested for pure 8Az5COOH and 8Az5COOH doped with a 6% of *R* or *S*-7'Az3 monolayers.

As previously mentioned, in this kind of experiments the cleanliness is an important factor. All the glass material that has to be in contact with the compounds should be cleaned with hot chromic mixture, the cuvettes and barriers are cleaned with soap and ultra-pure water, and both the Teflon-coated stirring bar and the Teflon-encapsulated thermistor are rinsed with chloroform. In all cases, monolayers are spread by means of a clean Hamilton syringe and temperature is strictly controlled.

Monolayer deposition on a quiescent subphase

When starting with a room-light photostationary solution, it is carefully deposited on top of the water surface, and after 20 minutes approximately (some time is needed for the domains to grow and coalesce in order to be big enough to be analysed), BAM images of isolated domains are recorded.

For experiments with pure *R* or *S*-7'Az3, another strategy to obtain a *cis-trans* monolayer has also been tried aiming to visualize the phase separation of both isomers. Starting from the *trans* pure solution (stored in the dark), the monolayer is spread and then irradiated with UV light (UV lamp, model VL-6, VilberLourmat with 365nm wavelength and 0.05 W cm^{-2} power density at 15 cm) to enhance the *trans* to *cis* conversion. By this method, the expansion of the monolayer due to the conversion from *trans* to *cis* isomer can be recorded by surface pressure measurements (see section 3.3).

When using a pure 8Az5COOH solution or a 8Az5COOH solution doped with a 6% of *R* or *S*-7'Az3, apart from spreading the photostationary solution to reach a mixed *cis-trans* monolayer, the following strategy is used in order to obtain a population of well-formed circular domains avoiding the formation of large masses of *trans* isomer. A pure *cis* solution obtained after 10 minutes of UV light irradiation is spread on top of the water, and the monolayer is left at ambient room light in order to let the *trans* domains grow slowly as the *cis* to *trans* conversion takes place. This process takes about 60-90 minutes to produce big enough domains to be analysed, then BAM images are recorded.

Monolayer deposition under vortical flow

On what follows, monolayers of pure 8Az5COOH and 8Az5COOH doped with a 6% of *R* or *S*-7'Az3 by weight have been used. In this case, solutions are irradiated with UV light for 10 minutes in order to obtain a nearly pure *cis* solution. Prior to monolayer spreading, a steady-state vortex flow is created in the subphase by means of a Reversible Magnetic Stirrer (J.P. Selecta, Spain) with a submerged cylindrical Teflon-coated magnetic bar (8 mm long, 3 mm diameter). Then, monolayers are prepared by carefully depositing one drop (2 µl) of the solution at the outer part of the vortex. The

subphase is stirred at a constant rate of Ω = 1000 rpm. When a monolayers is spread, it is always important to avoid letting the drop fall during the deposition since it could go to the subphase, and the final surface pressure wouldn't be the desired (in this experiments surface pressure is not monitored, but with a drop of 1mg/ml solution the pressure lays in the range 0-1 mN/m). The monolayer is stirred during 30 minutes after spreading, under room light, allowing spontaneous nucleation of *trans* domains. When stirring is stopped, BAM images are recorded during approximately 30 minutes to have enough recorded domains to determine the influence of the vortex flow on the handedness of the monolayer domains. The extent of chiral selection is quantified in terms of the enantiomorphic excess with respect to the amount of total clockwise domains, ee_{CW}, by applying equation (3.1). Values of ee_{CW} are calculated for each experiment, where different locations in the monolayer are taken into account, and it can be considered as an average value over the monolayer.

$$ee = \frac{2n_{CW} - n_T}{n_T} 100 \tag{3.1}$$

3.1.2.3 Transfer of the monolayer onto a solid substrate: Langmuir-Blodgett films

Monolayers of an amphiphilic compound are transferred onto a solid substrate by using the Langmuir-Blodgett method [16-18].

Experimental setup

The experimental setup used to prepare the Langmuir-Blodgett films (LB films) is shown in Figure 7. The barriers, thermistor, balance, microscope, etc. are the same described in section 3.1.2.1, except for the Langmuir trough (365 x 75 x 3.5 mm^3), which in this case has a central well 6.5 cm deep. The LB films are transferred to the substrate using a KSV-Nima Minitrough dipper.

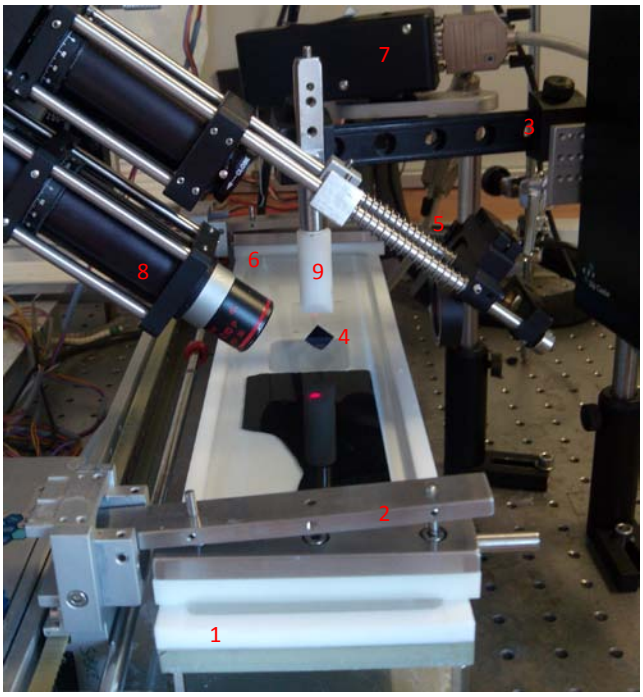

Figure 7. Experimental setup for the transfer of Langmuir monolayers onto a solid substrate by means of the Langmuir-Blodgett technique. (1) custom-made Teflon trough, (2) movable barriers, (3) KSV-Nima Minitrough dipper, (4) silicon substrate (SiO_2 SURF Standard, Nanolane) glued to a glass slice, (5) thermistor, (6) filter paper Wilhelmy plate, (7) electrobalance, (8) BAM, (9) dipper clip.

Materials

The spreading solution (1mg/ml) is prepared with chloroform (Baker, p.a.) as solvent. The subphase is ultrapure water supplied by a Millipore MilliQ system.

For the transfer of the monolayer from the water surface to a solid substrate, engineered silicon substrates (SiO_2 SURF Standard, Nanolane) are used. They are based on a silicon wafer substrate and engineered with a sequence of inorganic layers to tune their optical reflectivity so that light with normal incidence is reflected without changing its state of polarization. The top layer is composed of SiO_2, so the terminal groups are SiO_2/SiOH, and the rms roughness is less than 0.1. All this allows their characterisation by Optical Microscopy, as well as by Atomic Force Microscopy. The dimensions of the substrates are 10 x 10 mm^2, and 0.675 mm thick.

Methods

The substrates are activated with fresh piranha solution composed of 30% aqueous H_2O_2 and 70% concentrated H_2SO_4 (1:3, v/v). They are placed inside a staining jar, and covered with the solution for approximately 30 minutes. Piranha strongly reacts with organic matter so the solution can become extremely hot, thus it has to be handled with caution. Moreover, to avoid the possible accumulation of oxygen coming from the decomposition of the hydrogen peroxide, the solution cannot be stored in closed containers. Subsequently the substrates are rinsed with abundant ultrapure MilliQ water and, finally, dried with pure nitrogen and ready to be used.

To transfer a Langmuir monolayer onto a substrate, first the substrate has to be at least partially submerged into the aqueous subphase. For this purpose and due to the small size of the substrate used, it is glued with a double-sided adhesive tape stripe to a piece of microscope glass slide, which is held by the dipper clip. The dipper is placed in a way that the clean silicon plate is submerged into the water subphase contained in the central well of the Langmuir trough, until the water level is about to touch the adhesive tape. Contact between the tape holding the silicon substrate and the clean water subphase has to be avoided, in order to keep impurities from the tape glue away.

Once the silicon substrate is placed in a vertical position inside the subphase, and the water surface looks clean by BAM, one can proceed with the deposition of the Langmuir monolayer. Protocol explained in section 3.1.2.1 is followed to spread a monolayer, and to compress it to the desired state. Then, surface pressure is maintained constant and the substrate is withdrawn at a velocity of 8 mm min^{-1}. In this process, the monolayer is adsorbed on the silicon plate (Figure 8).

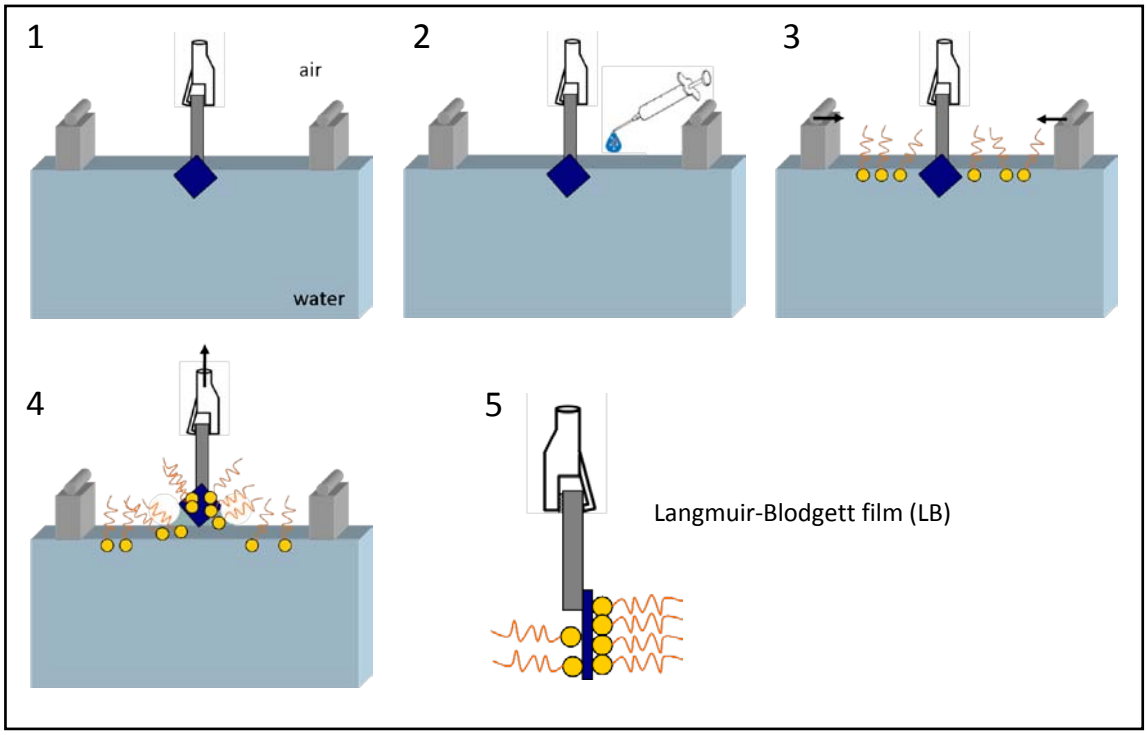

Figure 8. Schematic representation for the preparation of an LB film from a Langmuir monolayer. (1) A clean silicon substrate is held with the dipper clip and partially submerged in the water, (2) the *trans* solution is spread on the air/water interface and the monolayer is formed, (3) the monolayer is compressed until the desired pressure, (4) while the substrate is withdrawn, the monolayer is adsorbed onto it, (5) monolayer covering the silicon substrate

3.1.3 References

[1] A. Pulido-Companys, R. Albalat, J. Garcia-Amorós, D. Velasco, J. Ignés-Mullol. *Langmuir*, **29**, 9635-9642 (2013).

[2] H. Rau. *Photochemistry and Photophysics*. CRC Press, Boca Raton, Florida (1990), pp. 119-141.

[3] G. S. Hartley, R. J. W. Le Fèvre. *J. Chem. Soc*., 531-535 (1939).

[4] J. Crusats, R. Albalat, J. Claret, J. Ignés-Mullol, F. Sagués. *Langmuir*, **20**, 8668-8674 (2004).

[5] P. K. Behera, S. Mohapatra, S. Patel, B. K. Mishra. *Journal of Photochemistry and Photobiology A*, **169**, 253 (2005).

[6] S. Kirstein, S. Daehne. *International Journal of Photoenergy*, **1** (2006).

[7] J. M. Ribó, J. Crusats, J. A. Farrera, M. L. Valero. *Journal of the Chemical Society-Chemical Communications*, 681-682 (1994).

[8] J. Ignés-Mullol, J. Claret, R. Albalat, J. Crusats, R. Reigada, M. T. M. Romero, F. Sagués. *Langmuir*, **21**, 2948-2955 (2005).

[9] J. M. Pedrosa, M. T. M. Romero, L. Camacho, D. Möbius. *Journal of Physical Chemistry B*, **106**, 2583-2591 (2002).

[10] M. K. Durbin, A. Malik, A. G. Richter, C. J. Yu, R. Eisenhower, P. Dutta. *Langmuir*, **14**, 899-903 (1998).

[11] Y. Tabe, N. Shen, E. Mazur. *Physical Review Letters*, **82** (4), 759-762 (1999).

[12] R. Reigada, E. Abad, J. Crusats, J. Claret, J. Ignés.Mullol, F. Sagués. *Journal of Chemical Physics*, **121**, 9066-9076 (2004).

[13] T. M. Fischer, R. F. Bruinsma, C. M. Knobler. *Physical Review E*, **50**, 413-428 (1994).

[14] K. K. Loh, I. Kraus, R. B. Meyer. *Physical Review E*, **62**, 5115-5118 (2000).

[15] I. Kraus, R. B. Meyer. *Physical Review Letters*, **82**, 3815-3818 (1999).

[16] M. C. Petty. *Langmuir-Blodgett Films: An Introduction*. Cambridge University Press, United States (1996).

[17] A. Ulman. *An Introduction to Ultrathin Organic Films: From Langmuir-Blodgett to Self-Assembly*. Academic Press, San Diego (1991).

[18] D. K. Schwartz. *Surface Science Reports*, **27**, 241-334 (1997).

SECTION 3.2

THERMODYNAMICS AND MESOSCOPIC ORGANISATION IN LANGMUIR MONOLAYERS OF AN AZOBENZENE DERIVATIVE

3.2.1 Introduction

Langmuir monolayers of insoluble amphiphiles at the air-water interface are broadly studied systems, known since the beginning of the last century [1]. Due to their experimental simplicity and control possibilities [2], Langmuir monolayers offer a great potential for the study of the organisation of soft materials under non equilibrium conditions [3], and to understand the lateral packing of molecules based on their chemical structure, intermolecular interactions, and interactions with the supporting subphase [4]. Taking into account that any biological system is composed of soft (self-assembled) materials, Langmuir monolayers can be used as a model for such self-assembly, and present a wide range of biological applications as biomimetic systems [5] that can be related to biological membranes and the processes occurring within them, and may lead to the development of biosensors [6].

Among the different types of molecules that have been used to prepare Langmuir monolayers at the air-water interface, surfactants containing an azobenzene group are of special interest for their potential applications in photomechanical devices [7,8], optical switching, and image storing because of their high resolution and sensitivity [9,10]. These molecules are photosensitive and exposing them to UV light can induce the reversible transition from the *trans* to the *cis* isomer. In the same way, when the *cis* form is irradiated with visible light, or through thermal relaxation, the molecule isomerizes to the *trans* form (Figure 1). This photoisomerization gives rise to changes in properties such as the cross-sectional area of the molecule, molecular conformation, and dipole moment [11]. As a result, there will be a difference in the way the two isomers organise at the air/water interface. In previous studies working

with *trans* isomer monolayers of an azobenzene derivative, 8Az3COOH, a rich variety of morphologies was found, although a precise analysis of the thermodynamics of the phase change presented by such monolayers was not feasible [12]. On the other hand, it was found that monolayers prepared with a mixture of *trans* and *cis* isomers organise like a bidimensional emulsion. The structure of the disperse mesophase in such emulsions could be controlled by means of the thermodynamical variables or by light [13].

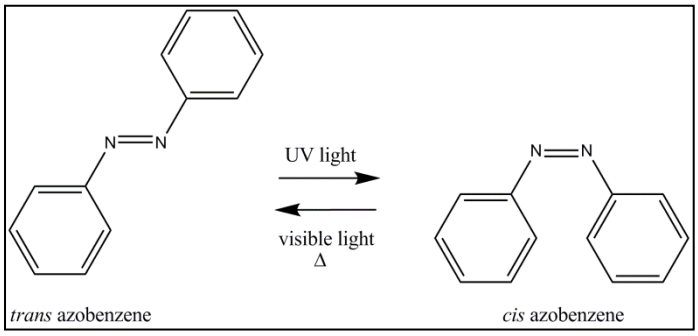

Figure 1. Illustration of the photoisomerisation of an azobenzene moiety (schematically drawn) [11].

In this work, we have studied the monolayer properties of an homologue compound, 4-octyl-4'-(5-carboxy-pentamethyleneoxy)azobenzene (8Az5COOH in our shorthand notation, see Figure 2) known to also form mesophases in the *trans* form [14–16]. Earlier studies with this compound have focused on the spectroscopic response of monolayers of the different homologues [14], the nature and extension of the supramolecular aggregates [15], and on the characterisation of stripped phases arising at high temperatures [16]. Although some compression isotherms have been reported, an accurate study of the thermodynamics of the observed first-order phase transition, and the temperature-dependent mesophase configuration for a wide temperature range are lacking in this system. This information may allow a better understanding of the role of the azobenzene group in the self-assembly of these monolayers, and could reveal new photosensitive structures with potential applications, both in pure monolayers or in mixtures of the two homologues.

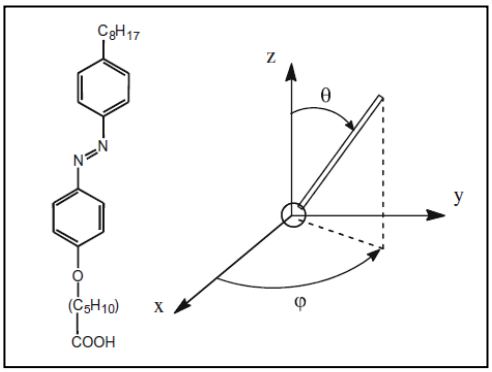

Figure 2. 4-Octyl-4'-(5-carboxy-pentamethyleneoxy)azobenzene, 8Az5COOH. Chemical structure: At the right, definition of the tilt (θ) and azimuth (φ) angles that configure the orientation of the molecules on the surface.

The first part of this work involves the study of monolayers of the pure *trans* isomer of 8Az5COOH, both by means of surface pressure-molecular area (π–*A*) isotherms and with simultaneous observation by Brewster angle microscopy (BAM). The latter is sensitive to the lateral order existing in the monolayer and offers a first description of the different phases, while the former can be used to characterise the thermodynamics of the first-order phase transition present in the system. The role of the azobenzene moiety in the self-assembly of these molecules is discussed by comparing the thermodynamic potentials in this system with those in monolayers of molecules with saturated aliphatic chains. The second part of this work focuses on the study of monolayers prepared with a photostationary mixture of the *trans* and *cis* isomers. We observe lateral phase separation between the two isomeric forms, our experiments suggesting that line tension between the two phases is significantly smaller for the homologue with the longer chain. Quantitative analysis of BAM images enables to characterised the molecular configuration inside circular isolated mesophase domains, whose morphology is less rich than the one reported for 8Az3COOH [17].

3.2.2 Experimental section

The compound 8Az5COOH was commercially obtained from Dojindo Labs (Japan) and was used as received. The subphase was ultrapure water from a Millipore

system. Spreading solutions (2 mM) were prepared using chlorofom (Baker, p.a.) as solvent.

Monolayers of 8Az5COOH were spread over the air-water interface contained in a custom-built Teflon trough (377x90x5mm^3), and compressed with a velocity of 11 mm/min following the protocol described in section 3.1.2.1. Brewster angle microscopy (BAM) was employed in order to get information on the supra-molecular organisation of 8Az5COOH in monolayers at different temperatures. The obtained images show a grey level distribution that can be correlated with the monolayer's local thickness and density. If the monolayer contains a mesophase, the grey scale distribution can be related to the local orientation of the molecules as well [18]. BAM images were recorded using a hard disk video recorder, and digital image analysis was performed with the software ImageJ [18]. The BAM analyser, which enables to resolve the azimuthal order in the monolayer, is set at 60° from the incidence plane, which spans North to South in the images. Geometrical distortion due to the oblique BAM observation is digitally corrected in all images reported here. Data analysis is performed with the software IgorPro (Wavemetrics, Inc.).

3.2.3 Results and discussion

Monolayers of trans-8Az5COOH. Compression isotherms and BAM imaging

In order to be able to consider the amount of *cis* isomer negligible in the spreading solutions, monolayers were prepared and stored in the dark. Moreover, the deposition on the air–water interface, as well as all manipulations, was performed inside the closed enclosure with the presence of only dim red light. Compression isotherms were recorded at temperatures ranging from 15 to 35 °C (Figure 3). The average of at least five realisations at each temperatura is reported, with a maximum dispersion in the area per molecule of 5%. In all cases, the surface pressure starts rising at an area per molecule between 35 and 40 Å^2 and gradually increases upon compression until a pressure (depending on the temperature) in which the monolayer starts undergoing a first-order phase transition signalled by a plateau region in the isotherm [1,19]. Compression past the transition eventually results in a cusp in the

isotherm, marking the collapse of the monolayer. This occurs at a surface pressure that decreases with temperature. This dependence, which is often described in the literature [20], indicates that the collapse process is kinetically and not thermodynamically controlled, as is the case in the first-order phase transition [21].

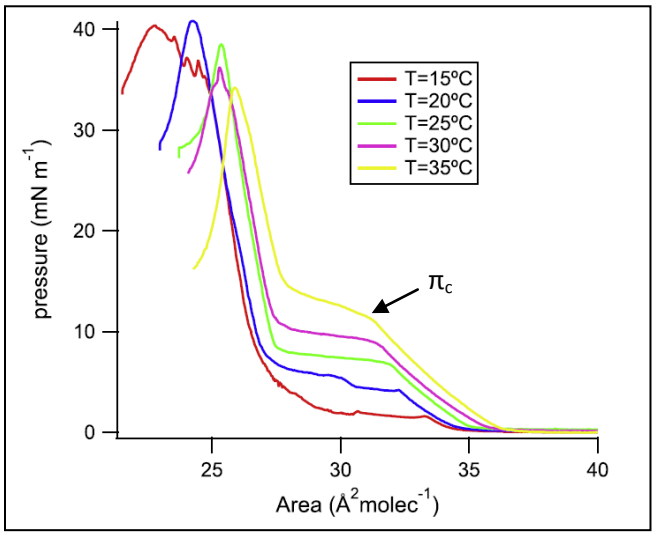

Figure 3. Compression isotherms of 8Az5COOH. The transition pressure π_c is marked in the isotherm performed at 35°C.

Isotherms recorded at the two lowest temperatures (T = 15 °C and T = 20 °C) reveal non-equilibrium features in the plateau (phase-coexistence region), in the form of noisy jumps in the lateral pressure. BAM images prove that this is the result of the mechanical response of the monolayer, which should be regarded as a complex two-dimensional material (see below). Upon further compression, the surface pressure rises until the collapse of the monolayer occurs.

At all temperatures and positive surface pressures BAM reveals monolayers with long-range orientational order. This is in contrast to monolayers of simple amphiphiles or phospholipids, where at low pressures isotropic liquid expanded phases are found, and only at high pressures the molecules arrange into an ordered (hexatic) phase [22].

The orientation of the molecules organised on the surface is defined by two angles: a tilt angle respect to the outward normal to the interface and an azimuth angle with a reference in-plane axis (see Figure 1). 8Az5COOH molecules in the

monolayer self-assemble forming domains with long range orientational order, large enough to be detected by BAM. The images that we obtained at low pressures reveal gradients in the monolayer reflectivity, which may be correlated with spatial changes in molecular orientation. In other words, the reflectivity (brightness) of the monolayer changes gradually as the orientation of the molecules changes, due to the optical anisotropy of the material. Monolayers spread at 15 °C organise forming a stripe texture with highly branched curved lines (Figure 4a). When the monolayer is spread at 20 °C or 25 °C the texture becomes more labyrinthine but formed by curved lines too (Figure 4c). At this range of temperatures reflectivity gradients decrease with increasing temperature, which means that the range of the orientational order in the monolayer increases. In addition, working at 20 °C and 25 °C, one can detect topological defects (structures where the symmetry typical of the ordered phase is locally broken. They arise spontaneously during the formation of such phase. Here, these defects are points where molecules presumably orient perpendicularly to the interface which determine the organisation of the mesogens with rotational symmetry surrounding a central point defect (Figure 4e). Configurations with this high symmetry are potentially very interesting for quantitative image analysis, from which important material parameters can be extracted [23,12,18]. A detailed analysis (not shown) has revealed that illumination inhomogeneities and monolayer deformations have distorted the orientational field, rendering these structures useless for a quantitative analysis. Below, we will present other configurations more amenable for this type of studies. From the BAM images one can see that the more the temperature is increased the more evident the stripe pattern is, the straighter and thin the lines become, and more fluid the mesophase is (Figure 4g and i). Reflectivity gradients increase when the temperature is increased past 25 °C, thus indicating the presence of a state of maximum orientational order at around 25 °C.

If the monolayer is further compressed there is a first-order (discontinuous) phase transition at a temperature dependent lateral pressure, π_c, and a totally new texture is achieved. BAM images obtained at high pressure show that the mesophase formed after this transition is composed of domains arranged as a mosaic (Figure 4b, d, f, h, and j). In such domains the reflectivity is constant, suggesting a parallel orientation of the molecules forming each domain, but different from the orientation of the

molecules in the neighbouring domains. Further studies have been done with the homologue compound, 8Az3COOH, which presents a very similar mesophase at high pressures. The mentioned studies consisting on Grazing X-ray diffraction analysis concluded that after the phase change an hexatic phase is obtained [24]. Similarities between BAM images of the two homologues in the low and high pressure phases [12,17] suggest that the behaviour of the surfactant reported in this work is the same, and that the high pressure phase features hexatic order. A more detailed study should involve the use of X-ray diffraction, which is beyond the scope of this work. At low temperatures the domains forming such mosaic are large (typical lateral size in excess of 100 μm) and well defined, whereas at higher temperatures the mosaic is formed by smaller domains (typical lateral size less than 50 μm) thus creating a fragmented texture. So in contrast with the results obtained at low pressures, in this case the orientational order decreases as the temperature increases. It is remarkable that the range of the orientational order above and below π_c is preserved if phase transition cycles are applied. For instance, the fragmented texture below π_c at 15 °C leads to the large domains in the mosaic texture upon compression above π_c (see Figure 4a and b), but the same fragmentation is regained if π is decreased below π_c again. This indicates that the range of the orientational order at a given π and T is inherent to the self-assembly of azobenzene molecules, and not a kinetic effect. What is more, it might be related to the formation of H-aggregates, previously reported by different groups [15,17], the formation of which would be a stable configuration for the *trans*-8Az5COOH molecules. In addition, at temperatures above room temperature, just before the phase transition, the stripe texture suffers a curious phenomena by which the stripes crease (see Figure 5). Again, this is not a kinetic effect; it is seen in all experiments above room temperature, and it is reversible: the original texture is regained when the pressure is decreased. Similar observations have been performed in 8Az3COOH monolayer [25], which suggests that this creasing may be the result of changes in the azobenzene-mediated self-assembly upon approaching the transition to the more ordered hexatic phase. These observations may hint towards a second-order transition. Such transitions represent a continuous change in the tilting of the molecules between two ordered phases and are difficult to detect by BAM imaging. In

order to assess whether there is evidence for a second-order phase transitions, we have calculated the isothermal compressibility modulus from the isotherms [19,1]. Nevertheless, we have been unable to detect any feature in the compressibility that might correlate with the changes observed in BAM images (Figure 5). Further studies will be required to find an explanation for the creasing of stripes.

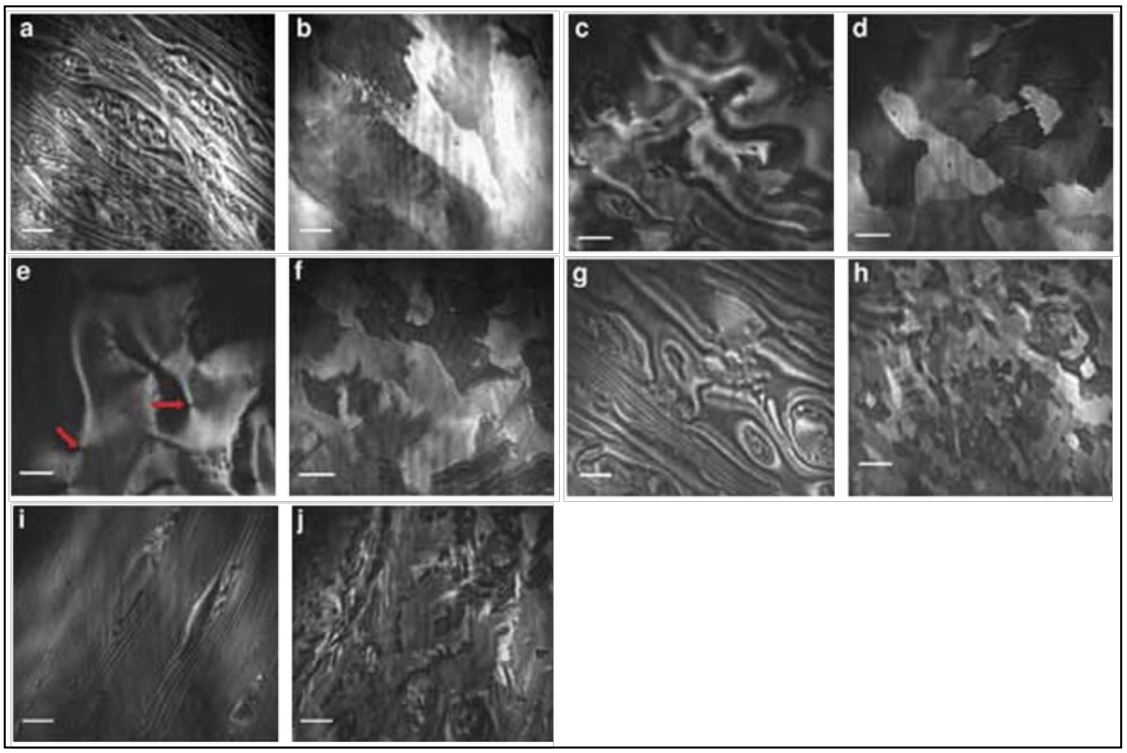

Figure 4. BAM images of *trans*-8Az5COOH monolayers at different temperatures. (a and b) Measured at 15 °C, (c and d) at 20 °C, (e and f) at 25 °C, (g and h) at 30 °C and (i and j) at 35 °C (each pair corresponding to the same experiment at different surface pressures). Images a, c, e, g and i correspond to low-pressure textures, and b, d, f, h and j correspond to high-pressure textures above π_c, after the phase change. Arrows on (e) mark point defects. The ruler is 100 μm long.

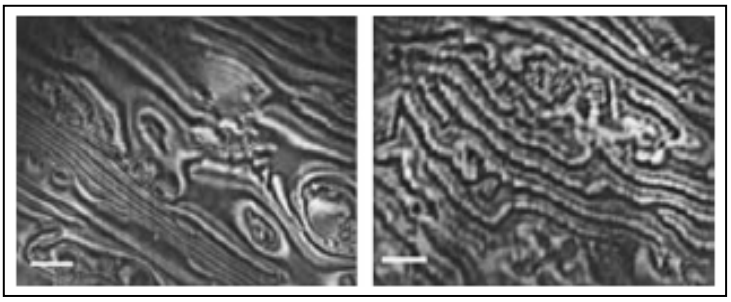

Figure 5. Creasing of the stripes prior to the phase transition. BAM images of the same region just before (left) and just after (right) the change. T = 30 °C. The ruler is 100 μm long.

On the other hand, BAM imaging provides useful information to interpret the noisy isotherms in the coexistence region at the two lowest temperatures (see above). Nucleation and growth of the high pressure phase proceeds through avalanches: sudden phase conversion occurs in finite, but macroscopic, regions in the monolayer. Such sudden changes in local density are detected by the pressure sensor, and result in jitter in the lateral pressure data within the plateau region (see Figure 3). To the best of our knowledge this is the first time such a dynamics is observed during phase transitions in monolayers, although complex viscoplastic behaviour has been reported during the collapse of monolayers [26,20].

Finally, compression past the collapse point results in the formation of multilayers that manifest as bright spots in the BAM images (BAM reflectivity increases with the square of the monolayer's thickness [18]). Applying compression cycles it was found that the collapse of the monolayer was sometimes reversible.

Monolayers of trans-8Az5COOH isomer: Thermodynamic study

The data just reported for 8Az5COOH can be analysed to characterise the thermodynamics of the first-order phase transition, which will provide information about molecular interactions within the monolayer. The heat and the entropy of the transition can be estimated applying the Clausius–Clapeyron equation,

$$\frac{d\pi_c}{dT} = \frac{\Delta S}{\Delta A} = \frac{\Delta H}{T\Delta A}, \tag{1}$$

where π_c is the value of the surface pressure during the phase change, ΔS, ΔH are the entropy and heat of transition, respectively, ΔA is the variation of the area per molecule during the phase change, and T is the temperature.

For each of the isotherms one can graphically obtain the value of the surface pressure when the phase change starts, at every temperature. Plotting the values of π_c vs. T the equilibrium coexistence curve is obtained, the slope of which is $\Delta S/\Delta A$. The variation of the area during the phase change (in the plateau region) is graphically

estimated from the isotherms by approximating a linear change in the lateral pressure in the hexatic phase, $\pi = f_T(A)$, and finding the area per molecule of this phase during phase transition by solving $f_T(A) = \pi_c(T)$. With this, the value for the transition entropy and enthalpy can be determined by simple calculations (Table 1).

***T* (°C)**	**π_c (mN/m)**	***ΔA* (Å2/molec)**	***ΔS* (J/mol)**	***ΔH* (kJ/mol)**
15	1.46	-5.79	-16.7	-4.82
20	4.19	-4.98	-14.4	-4.22
25	6.75	-4.11	-11.9	-3.54
30	8.83	-3.62	-10.5	-3.17
35	11.25	-3.16	-9.1	-2.81

Table 1. Thermodynamic phase transition data of *trans*-8Az5COOH.

Several studies determining the thermodynamic potentials of a monolayer undergoing a phase transition have been reported in the literature, but none using an azobenzene derivative. In the earlier work done in our group with 8Az3COOH, such analysis could not be performed because both the slope for π_c vs. *T* and *ΔA* could not be determined with enough precision due to the short or inapreciable plateau region present in the isotherms. The situation is different for 8Az5COOH, for which all the required parameters can be measured with confidence. In order to put the values for *ΔS* and *ΔH* obtained here in the proper context, we took the values reported by Albrecht et al. [27] as a reference. Their work was based on phospholipid monolayers, and they found for the heat of transition values around -15 kJ/mol for Dimyristoyl phosphatidic acid, and -25 kJ/mol for Dipalmitoyl lecithin (in a range of temperatures between 15 and 35 °C). Notice that these are double chain molecules, so one should consider half the reported values when comparing with a single chain molecule. Our values for 8Az5COOH are around -4 kJ/mol (in the same temperature range), which means that a lower amount of energy is required for the transition between the low and high pressure phases. A possible justification lies in the tendency of azobenzene chromophores to form H aggregates due to $\pi-\pi$ stacking, a phenomenon that has been widely studied [14,15,24,28]. The ability of this kind of molecules to self assemble

induces an orientational order in the expanded phase, which is a mesophase at unusually low surface densities, and this is the main difference with the totally disordered liquid expanded phase formed by phospholipids. The high-pressure phase in 8Az5COOH is, presumably, hexatic, just as liquid condensed phases in phospholipids, so a similar degree of order is expected. Therefore, ΔS should be smaller, in absolute value, for the azobenzene derivative as we do find indeed when comparing with the values reported by Albrecht et al. [27] for phospholipids, in the range -126 until -90 J/mol (temperature between 15 and 35 °C). With respect to the differences between the isotherms of 8Az3COOH and 8Az5COOH, the two extra carbon atoms that the latter compound has between the azobenzene moiety and the acidic terminal group should be responsible for the thermodynamic differences. The longer chain of 8Az5COOH provides the molecule with enhanced mobility and, as a consequence, the H-aggregate system that is the responsible of the formation of the mesophase might be more perturbed when compared to the one formed by 8Az3COOH. For this reason, we expect that the mesophase formed by 8Az3COOH should be more ordered, so there would be a smaller difference between its expanded and condensed phases, and the phase change should be even less energy demanding. In fact, we found that for 8Az3COOH the values for ΔA and $d\pi_c/dT$ are significantly smaller [12], and so would be expected to be the values for the thermodynamic potentials ΔS, ΔH, although they could not be determined with confidence.

Monolayers of a cis-trans mixture

Mesogens in the *trans* configuration can be forced into the *cis* form by exposure to UV light. Although we have not measured the isotherms of the pure *cis* monolayer for 8Az5COOH, they have been previously studied for the analogue compound, 8Az3COOH, showing a uniform isotropic phase, which does not undergo any phase transformation [12]. As mentioned above, spreading a roomlight photostationary mixture of the two isomeric forms of this compound resulted in a two-dimensional emulsion where *trans* rich circular domains featured axially symmetric inner textures that depended on domain size, temperature and lateral pressure [17].

We follow a similar procedure with 8Az5COOH, in order to test how the line tension between the two phases depends on chain length, and to explore the possible textures inside isolated domains in the homologue compound. Just after spreading the photostationary *cis*/*trans* mixture BAM images reveal a phase-separated monolayer, with small circular domains with an inner texture that cannot be resolved due to their small size (less than 10 μm in diameter). After about 20 min, coalescence and isomerisation into the *trans* form make these domains big enough to allow the study of their inner texture (diameter larger than 100 μm), displaying highly symmetric configurations similar to those of the shorter homologue. Although longer resting times may result in larger domains, the ripening process is much slower than in the case of 8Az3COOH, suggesting that line tension between the isotropic phase and the mesophase is much smaller in the longer homologue. Moreover, compression of the monolayer leads to a transition to the high pressure phase inside the domains, resulting in a mosaic texture analogous to the case of the pure *trans* monolayer. These indirect evidences suggest, consistently with what had been demonstrated for 8Az3COOH, that the circular mesophase domains are composed mostly of the *trans* isomer while the surrounding isotropic matrix is mostly *cis* isomer of 8Az5COOH.

Characterisation of the inner texture of the *trans*-rich domains is possible by fitting their BAM reflectivity to a suitable spatial distribution of the azimuth field, using an optical model that assumes that the monolayer behaves as a uniaxial birefringent optical medium [29]. This fit requires knowledge of the different instrumental parameters and of material parameters such as the polar tilt angle (usually assumed uniform across regions with small reflectivity gradients) and the two dielectric coefficients that characterise the interaction of light with this medium [23,18,30]. Finding these parameters is possible by analysing BAM images in a region with a very symmetric or known azimuth profile, provided images are free from optical artifacts. This is a critical step since, once these parameters are known with confidence, finding the azimuth distribution inside the isolated *trans*-rich domains can be done by trial and error, even with images of modest quality [17]. We proceed to determine these required material parameters by analysing a *trans*-rich domain at 35 °C featuring an axisymmetric spiral texture organised around a central point singularity (Figure 6A, 6B). We proceed by obtaining the gray level profile along a circumference of approximately

half the domain radius (actually, we average a circular corona 10 pixels thick in order to filter noise out). This profile is fitted to a reflectivity function (Figure 6C) by assuming an axisymmetric azimuth profile as described elsewhere [18]. The relevant material parameters are obtained from this fit, as summarised in Table 2.

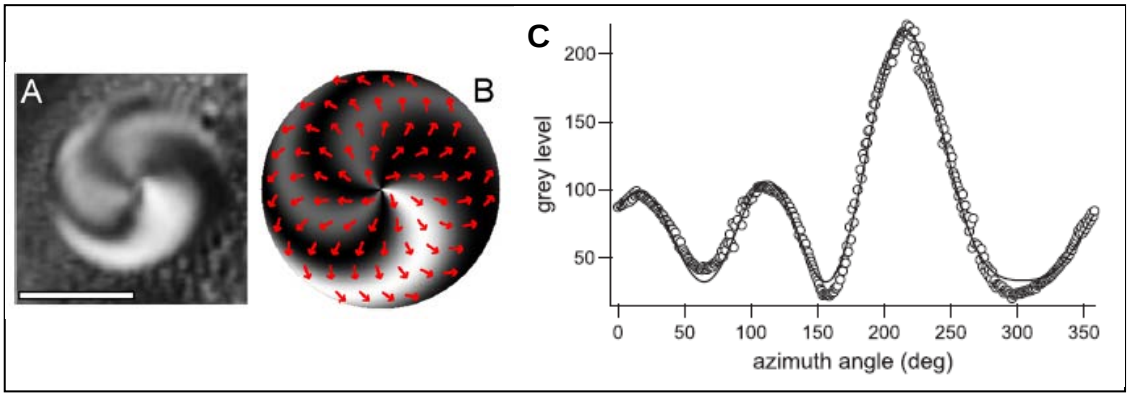

Figure 6. (A) Domain of *trans*-rich phase in a matrix of *cis*-rich phase for 8Az5COOH. T = 35 °C. The BAM analyser is set at 60°. The ruler is 100 µm. (B) Proposed azimuth field and corresponding BAM texture for the circular domain in (A), after finding all relevant material parameters. (C) Grey level as a function of the polar angle along a circumference of radius 52.5 µm, centred on the central point defect, for the droplet shown in (A). The solid line is a fit to the reflectivity data.

Parameter	Obtained value
$\varepsilon_{\perp}$ (fixed value)	2.2±0.1
ε_{II}	3.0±0.1
Polar tilt angle	55±3°
Analyser orientation (known value)	60°

Table 2. Material parameters extracted from the fit to the reflectivity data.

When compared to the material parameters obtained for 8Az3COOH [12], we observe that the dielectric coefficients for light polarised parallel (ε_{II}) and perpendicular ($\varepsilon_{\perp}$) to the alkane chains have identical values (within error), while the polar tilt angle is slightly larger for 8Az5COOH. Knowing these parameters we can propose an azimuth field that reproduces the observed BAM texture to a high degree of accuracy. We approximate this azimuth field with a fourth-order polynomial of the distance to the central defect, and the coefficients are selected to achieve an optimal match with the experimental BAM image. We conclude that for Figure 6 the azimuth

field is type bend (tangent to the circular boundary) near the central core and evolves towards a splay (radial) configuration near the boundary [17] (Figure 6B). At this point we are also able to analyse with confidence the inner texture of domains of 8Az5COOH under different experimental conditions. At 15 °C, mixed monolayers feature small circular domains (diameter <100 μm) with a bend type texture and bigger domains with a double boojum texture (two point singularities on the domain boundary [17]). As temperature increases, the size of the domains tends to increase as well, and at 25 °C we find bend domains that reach sizes of around 100 μm. At this temperature we find some splay domains and double boojums too. If the temperature is increased until 35 °C the monolayer presents splay and double boojum domains of variable sizes, but no bend domains are found.

To complete the comparison between photo-stationary monolayers of the two homologue compounds we check the photosensitive behaviour of 8Az5COOH monolayers. It is known that upon irradiation with polarised visible light of photo-stationary monolayers of 8Az3COOH, *trans* molecules forming splay domains tend to align with the polarisation of light. We irradiated 8Az5COOH monolayers with visible light of λ = 480 nm, and confirmed that splay domains do photo-align with the polarisation of light as well. On the other hand, bend and double boojum domains do not photo-align, similarly to what was observed with 8Az3COOH.

3.2.4 Conclusions

In the present work we have studied Langmuir monolayers of 8Az5COOH in comparison with a shorter homologue, 8Az3COOH, in order to demonstrate the influence of small structural changes in the capacity of amphiphilic molecules to self-assemble at the air/water interface. Yokoyama and co-workers had already reported dramatic dynamical changes following small variations in the molecular structure of monolayers of a series of homologues that included 8Az3COOH and 8Az5COOH [31], but an in-depth comparison of the equilibrium properties of the two systems was lacking. We have started with a thermodynamic analysis identifying the phases formed by *trans*-8Az5COOH at several temperatures, concluding that the surface pressure of

the phase change has an increased dependence on temperature. Such dependence has permitted the analysis of the phase transition, which was not possible with 8Az3COOH. By means of the two-dimensional Clausius–Clapeyron equation, we have determined variations in the thermodynamic potentials enthalpy and entropy upon phase change. Their magnitudes are significantly smaller than those obtained for monolayers formed by phospholipids of similar chain length [27]. To explain the decrease in those values we suggest that the ability of the azobenzene molecules to self-assemble by forming H-aggregates induces an orientational order in the more expanded phase that makes the transition to the more ordered phase less energy demanding than in the case of phospholipids. Simultaneously to the thermodynamic magnitudes, Brewster angle microscopy images have been obtained for the monolayers spread at different temperatures. Images feature textures whose local brightness can be related to molecular orientation. These observations indicate the presence of a state of maximum orientational order near 25 °C for the low pressure mesophase, and a steady decrease in the range of the order with temperature in the high pressure (presumably hexatic) phase [24]. We have also analysed monolayers formed by a mixture of *cis* and *trans* molecules. In such monolayer a segregation in *trans*-rich domains and a *cis*-rich region is observed, although the slow coarsening suggests that the two isomers have a much lower line tension than in the case of 8Az3COOH [17]. The quantitative analysis of the BAM images of an isolated domain has allowed the determination of some of the material parameters like the dielectric coefficients and the angles describing the orientational order, and has confirmed a molecular organisation with rotational symmetry. Finally, we have verified that *trans*-rich domains with the splay-out configuration photoalign when shined with linearly polarised light, in analogy to the behaviour of 8Az3COOH [13].

In summary, we have shown that in spite of the two homologues sharing rare features, such as the existence of a low density mesophase, the addition of two methylene groups in the alkane chain results in remarkably different thermodynamic behaviour and in a significant increase in the miscibility of the *cis* and *trans* isomers in monolayer form (a reduction in the line tension in the phase-separated monolayers). An interesting extension of this work could involve the exploration of mixed

monolayers of the two homologues, 8Az3COOH and 8Az5COOH, seeking for compositions where the richer morphological and dynamical features of 8Az3COOH can be extended to wider ranges of the thermodynamic control parameters.

3.2.5 References

[1] G.L. Gaines, *Insoluble Monolayers at Liquid–Gas Interfaces*. Interscience Publishers, (1966).

[2] P. Dynarowicz Latka, A. Dhanabalan, O. N. Oliveira, *Adv. Colloid Interface Sci.,* **91** (2), 221–293 (2001).

[3] A. Mikhailov, G. Ertl, *Science*, **272**, 1596–1597 (1996).

[4] V. M. Kaganer, H. Mohwald, P. Dutta, *Rev. Mod. Phys.,* **71** (3), 779–819 (1999).

[5] R. Maget-Dana, *Biochim. Biophys. Acta (BBA) – Biomembranes,* **1462** (1–2), 109–140 (1999).

[6] A. A. M. Santafe, L. J. Blum, C. A. Marquette, A. P. Girard-Egrot, *Langmuir,* **26** (3), 2160–2166 (2010).

[7] C.J. Barret, J. Mamiya, K. G. Yager, T. Ikeda, *Soft Matter,* **3,** 1249 (2007).

[8] Y. Yu, M. Nakano, T. Ikeda, *Nature*, **425**, 145 (2003).

[9] K. Ichimura, *Chem. Rev*., **100,** 1847–1873 (2000).

[10] T. Ikeda, O. Tsutsumi, *Science,* **268,** 1873 (1995).

[11] M. Matsumoto, S. Terrettaz, H. Tachibana, *Adv. Colloid Interface Sci.,* **87,** 147–164 (2000).

[12] J. Crusats, R. Albalat, J. Claret, J. Ignés-Mullol, F. Sagués, *Langmuir,* **20,** 8668–8674 (2004).

[13] J. Ignés-Mullol, J. Claret, R. Reigada, F. Sagués, *Phys. Rep. – Rev. Sect. Phys. Lett.,* **448** (5–6) , 163–179 (2007).

[14] T. Kawai, J. Umemura, T. Takenaka, *Langmuir,* **5,** 1378–1383 (1989).

[15] J. M. Pedrosa, M. T. Martín-Romero, L. Camacho, D. Mobius, *J. Phys. Chem. B,* **106** (10), 2583–2591 (2002).

[16] Y. Tabe, N. Shen, E. Mazur, H. Yokoyama, *Phys. Rev. Lett.,* **82** (4), 759–762 (1999).

[17] J. Ignés-Mullol, J. Claret, R. Albalat, J. Crusats, R. Reigada, M. T. Martin-Romero, F. Sagués, *Langmuir,* **21,** 2948–2955 (2005).

[18] J. Ignés-Mullol, J. Claret, F. Sagués*, J. Phys. Chem. B,* **108** (2), 612–619 (2004).

[19] A. Ullman, *Introduction to Ultrathin Organic Films*, Academic Press, San Diego (1991).

[20] P. Burriel, J. Claret, J. Ignés-Mullol, F. Sagués, *Eur. Phys. J.,* **143,** (2007).

[21] J. Adams, A. Buske, R. S. Duran*, Macromolecules,* **26** (11), 2871–2877 (1993).

[22] H. Mohwald, *Handbook of Biological Physics*, vol. 1, Elsevier Science B.V. (1995) (Chapter 4).

[23] M. N. G. De Mul, J. A. J. Mann, *Langmuir,* **10,** 2311–2316 (1994).

[24] M. K. Durbin, A. Malik, A. G. Richter, C. J. Yu, R. Eisenhower, P. Dutta, *Langmuir,* **14** (4), 899–903 (1998).

[25] J. Ignés-Mullol, private communication.

[26] J. P. Kampf, C. W. Frank, E. E. Malmstrom, C. J. Hawker, *Science,* **283** (5408), 1730–1733 (1999).

[27] O. Albrecht, H. Gruler, E. Sackmann, *J. Phys*. (Paris), **39,** 301 (1978).

[28] F. Xu, H. S. Kitzerow, P. P. Crooker*, Phys. Rev. A,* **46** (10), 6535–6540 (1992).

[29] G. A. Overbeck, D. Honig, D. Mobius, *Thin Solid Films,* **242,** 213–219 (1994).

[30] J. Wang, L. Zou, A. Jakli, W. Weissflog, E.K. Mann, *Langmuir,* **22** (7), 3198–3206 (2006).

[31] Y. Tabe, T. Yamamoto, H. Yokoyama, *New J. Phys.,* **5** (1), 65 (2003).

SECTION 3.3

SUPRAMOLECULAR ORGANIZATION AND HETEROCHIRAL RECOGNITION IN LANGMUIR MONOLAYERS OF CHIRAL AZOBENZENE SURFACTANTS

3.3.1 Introduction

The study of chiral interfaces, in particular in the context of molecular recognition, is of significant interest in material science, for instance in the development of sensors, optical filters, or catalytic surfaces [1]. Particular attention is deserved to insoluble surfactant monolayers self-assembled at the air-water interface that may be transferred onto solid support by means of the Langmuir-Blodgett (LB) technique [2]. Chiral recognition in these systems, both due to interaction within monolayer components or between monolayers and aqueous guests, has been extensively studied [3]. The high specificity of the lateral interactions in such low-dimensional systems can lead to significant differences in the thermodynamics of the racemic mixture when compared to the pure enantiomers [4], or may result in the spontaneous segregation of racemic mixtures into two-dimensional enantiomorphic crystals [5-7]. The presence of chiral surfactants often results in the formation of submillimeter domains with chiral shape [8] or molecular organization [9, 10], either during the isothermal condensation of ordered monolayer phases or during the collapse into stacked multi-layers. Monolayers of racemates may result in the chiral symmetry breaking of the self-assembled structures. The resulting racemic domains either feature segregated regions expressing one chirality or hinder the expression of molecular chirality altogether [11]. Heterochiral molecular recognition evidenced in changes in the phase behavior of racemic mixtures compared to pure enantiomers has been reported both for low molar mass and for polymeric liquid crystals [12, 13]. It has also been demonstrated that specific lattice-controlled interactions within aggregates

in Langmuir monolayers of racemic aminoacid mixtures can lead to the enhanced generation of homochiral ologipeptides [14]. Recently, experiments with racemic mixtures of aminoacid derivatives revealed new modes of self-assembly into nanostructures previously unobserved in the pure enantiomers [15, 16].

Among non-biomimetic films, monolayers of surfactant molecules featuring an azobenzene moiety have been the object of significant research interest both for the possibility to build photosensitive films [17] and for the enhanced ability of *trans* azobenzene molecules to statically and dynamically self-assemble at the air-water interface [18]. Although azobenzene-based compounds, both surfactants and non-surfactants, have been reported to form stable monolayers at the air/water interface, the self-assembly of ordered mesophases is restricted to very specific molecular structures [19]. A paradigmatic example is provided by the surfactant 8Az3COOH presented in the previous section [20], which features a rich polymorphism including labile photosensitive phases [18] and structures with orientational chirality that can be selected either by means of a chemical dopant or by the application of vortical stirring [21]. Recently, Haro et al., have reported experiments aimed at characterizing the supramolecular architechture of Langmuir monolayers and LB films of a chiral azobenzene surfactant, which we will denote (S)-3'Az7 [22]. Although this compound forms stable monolayers that enable the transfer of multilayer LB films, the authors do not observe the emergence of lateral order in this system.

In this section we report the self-assembly behavior of the two enantiomers (R/S) of the chiral azobenzene fatty acid 7'Az3 (see Section 3.1). In a recent publication, it was shown that these amphiphilic molecules could be employed as chiral dopants to select the otherwise random chirality of self-assembled domains of the surfactant 8Az3. In the current work, we wanted to explore the ability of the pure chiral analogues to self-assemble into ordered chiral structures. We find that, in contrast to the behavior of 8Az3, the ability of the pure enantiomers to form mesophases is hindered, presumably by the presence of the chiral center. Remarkably, a racemic mixture of the R/S enantiomers of 7'Az3 does self-assemble into an ordered mesophase at low lateral pressures. Brewster angle microscopy observations reveal the presence of pinwheel defect configurations, which is an unambiguous evidence of the existence of hexatic order at the nanoscale [23]. This is a striking example of

heterochiral recognition in monolayers in which a high degree of ordering is obtained through the interaction of two complementary chiral species that independently fail to organize as a mesophase. At all compositions, the chiral surfactants organize into ordered multilayers above the monolayer collapse pressure. The resulting submillimeter domains have been transferred onto engineered silica surfaces in order to analyze their configuration at the nanoscale by means of Atomic Force Microscopy, revealing a well-defined microstructure that depends on the monolayer composition.

3.3.2 Experimental section

Spreading solutions were prepared by dissolving the surfactants in chloroform (Baker, p.a.), to get a concentration of 1 mg cm^{-3}. Langmuir monolayers were spread on a thermostatic KSV-Nima Minitrough Teflon trough (365 x 75 x 5 mm^3), and compressed at 6 mm min^{-1} (compression rate of order 10^{-2} $nm^2molec^{-1}min^{-1}$) following the protocol described in section 3.1.2.1. The subphase temperature was kept at 25°C ± 0.2°C in the experiments reported herein. The system was computer-controlled by means of the provided KSV software. Real time BAM images were captured by means of a Sony XC-77CE CCD camera and stored in digital format for further processing with the public domain software ImageJ.

LB films were subsequently characterized by optical microscopy using a custom-built polarizing reflection microscope, and Atomic Force Microscopy (Nanotec Electrónica SL, Cervantes AFM system), using arrow-NCR-20 cantilevers in non-contact mode, with a thickness of 4.6 µm, a length of 160 µm, and a width of 45 µm. Their resonance frequency is 285 kHz approximately, and their force constant is 42 Nm^{-1}. AFM image acquisition and image processing has been performed with the aid of the software WSxM [24]. In the reported images, filters *plane*, *flatten*, and *equalize* have been applied on the raw data.

The original design of the AFM header (see Figure 1) provides a clear view access, through beam-splitter BS2, to the cantilever on top of the sample under investigation. As is typical in this type of instruments, the original design included a polarizing beam splitter that maximizes the reflection of the polarized laser used to

probe the tip deflection (red beam) but modifies the state of polarization of the light beam from the polarizing optical microscope (green beam). The ability to visualize thin aggregates on the SURF substrate relies on the use of polarized light and the observation of its reflection through a crossed analyzer. Reflection from the bare substrate is minimized this way so observed textures come from the presence of laterally organized thin films that modify the state of light polarization. The original polarizing beam splitter BS2 was replaced by a non-polarizing one to enhance the signal to noise ratio. With this modification we were able to obtain an accurate registry between optical observation of aggregates and the corresponding AFM scans.

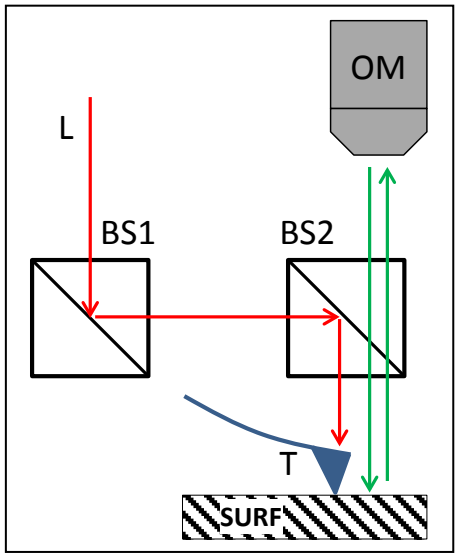

Figure 1. Diagram illustrating the setup that enables combined optical and atomic force microscopy of samples deposited on engineered substrates (SURF). The AFM probe laser (L) impinges on the cantilever tip (T) after deflection from two beamsplitters (BS1, BS2). Beamsplitter BS2 is non-polarizing, so it offers an unperturbed optical path for the linearly polarized light from the reflection optical microscope (OM).

3.3.3 Results and discussion

Langmuir films

We have measured surface pressure/molecular area isotherms for monolayers with the pure enantiomers and for a racemic mixture of the two chiral surfactants (Figure 2). We have taken great care to ensure that the azobenzene derivatives are in the thermodynamically stable *trans* form by preparing the spreading solutions under

dim red light and by performing the experiments in the dark or under dim red light. We report data for a temperature T= 25 °C, although no additional features have been observed for temperatures between 15 °C and 35 °C. The isotherms of both enantiomers have an observable but small shift in their relative area per molecule values that we attribute to experimental uncertainties. In other words, our observations are compatible with both enantiomers featuring identical thermodynamic behaviour, as one would expect in the absence of any external chiral influence [8]. Pressure lift-off takes place at around 35 $Å^2 molec^{-1}$, comparable to the value obtained for the achiral analogue 8Az3 [20], and slightly below the value reported by Haro et al. [22] for a compound of similar chain length but more distal position of the azobenzene moiety. A compression/expansion cycle shows little hysteresis provided the surface pressure is kept below monolayer collapse, whose signature is the appearance of a local maximum in the monolayer (Figure 2).

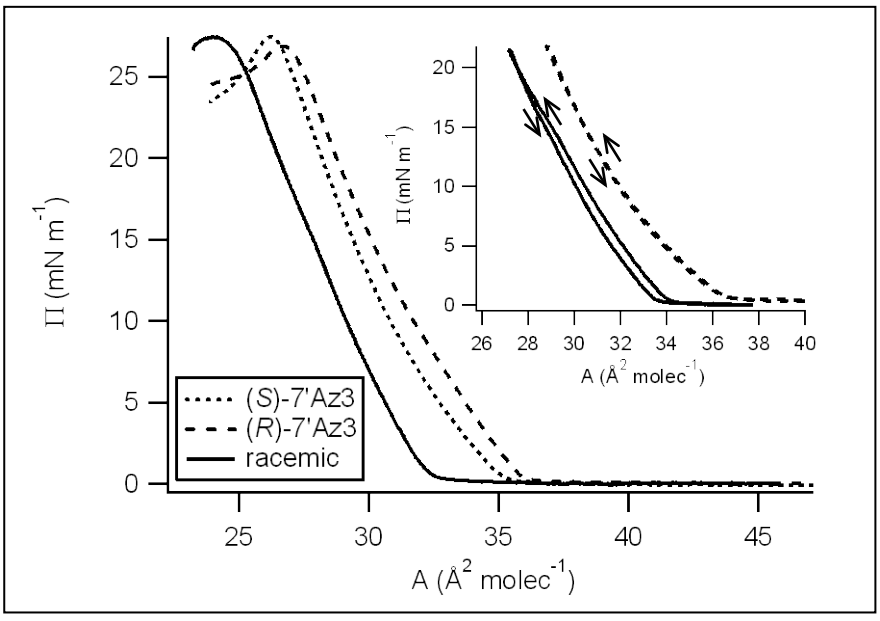

Figure 2.Surface pressure/molecular area isotherms at T = 25°C for monolayers of pure (*S*)-7'Az3,(*R*)-7'Az3, and for a racemic mixture. All isotherms are the average of five experimental realizations. In the inset, one of the isotherms for the R enantiomer and one for the racemic mixture are displayed as a compression-expansion cycle.

Real time Brewster angle microscopy reveals that the monolayers are isotropic at optical length-scales until collapse takes place below an area per molecule of 27 $Å^2$ $molec^{-1}$, approximately. This is consistent with the experiments by Haro et al. where

the authors report a featureless monolayer under BAM observations, and is in contrast to the behaviour or 8Az3, which features an ordered expanded phase that was attributed to the tendency of the *trans* azobenzene hydrophobic tails to form face-to-face H-aggregates on the air/water interface [26]. Nevertheless, we have found no measurable difference in the UV-vis spectrum of enantiomeric and racemic 7'Az3 monolayers after LB transfer (Figure 3), observing the signature of H-aggregation (hypsochromic shift in the UV-vis reflection spectrum) in both cases. A similar observation has been reported by Haro et al. for monolayers of (S)-3'Az7 [22], both in-situ and after LB transfer.

In previous experiments with the achiral analogue 8Az3, monolayers of a photostationary mixture of the *cis* and the *trans* isomers phase separate at the air/water interface, resulting in the coexistence of optically birefringent sub-millimetre regions rich in the *trans* isomer surrounded by optically isotropic regions rich in the *cis* isomer [20]. We have attempted to observe similar phase segregation with (R/S)-7'Az3, both by spreading a room light photostationary *cis*-*trans* mixture of either chiral enantiomer or by first spreading a pure *trans* monolayer followed by irradiation with UV light (see Figure 4). Although an expansion following *trans* to *cis* isomerization is detected by surface pressure measurements, BAM images reveal a homogeneous monolayer at all times. This might suggest either that *cis*-*trans* segregation does not occur for these compounds or that segregation does occur but the arrangement of the two isomers (lateral order and packing density) is too similar to be detected by our imaging equipment. Experimental evidence below with monolayers of a racemic mixture suggests that the latter hypothesis is most likely.

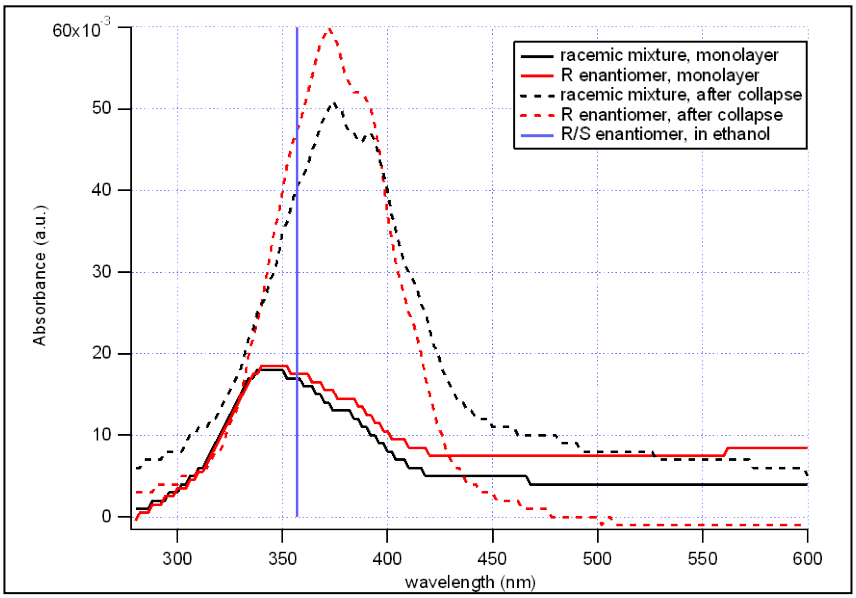

Figure 3. UV-vis absorption spectra of Langmuir-Blodgett films for the pure R enantiomer and for the racemic mixture (*trans* isomeric form), obtained with a single upstroke before and after monolayer collapse. The films were transferred onto a quartz substrate and analyzed in a Shimadzu 1601 uv-vis spectrophotometer using a custom-made accessory. The maximum in the absorbance of the pure enantiomers in ethanol is indicated with the blue vertical line.

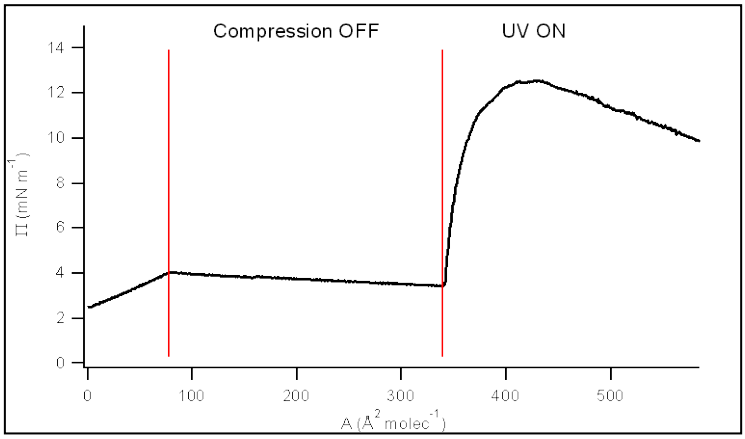

Figure 4. A pure *trans* monolayer of (*S*)-3'Az7 is spread and initially compressed up to a surface pressure of 4 mN m^{-1}. The monolayer is allowed to relax in the dark at constant area for about 250s. A UV lamp (model VL-6, VilberLourmat with 365nm wavelength, 0.05 W cm^{-2} power density at 15 cm) is subsequently switched on. Surface pressure rises rapidly due to *trans*-to-*cis* isomerization until reaching a maximum value followed by a steady drop. We interpret this behavior as a manifestation of the increased water solubility of the *cis* isomer[20]. BAM images (not shown) are unable to observe any features throughout this process, unlike the phase separation of *cis* and *trans* isomers clearly observed in monolayers of the analogue 8Az3COOH.

We have also studied monolayers prepared with an equimolar (racemic) mixture of (R/S)-7'Az3 in the *trans* form. Pressure/area isotherm data in Figure 2 reveal that mixed monolayers feature a condensation with respect to an ideal mixture of the

pure enantiomers, with a surface excess area of about 2 $Å^2$ $molec^{-1}$. Remarkably, BAM images show that this condensation is accompanied by the onset of orientational order in the monolayer, as revealed by the formation of textures with regions of very different reflectivity that changes if the BAM analyzer is rotated. This is a signature of optical birefringence (Figure 5), which is reminiscent of hexatic textures described in long-chain fatty acids [27] and for the achiral analogue 8Az3 at high lateral pressures [20, 28]. This hypothesis is confirmed below when lateral boundary conditions induce the formation of highly symmetric textures. The average size of the birefringent domains grows significantly with time for the first few minutes and remains unchanged, or changes much more slowly afterwards. Changes in the thermodynamic properties of racemic mixtures of Langmuir monolayers with respect to the pure enantiomers are not unusual [4, 5, 22], given the different possible packing arrangements at the air/water interface of pure enantiomers and racemic mixtures [7]. Compression of the racemic monolayer has no significant effect on the observed patterns until a pressure close to 10 mN m^{-1} is approached. Domains become fragmented and birefringence disappears rather abruptly (Figure 5, B and C). It is puzzling that this loss of birefringence is not accompanied by a detectable feature in the isotherm (Figure 2), as changes between a disordered and a hexatic phase usually involve a first order phase transition evidenced by a plateau in the isotherm. Moreover, one would expect the surface excess area to decrease when birefringence is lost, as ordering approaches that of the pure enantiomers. In other words, one would expect the isotherm of the racemic mixture to approach that of the pure enantiomers above 10 mN m^{-1}. It remains unclear why this does not happen. A possible explanation would be that the loss of optical contrast is due to a progressive untilting of the hydrophobic chains until they become oriented perpendicularly to the interface. This hypothesis, however, is refuted by experimental evidence below.

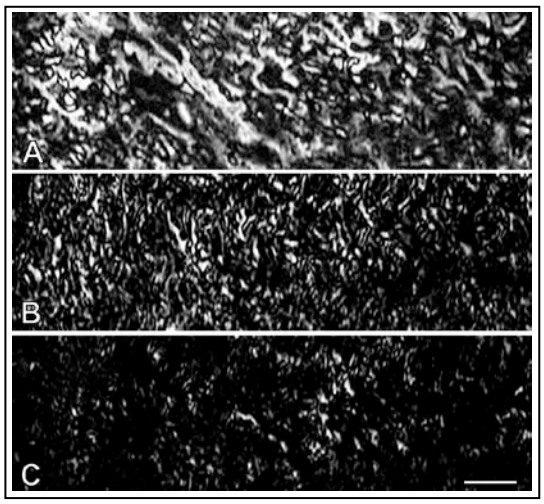

Figure 5. BAM images of a racemic mixture of (*S*)-7'Az3,(*R*)-7'Az3, revealing the onset of orientational order and its degradation upon compression. Lateral pressures are 1.0 mN m^{-1} (A), 9.7 mN m^{-1} (B), and 10.7 mN m^{-1} (C). The monolayer has relaxed at constant area for 30 minutes in (A). The line segment in (C) is 100 μm long.

Similarly to the procedures often employed in the liquid crystal literature, the nanoscale ordering of monolayer mesophases is typically inferred from the microscale BAM textures of highly symmetric configurations, which can be obtained in isolated submillimeter domains [23]. Boundaries impose anchoring conditions on the molecular orientation that are topologically incompatible with the nanoscale order, which results in the formation of point defects characteristic of the underlying order. In earlier experiments with the analogue 8Az3 [20], we could prepare isolated mesophase domains taking advantage of the spontaneous phase separation of the *cis* and *trans* isomeric forms, which results in the formation of pinwheel patterns, characteristic of hexatic phases. Following similar procedures, we generate here mesophase domains by spreading a monolayer with a *cis*-rich racemic mixture (previous irradiation with UV light of the spreading solution), allowing the slow spontaneous relaxation into the *trans* isomers and subsequent segregation and self-assembly of the *trans*-rich mesophase domains. Indeed, BAM images reveal the formation of the pinwheel patterns, organized in sectors of uniform reflectivity (uniform molecular orientation), an unambiguous signature of hexatic order [23] (Figure 6). Since the segregation of *trans*-rich and *cis*-rich domains is observed for the racemic mixture, the reason why such a segregation was not observed for the pure enantiomers was probably due to a lack of optical reflectivity contrast between the *cis*-rich and *trans*-rich domains in the latter case. The analysis of BAM micrographs of the isolated domains can be used to

characterize the orientational order of the surfactants. Since the total chain length and the position of the azobenzene moiety in (R/S) 7'Az3 is close to that in 8Az3COOH, we can use the optical dielectric properties of the latter [20] to perform calculations in the current system, yielding an estimate for the average tilt angle of about 45° with respect to the interface normal, and an average tilt oriented along the bisector in each circular sector of an isolated domain (Figure 6).

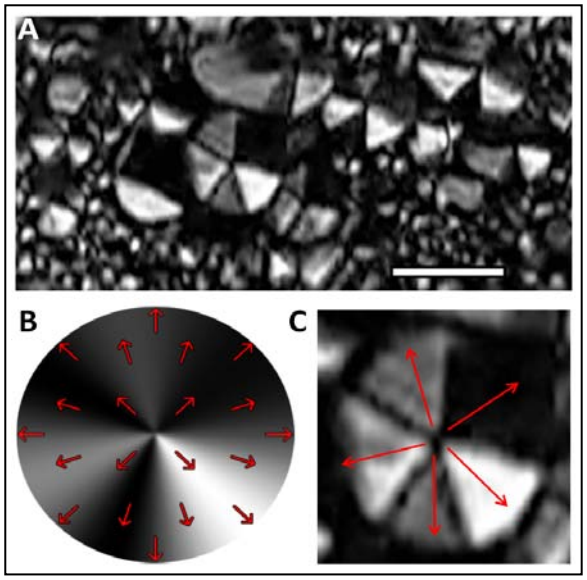

Figure 6.(A) BAM micrograph of *trans*-rich domains surrounded by a *cis*-rich matrix in a monolayer containing a racemic mixture of the chiral azobenzene surfactants.An optical analysis enables to relate the digitized reflectivity patterns with the modeled molecular order (B), which enables to obtain the local average in-plane molecular orientation (C). The ruler in (A) is 100 µm long.

We can take further advantage of these high symmetry configurations to ascertain whether the loss of contrast upon compression of the hexatic phase in the racemic mixture of (R/S) 7'Az3 is due to transition into a low-birefringence untilted phase (see above). If this were the case, the same structures observed before the loss of contrast at high pressure would be regained once the pressure is lowered before the transition threshold. We proceed by compressing a monolayer with structured domains such as that reported in Figure 6A until a pressure well above the loss of BAM contrast, and well below the collapse. We subsequently expand the monolayer until BAM contrast is regained. The result is that the recovered birefringent phase is now very fragmented, similar to a freshly spread monolayer, with no sign of the pinwheel patterns observed before compression. We thus conclude that the loss of contrast is accompanied with a loss of the hexatic order present at low pressures.

Compression beyond the collapse point results, for all monolayer compositions, in the nucleation and growth of submillimeter domains with multi-layer thickness, as revealed by the large increase in BAM reflectivity. One would expect these films to be tri-layers or, in general, be formed by an odd number of monolayers arranged head-to-head and tail-to-tail in order to always expose the hydrophobic tails to the air [22]. In fact, UV-vis spectroscopy performed on LB films obtained before and well after the collapse reveal that the reflected light intensity is roughly three times larger for the multilayer film, suggesting that, on average, monolayers collapse into tri-layers. The presence of orientational order inside the collapsed domains is revealed by their optical birefringence, which is made evident by rotating the BAM analyzer (Figures 7 and 8 for observations on LB films). We have qualitatively analyzed a number of collapsed domains obtained for the different system compositions with the purpose of evidencing a signature of heterochiral recognition similar to the one we have reported above for monolayers. Collapsed domains of the two enantiomers have compact shapes, with rough boundaries and an inner texture that often features spiral motifs (see Figure 7A), although no clear evidence for enantiomorphic configurations is observed when comparing multi-layer domains of the pure enantiomers. For the racemic mixture, collapsed domains are less compact in shape, featuring coexistence between regions with rough edges and inner texture with regions with both smooth edges and inner texture. As we see in the next section, a nanoscale ordering is evidenced in the collapsed domains after their transfer onto solid support.

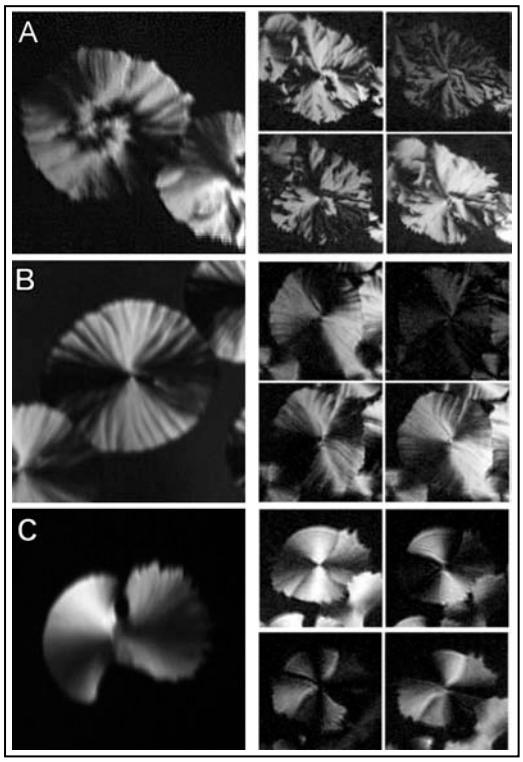

Figure 7.BAM micrographs of multi-layer domains prepared with pure (*S*)-3'Az7 (A), (*R*)-3'Az7 (B), and with a racemic mixture of the two (C). Images have been taken at the area per molecule at which lateral pressure exhibits a maximum (onset of collapse). Birefringence in these domains is evident by rotating the BAM analyzer (snapshots of a domain at four different analyzer orientations are shown on the right column next to each image). BAM laser intensity has been attenuated to compensate for the increased reflectivity of these thick films.

Figure 8. Polarizing reflection micrographs of a collapsed domain prepared with a racemic mixture of 3'Az7, and transferred on a SURF substrate using the LB technique. The sample is rotated in the different panels, as indicated by the arrow, to illustrate the birefringence of the collapsed domains. Images were taken eight weeks after LB transfer.

Langmuir-Bodgett films

Further information on the molecular arrangement in the multilayer domains nucleating upon monolayer collapse can be obtained by transferring the films onto solid support and performing atomic force microscopy (AFM) measurements on them. LB transfer took place just after monolayer collapse, maintaining constant the surface pressure during the process. BAM images acquired at the air/water interface prior to LB extraction (Figure 7) reveal the nucleation and growth of multilayer domains featuring long-range orientational order, which is evidenced by rotating the BAM analyzer. Given that both the typical domain size and their average spacing are larger than the range of our largest AFM scanner (70 μm), the ability to properly place the AFM tip on top of a domain is crucial in this case. We have therefore transferred the surfactant films onto engineered silicon substrates (SURF) that allow optical inspection of the thin films and performed AFM scans over regions whose structure is known at optical length scales thanks to the modified AFM header combined with a polarizing reflection microscope (see Experimental Section above). High resolution optical micrographs reveal that the domain morphology is preserved by the LB transfer process, including their birefringent nature, and hint at a nanostructure that could not be resolved by means of BAM imaging (See Figure 8). Since there is no strong bond between the carboxylic group of our surfactant molecules and the SiO_2 surface, films tend to desorb and surfactant micro-crystals grow after a few hours. As a result, LB films of the pure enantiomers inspected weeks after their transfer have degraded, and the original domain structure is no longer observable. In the case of films prepared with the racemic mixture, film stability is noticeably enhanced. For instance, in Figure 8 we report micrographs of a LB film that was eight weeks old. In this case, only modest film degradation is detected.

Our AFM data clearly reveal that collapsed domains are formed by isolated, micrometer-size elongated multilayer subdomains (Figure 9) arranged in a nematic-like local orientational order, which is presumably the cause of the detected optical birefringence under BAM observation. In the case of films of the pure enantiomers, the orientation of elongated subdomains changes continuously around the center of the

parent domain, while in the case of films of the racemic mixture, the parent domain is organized in regions inside of which elongated subdomains remain roughly parallel.

We have measured the thickness profile across the main features observed on AFM scans of the LB films (Figure 9). For the films of the pure enantiomers, most elongated domains have an average thickness of 5.0 nm above the lowest level. There are a few scattered features whose thickness is either 2.5 nm or 7.5 nm above the baseline level, indicating a characteristic step size of 2.5 nm. For the films prepared with the racemic mixure, scattered elongated domains are 4.0 nm thicker than the baseline level, and they stand 2.0 nm above a uniform continuous region that stands 2.0 nm above the baseline level (Figure 9). In order to interpret these measurements, we have estimated the length of the chiral azobenzene surfactant molecules, which is approximately 2.5 nm [29]. The most likely arrangement for the collapsing monolayer is to spontaneously organize in the so-called Y type film [29], in which stacked monolayers arrange in a head-to-head or tail-to-tail fashion, always exposing hydrophobic tails to the air. Consequently, one expects that the baseline region on the LB films, which have been transferred by a single upstroke, corresponds to the first monolayer, and that subsequent steps correspond to bilayers. This is consistent with UV-vis measurements performed on LB films obtained for fully collapsed monolayers (Figure 3). Data indicate an absorbance roughly three times large for the collapsed monolayers than for the single monolayer LB films, indeed suggesting that the former are trilayers on average. In order to understand the measured bilayer thickness when compared to the estimated molecular length we need to take into account that molecules are most likely tilted with respect to the interface normal, as suggested by the optical birefringence of collapsed domains (birefringence is maximal when the optical axis of the material is perpendicular to the light path). A final aspect that must be taken into account to interpret molecular arrangement inside collapsed domains is the insertion of hydrophobic chains in adjacent monolayers, which has been suggested to be significant in similar systems [22]. In the case of LB films of the racemic mixture, one can take as a reference value the tilt angle that we have estimated from the analysis of BAM micrographs of hexatic domains (see above), namely $\theta = 45°$. With this, the thickness of a bilayer, ignoring chain insertion, would be 3.6 nm. In consequence, the measured bilayer thickness (step height reported above) would

imply a chain insertion of about 1.6 nm for films of the racemic mixture, and 1.1 nm in the case of films of the pure enantiomers. The increased chain insertion in racemic films is consistent with the enhancement in the film stability reported above. Chain insertion also favors interaction between molecules in adjacent monolayers, as is evidenced by the bathochromic shift observed in UV-vis spectra of multilayers (Figure 3).

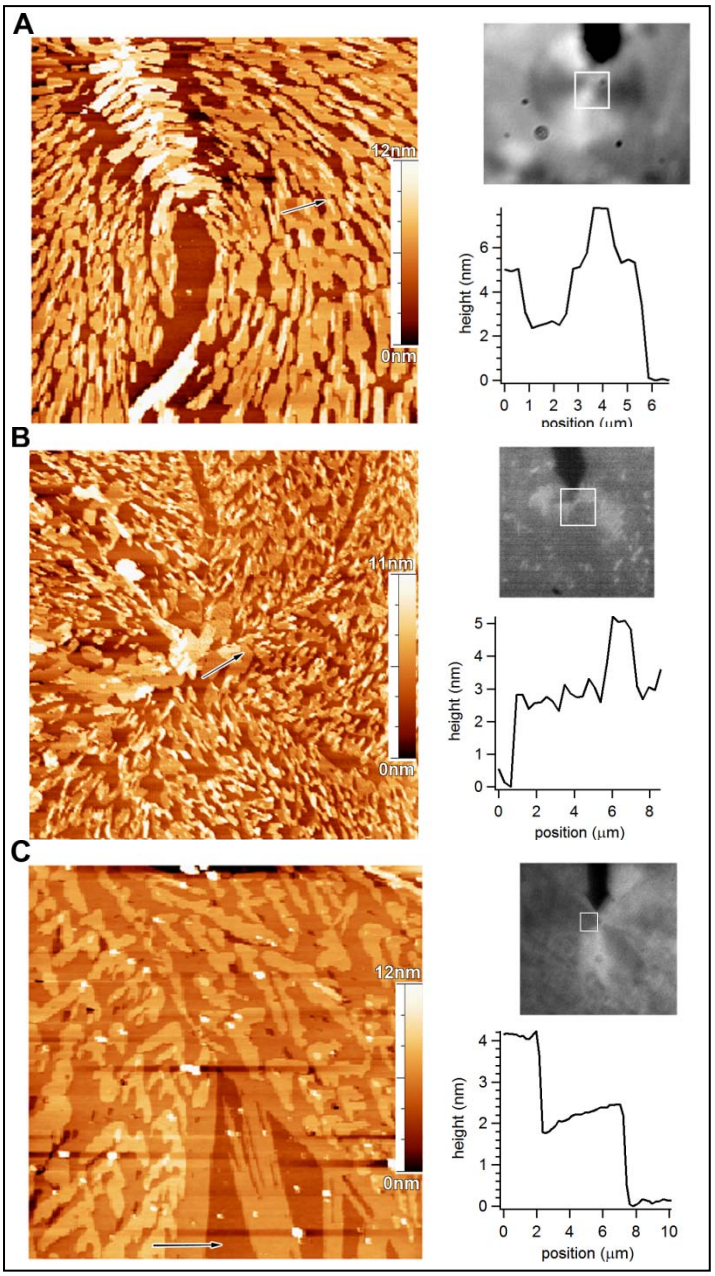

Figure 9. AFM topography scans of a region near the center of a collapsed domain in LB films on SURF substrates of chiral azobenzene surfactants at different compositions. To the right of each AFM image an optical micrograph shows the location of the scanned region, marked with a white square, as observed by in-situ polarizing reflection microscopy. The height profile along a linear path, marked by an arrow on the AFM image, is also included to the right of the image. Film composition and scanned window sizes are (*S*)-7'Az3, 70×70 μm^2 (A); (*R*)-7'Az3, 70×70 μm^2 (B); racemic mixture of the two surfactants, 50×50 μm^2 (C).

3.3.4 Conclusions

We have reported studies of the assembly behaviour of chiral azobenzene surfactants at the air/water interface. While the presence of the chiral center in the

hydrophobic chain hampers the ability of *trans* isomers of these compounds to form mesophases (compared to achiral analogues), a significant heterochiral recognition is observed in monolayers prepared with the racemic mixture. This is evidenced during Brewster angle microscopy observations, which reveal the formation of a mesophase. By preparing monolayers in the form of isolated *trans*-azobenzene rich domains, the nanoscale ordering couples with the anisotropic boundary conditions at the domain boundary, resulting in textures that unambiguously indicated the formation of a hexatic phase. Following previously described methods we have been able to characterize the orientational order at the mesoscale, in particular the average orientation of tilted hydrophobic chains. Compression of the hexatic racemic monolayer leads to a transition into a non-birefringent phase. Although hexatic order is regained upon expansion, the range of the tilt-orientational order is severely diminished. Further studies involving grazing-incidence x-ray diffraction and spectroscopic techniques would be needed to propose a model that fully characterizes the arrangement of the two enantiomers in the hexatic lattice of the mesophase, to understand the changes that take place upon compression from an ordered into a disordered phase, and to compare the molecular arrangement of the disordered racemic phase with that in the disordered phases observed for pure enantiomers. For all compositions, high compression leads to film collapse into ordered stacks of odd-number monolayers, with the formation of submillimeter birefringent crystallites featuring an inner nanostructure, as revealed by AFM studies of LB-transferred films. Under these conditions, interlayer penetration is enhanced for the racemic mixture.

The observed heterochiral recognition effects could be explored under adsorption at different interfaces. Recently, Iavicoli et al. [30] reported that the presence or absence of spontaneous resolution of a racemate of self-assembling surfactants is dramatically dependent on the nature of the support surface. In our case, the adsorption of the chiral azobenzene surfactants could be studied at the solution/solid interface during the formation of self-assembled monolayers, or at the liquid crystal/water interface, which is known to amplify changes in the mesoscale ordering of adsorbed species [31]. In the latter context, structured monolayers of achiral analogues of these compounds have also been employed successfully to

pattern substrates via the LB technique showing that this can be a new strategy to structure liquid crystal devices at the microscale [32]. In fact, the Langmuir-Blodgett technique has recently been acknowledged to offer a new bottom-up approach to pattern surfaces with large areas with well-defined microstructures, which may be employed as an interface between biological systems and material science [33].

3.3.5 References

[1] D. Vollhardt, N. Nandi, S. D. Banik. *Phys. Chem. Chem. Phys.*, **13**, 4812 (2011).

[2] M. C. Petty. *Langmuir-Blodgett films: an introduction*. Cambridge University Press, Cambridge (1996).

[3] K. Ariga, T. Michinobu, T. Nakanishi, J. Hill. *Curr. Opin. Colloid Interface Sci.*, **13**, 23 (2008).

[4] E. M. Arnett, N. G. Harvey, P. L. Rose. Acc. Chem. Res., **22**, 131 (1989).

[5] I. Kuzmenko, K. Kjaer, J. Als-Nielsen, M. Lahav, L. Leiserowitz. *J. Am. Chem. Soc.*, **121**, 2657 (1999).

[6] W. Mamdouh, I. H. Uji, A. E. Dulcey, V. Percec, S. De Feyter, F. C. De Schryver. *Langmuir*, **20**, 7678 (2004).

[7] I. Weissbuch, L. Leiserowitz, M. Lahav. *Curr. Opin. Colloid Interface Sci.*, **13**, 12 (2008).

[8] N. Nandi, D. Vollhardt. *Chem. Rev*., **103**, 4033 (2003).

[9] E. Jimenez-Millan, J. J. Giner-Casares, M. T. Martin-Romero, G. Brezesinski, L. Camacho. *J. Am. Chem. Soc*., **133**, 19028 (2011).

[10] J. Ignés-Mullol, J. Claret, F. Sagués. *J. Phys. Chem. B*, **108**, 612 (2004).

[11] N. Nandi, D. Vollhardt. *Curr. Opin. Colloid Interface Sci*., **13**, 40 (2008).

[12] V. Percec, A. D. Asandei, Q. Zheng. *J. Polym. Sci., Part A: Polym. Chem*, **38**, 3631 (2000).

[13] V. Percec, H. Oda. *Macromolecules*, **27**, 5821 (1994).

[14] H. Zepik, E. Shavit, M. Tang, T. R. Jensen, K. Kjaer, G. Bolbach, L. Leiserowitz, I. Weissbuch, M. Lahav. *Science*, **295**, 1266 (2002).

[15] X. Zhu, Y. Li, P. Duan, M. Liu. *Chemistry*, **16**, 8034 (2010).

[16] H. Cao, X. Zhu, M. Liu. *Angew. Chem., Int. Ed.*, **52**, 4122 (2013).

[17] T. Seki, M. Sakuragi, Y. Kawanishi, T. Tamaki, R. Fukuda, K. Ichimura, Y. Suzuki. *Langmuir*, **9**, 211 (1993).

[18] J. Ignés-Mullol, J. Claret, R. Reigada, F. Sagués. *Phys. Rep*., **448**, 163 (2007).

[19] Y. Tabe, T. Yamamoto, H. Yokoyama. *New J. Phys*., **5**, 65 (2003).

[20] J. Crusats, R. Albalat, J. Claret, J. Ignés-Mullol, F. Sagués. *Langmuir*, **20**, 8688 (2004).

[21] N. Petit-Garrido, J. Claret, J. Ignés-Mullol, F. Sagués. *Nat. Commun*., **3**, 1001 (2012).

[22] M. Haro, J. del Barrio, A. Villares, L. Oriol, P. Cea, M. C. Lopez. *Langmuir*, **24**, 10196 (2008).

[23] T. M. Fischer, R. F. Bruinsma, C. M. Knobler. *Phys. Rev. E*, **50**, 413 (1994).

[24] I. Horcas, R. Fernandez, J. M. Gomez-Rodriguez, J. Colchero, J. Gomez-Herrero, A. M. Baro. *Rev. Sci. Instrum*., **78**, 13705 (2007).

[25] M. Amaike, H. Kobayashi, K. Sakurai, S. Shinkai. *Supramol. Chem*., **14**, 245 (2002).

[26] J. -M. Pedrosa, M. T. T. Romero, L. Camacho, D. Möbius. *J. Phys. Chem. B*, **106**, 2588 (2002).

[27] J. Ignés-Mullol, D. K. Schwartz. *Langmuir*, **17**, 3017 (2001).

[28] M. K. Durbin, A. Malik, A. G. Richter, C. J. Yu, R. Eisenhower, P. Dutta. *Langmuir*, **14**, 899 (1998).

[29] M. D. Hanwell, D. E. Curtis, D. C. Lonie, T. Vandermeersch, E. Zurek, G. R. Hutchison. *J. Chem inf*., **4**, 17 (2012).

[30] P. Iavicoli, H. Xu, T. Keszthelyi, J. Telegdi, K. Wurst, B. Van Averbeke, W. J. Saletra, A. Minoia, D. Beljonne, R. Lazzaroni, S. De Feyter, D. B. Amabilino. *Chirality*, **24**, 155 (2012).

[31] Y. Bai, N. L. Abbott. *Langmuir*, **27** (2011).

[32] N. Petit-Garrido, R. Trivedi, J. Ignés-Mullol, J. Claret, C. Lapointe, F. Sagués, I. Smalyukh. *Phys. Rev. Lett*., **107**, 177801 (2011).

[33] X. Chen, S. Lenhert, M. Hirtz, N. Lu, H. Fuchs, L. Chi. *Acc. Chem. Res*., **40** (2007).

CHAPTER 3.4

INDUCTION AND SELECTION OF CHIRALITY OF A 8Az5COOH MONOLAYER

3.4.1 Introduction

Chiral symmetry breaking is a widely studied phenomenon relevant in materials science, due to its applicability in self-assembling processes [1] and asymmetric catalysis [2], as well as in chemistry or in soft-matter research [3-8]. In the latter area, many two-dimensional systems giving chiral structures have been reported [5, 9-14], and in particular, the chiral selection of self-assembled achiral molecules forming a monolayer at the air-water interface, by means of either a chemical modifier or a chiral force like a hydrodynamic vortex [15, 16, 17]. In their studies *Petit-Garrido et. al.* work with mixed *cis-trans* Langmuir monolayers of the azobenzene molecule 8Az3COOH. This system behaves as a 2-dimensional emulsion composed of *trans*-rich birefringent circular domains, embedded in an isotropic *cis*-rich phase, and although the amphiphilic molecule forming the monolayer is achiral, the *trans*-rich circular domains display a random chirality. When the system evolves in the absence of any chiral force or chiral dopant, the distribution of chiral *trans*-rich domains is racemic, both clockwise (CW) and counter-clockwise (CCW) configurations are equally represented. In further studies, *Petit-Garrido et. al*. show that the orientational chirality of these circular *trans*-rich domains can be selected by applying a vortical flow to the aqueous bulk phase underneath the air-water interface, and quantified by an enantiomorphic excess parameter. What is more, they also prove that a well-defined handedness on the orientational chirality of the *trans*-rich domains can be induced by adding a chiral modifier to the system, which is chemically compatible with the 8Az3COOH monolayer. In addition, when both chiral selectors are combined, their effect can be opposed or enhanced.

A preliminary study of the effect of chiral modifiers and vortical flow over a monolayer of an azobenzene derivative similar to the previously studied (8Az3COOH) is here reported. Our experimental system consists of Langmuir monolayers of an homologue compound, 4-octyl-4'-(5-carboxy-pentamethylene-oxy)azobenzene (8Az5COOH), which also presents a *cis-trans* photoisomerisation giving a 2D emulsion, where *trans*-rich domains are surrounded by a *cis*-rich matrix. Such domains present two diametrically opposite point singularities on the boundary of the domain. By BAM, images of these birefringent domains can be captured and their reflectivity analysed, concluding that the molecules are organized pointing from one of the defects to the other (double boojum configuration). When the monolayer is doped with a certain quantity of a chiral modifier, the *trans*-rich domains become chiral displaying a boojum configuration, with one singularity placed at the edge of the domain and the molecular azimuths organised around the defect. Moreover, the influence of a chiral 3D force, a vortical flow, in combination with the chemical induction of chirality has been explored in our system, in a first attempt to compare the chiral behaviour of a 8Az5COOH monolayer.

3.4.2 Experimental section

The experimental setup used in the following experiments is described in section 3.1.2.2. Monolayers are prepared spreading at the air-water interface drops of a chloroform solution (1mg/ml) of 8Az5COOH, or 8Az5COOH doped with a 6% wt. of the chiral modifier (R/S-enantiomer) as described in section 3.1.2.2. Temperature is kept at 20°C ± 0.2 °C. In order to resolve the chiral organisation of molecules in the monolayer, BAM images are recorded using a hard disk video recorder, and digital image analysis is performed with the software ImageJ [18].

3.4.3 Results and discussion

In order to be able to obtain *cis-trans* mixed monolayers with bigger and well formed domains, we spread a nearly pure *cis* solution of 8Az5COOH at constant

temperature and area, and we let it evolve under room light. Since *cis-trans* relaxation is occurring, *trans* rich domains form and grow. Approximately 45 minutes after the spreading step, the domains are big enough to be analysed and their inner texture can be resolved fitting their BAM reflectivity to a suitable spatial distribution of the azimuth field, by means of an optical model (see section *3.2.3 Monolayers of a cis-trans mixture)* [18, 19, 20]. The majority of circular *trans*-rich domains display a double-boojum configuration with two defects pinched at opposite poles, where the molecular azimuth field departs from a point defect on one of the poles, with the field lines parallel to the domain boundary, and converges towards the opposed pole (Figure 1). The lack of chirality of those entities presents the major difference with the shorter homologue 8Az3COOH. When working at the same experimental conditions, 8Az3COOH presents a phase separated *cis*-tran mixed monolayer with circular bend-like *trans*-rich domains, which perform a chiral organisation of molecular azimuths around a central defect perpendicularly to the radial direction (Figure 2B). These bend-like domains apparently come from the coalescence of pairs of precursor elliptical domains with antiparallel molecular orientations, and their chirality reflects the relative orientation of their parent ellipses [15, 16]. The elliptic domains feature two defects at the equatorial poles, one defect strictly pinched at the domain boundary whereas the other defect escapes towards the surrounding *cis*-rich matrix (Figure 2A). When temperature is increased above 35 °C the lability of the monolayer increases, the elliptical *trans* domains become unstable and transform into circular domains displaying a double-boojum configuration, and so chiral discrimination disappears in these monolayers [16]. Considering the increase in the monolayer lability to have a similar effect to that of an increase in the miscibility of *cis* and *trans* isomers, these observations are in agreement with the conclusions in section 3.2.3 *Monolayers of a cis-trans mixture* [19]. In that section we found evidences that the longer compound 8Az5COOH presents a higher miscibility between the *cis* and *trans* isomers in monolayer form, which could explain the straight formation of achiral entities with double-boojum configuration instead of forming elliptical domains.

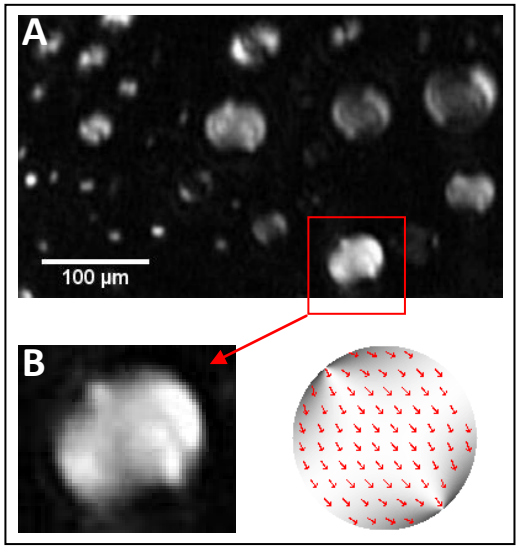

Figure 1. (A) BAM micrograph of a *cis-trans* 8Az5COOH monolayer at 20°C and low surface pressure. (B) *Trans*-rich domain performing a double boojum configuration and a sketch showing the orientational field of the surfactant molecules together with the simulated BAM image.

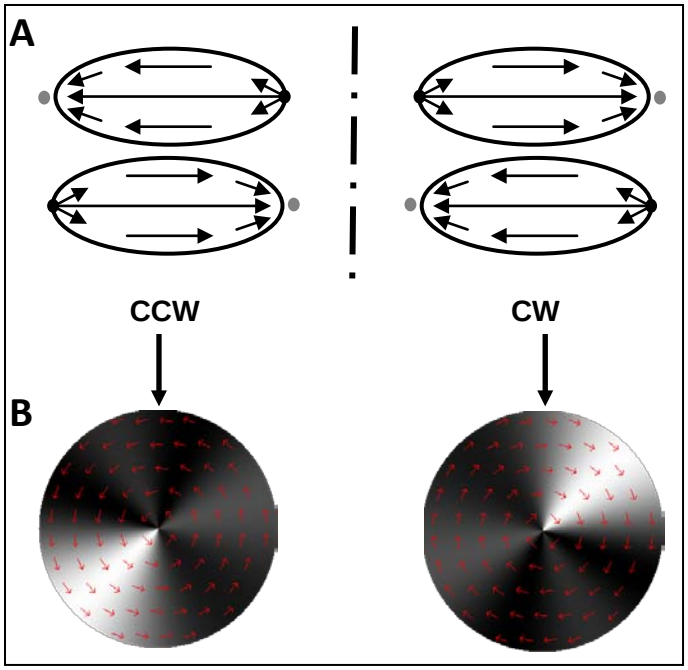

Figure 2. (A) Sketch of two antiparallel coalescing elliptical domains leading to the formation of (B) two bend circular domains; CCW (left), CW (right). Arrows represent the local orientation of amphiphilic molecules. Dots in (A) denote the two asymmetric equatorial defects at the poles of the ellipses.

A determinate chirality in the *trans*-rich domains appears when we add a small amount of a chiral surfactant modifier ((S/R)-(+/–)-4-[4-[4-(1-methylheptyloxy phenyl) azo]phenoxy]butanoic acid, studied in chapter 3.3 [21]) to the 8Az5COOH chloroform solution, prior to dispersion. The circular *trans*-rich domains that featured two

opposed singular defects at the domain boundary perform now a boojum configuration, where the two defects have migrated to form one singularity placed at the edge of the domain (Figure 3). In this configuration, the azimuths organise around the defect perpendicularly to the radial direction, giving a clockwise (CW, corresponding to the addition of S-enantiomer) or counter clockwise orientation (CCW, corresponding to an R-enantiomer addition) (see Figure 4).

Figure 3. BAM micrograph of a *cis-trans* 8Az5COOH monolayer doped with a 6% of S-enantiomer, at 20°C and low surface pressure.

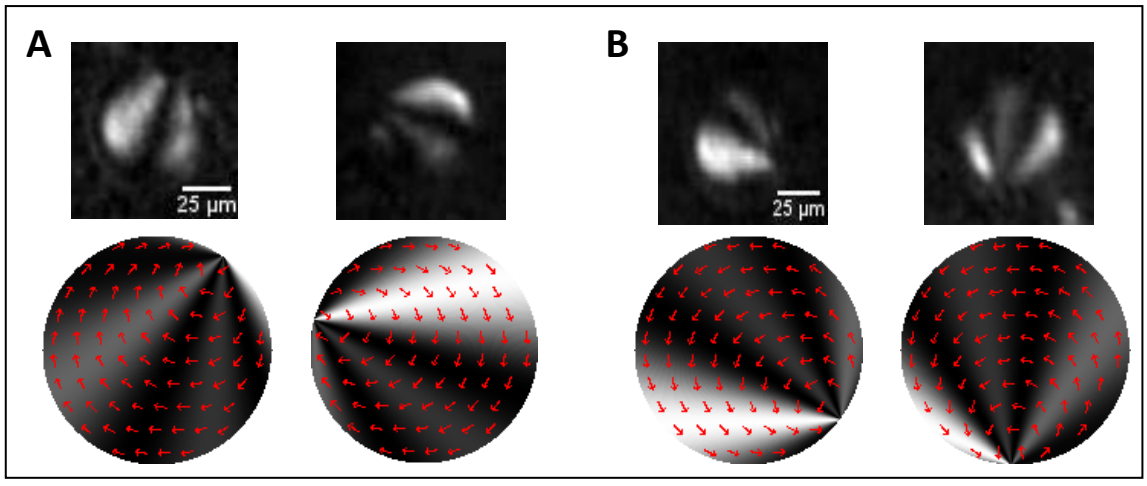

Figure 4. BAM images of (A) CW boojum domains and (B) CCW boojums domains (up), and a sketch of the local in-plane orientational field with the corresponding simulated BAM image (below).

The dominance of a particular chirality is measured in terms of the enantiomorphic excess (*ee*) of domains with a particular sign,

$$ee = \frac{2n_{CW} - n_T}{n_T} 100, \quad (1)$$

where CW is the chosen chirality and n_{CW} stands for the number of CW domains with respect to the total number n_T , which is around 200 in a typical experiment. Experimental results indicate that a neat handedness selection takes place when the monolayer is doped with a 6% of *R/S*-enantiomer, and that total discrimination is observed: 100% of the counted domains display the chirality induced by the chiral modifier (CW in the case of *S*-enantiomer addition, and CCW in the case of *R*-enantiomer addition).

To test the effect of vortical shearing we now proceed by spreading the *cis* 8Az5COOH solution while gently stirring the aqueous subphase. Stirring is maintained during 30 minutes while *cis-trans* conversion is taking place and *trans*-rich domains are formed. After stopping stirring, BAM images of the monolayer are recorded. Experimental results show the appearance of chiral bend like domains in the monolayer, presenting a neat handedness selection which correlates with the stirring sense of the spinning bar: CW stirring favours the formation of CW domains, while CCW stirring favours the formation of CCW domains (Figure 5). In addition, the enantiomorphic excess of bend domains ($ee_{Bend\ CW}$) is calculated by means of equation 1 for each case, giving the values summarised in Table 1.

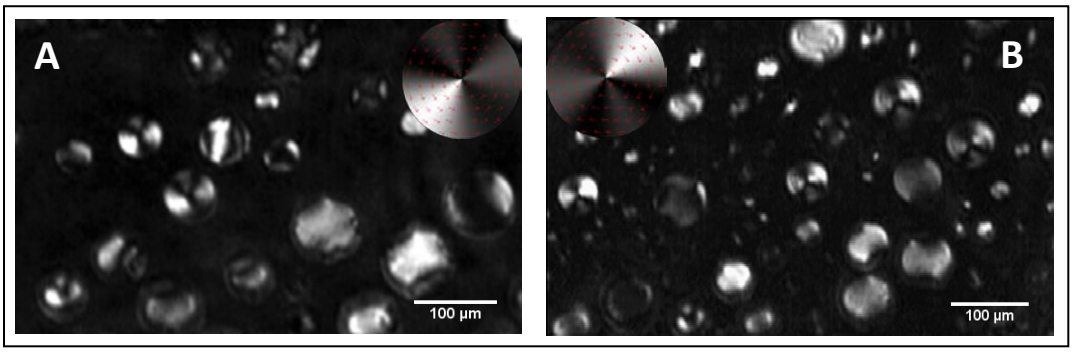

Figure 5. BAM images of *cis-trans* 8Az5COOH monolayers at low pressures, (A) after 30 minutes of CCW stirring at Ω=1000 rpm, and (B) after 30 minutes of CW stirring at Ω=1000 rpm. A sketch of the domains found in the images is shown at the upper right part of the image (A), and at the upper left part (B).

Stirring sense	ee_{CW}
CW	30 %
CCW	-28 %

Table 1. $ee_{Bend\ CW}$ values for bend-like domains appeared after 30 minutes stirring CW or CCW at Ω = 1000 rpm.

Furthermore, the effect of vortical shearing has been tested over a 8Az5COOH monolayer doped with a 6% of *R/S*-chiral modifier. In this case, the majority of the obtained *trans*-rich domains perform a boojum configuration; however there is a certain amount of bend-like domains that only appear when stirring is involved in the process. If we count boojum domains and calculate the corresponding enantiomorphic excess ($ee_{Boojum\ CW}$) when stirring CW and CCW, for a monolayer doped with *R* or *S*-enantiomer, we can clearly conclude that the chiral dopant has a significant effect on the monolayer configuration even in the cases where the stirring sense is contrary to the chirality induced by the dopant (see Table 2). On the other hand, when focusing only in bend domains, experimental results have much more dispersion and a conclusion on the effect and competence of the chiral modifier and the chiral force can not be proposed. Further experiments are needed in order to complete the observations done.

Chiral modifier	Stirring sense	ee_{CW}
S-enantiomer	CW	~ 100 %
	CCW	~ 88 %
R-enantiomer	CW	~ -92 %
	CCW	~ -100 %

Table 2. $ee_{Boojum\ CW}$ values for boojum domains, after stirring 30 minutes a doped monolayer at Ω = 1000 rpm.

3.4.4 Conclusions

We have reported a first exploration of the chiral behaviour of 8Az5COOH Langmuir monolayers at the air/water interface. In particular, we have studied the response of the azobenzene derivative to the addition of a chemical modifier and a 3D vortex flow, in comparison to the behaviour of a shorter homologue (8Az3COOH). We focus on isolated domains that appear when the *cis* and *trans* isomers of the surfactant coexist in the monolayer. The orientational order of these domains is resolved by Brewster angle microscopy, evidencing the main difference between both analogues: 8Az5COOH is not forming chiral domains at the explored conditions, probably due to a higher miscibility between its *cis* and *trans* isomers. In the presence of a chemical chiral modifier the domains become chiral, and total chiral selection is observed indicating a good compatibility of the dopant with the surfactant. By stirring the aqueous subphase the orientational chirality can be controlled, however when the monolayer is doped with a chiral modifier its effect is predominant.

In summary, we have shown that despite the similarity between the two homologues, its chiral behaviour is different according to the differences in thermodynamic behaviour found in chapter 3.2. It must be remarked that the present study is an introductory exploration of the chirality of a 8Az5COOH monolayer, so an extension of this work would be interesting in order to explore different temperature and pressure conditions which would complete the information found.

3.4.5 References

[1] G. M. Whitesides, J. P. Mathias, C. Seto. *Science*, **254**, 1312 (1991).

[2] I. Lee, Z. Ma, S. Kaneko, F. Zaera. *Journal of the American Chemical Society*, **130**, 14597 (2008).

[3] P. Cintas. *Angewandte Chemie International Edition*, **41**, 1139 (2002).

[4] J. J. L. M. Cornelissen, A. E. Rowan, R. J. M. Nolte, N. A.J.M. Somerdijk. *Chemical Reviews*, **101**, 4039 (2001).

[5] L. Pérez-García, D. Amabilino. *Chemical Society Reviews*, **36**, 941 (2007).

[6] D. Pijper, B. L. Feringa. *Soft Matter*, **4**, 1349-1372 (2008).

[7] M. A. Mateos-Timoneda, M. Crego-Calama, D. N. Reinhoudt. *Chemical Society Reviews*, **33**, 363-372 (2004).

[8] I. Kuzmenko, H. Rapaport, K. Kjaer, J. Als-Nielsen, I. Weissbuch, M. Lahav, L. Leiserowitz. *Chemical Reviews*, **101**, 1659-1696 (2001).

[9] W. Dzwolak, A. Loksztejn, A. Galinska-Rakoczy, R. Adachi, Y. Goto, L. Rupnicki. *Journal of the American Chemical Society,* **129**, 7517 (2007).

[10] J. M. Ribó, J. Crusats, F. Sagués, J. Claret, R. Rubires. *Science*, **292**, 2063 (2001).

[11] J. Crusats, J. Claret, I. Díez-Pérez, Z. El-Hachemi, H. Garcia-Ortega, R. Rubires, F. Sagués, J. M. Ribó. *Chemical Communications*, 1588 (2003).

[12] O. Ohno, Y. Kaizu, H. Kobayashi. *Journal of Chemical Physics*, **99**, 4128 (1993).

[13] N. Nandi, D. Vollhardt. *Chemical Reviews*, **103**, 4033-4075 (2003).

[14] R. Viswanathan, J. A. Zasadzinski, D. K. Schwartz. *Nature*, **368**, 440-443 (1994).

[15] N. Petit-Garrido, J. Ignés-Mullol, J. Claret, F. Sagués. *Physical Review Letters*, **103**, 237802 (2009).

[16] N. Petit-Garrido, J.Claret, J. Ignés-Mullol, J.A. Farrera, F.Sagués. *Chemistry*, **18**, 3975-3980 (2012).

[17] N. Petit-Garrido, J. Claret, J. Ignés-Mullol, F. Sagués. *Nature Communications*, **3**, 1001 (2012).

[18] J. Ignés-Mullol, J. Claret, F. Sagués. *J. Phys. Chem. B*, **108** (2), 612-619 (2004).

[19] A. Pulido-Companys, J. Ignés-Mullol. *Journal of Colloid and Interface Science*, **352**, 449-455 (2010).

[20] J. Ignés-Mullol, J. Claret, R. Albalat, J. Crusats, R. Reigada, M. T. Martín-Romero, F. Sagués. *Langmuir*, **21**, 2948-2955 (2005).

[21] A. Pulido-Companys, R. Albalat, J. Garcia-Amorós, D. Velasco, J. Ignés-Mullol. *Langmuir*, **29**, 9635-9642 (2013).

CHAPTER 4

TWO-DIMENSIONAL MICROFLUIDICS

SECTION 4.1

EXPERIMENTAL SYSTEM

4.1.1 Langmuir monolayers for two-dimensional microfluidics experiments

In this section, the different molecules used to prepare Langmuir monolayers for two-dimensional microfluidics experiments will be introduced.

Diffusion experiments and monolayer's velocity profile

To follow the diffusion of a species present in a two-dimensional system, we have chosen a phospholipid monolayer, which presents an expanded phase at the working temperature and pressure, and is stable at the air/water interface, and a fluorescent dye to dope the phospholipid monolayer, which allows to monitor its diffusion by Fluorescence Microscopy. The chosen phospholipid is 1,2-dimyristoyl-sn-glycero-3-phosphocholine (DMPC, Sigma, >99 %, MW=677.93 g·mol^{-1}), which is a neutral lipid from the Phosphatidylcholines (PC) family, present in the cellular membrane of animals and plants, and in the pulmonary surfactant (Figure 1) [1, 2]. The fluorescent dye we use is Texas Red DHPE (N-(Texas Red sulfonyl)-(1,2-dihexadecanoyl-sn-glycero-3-phosphoethanolamine, triethylammonium salt), MW=625.15 g·mol^{-1}, Life Technologies), an amphiphilic molecule commonly used in biologic assays [3], soluble in volatile solvents and which forms monolayers at the air/water interface. Its adsorption spectrum has a peak at 595 nm, and it fluoresces at about 615 nm (Figure 2). We add a small amount of TR-DHPE in the phospholipid monolayer, in the range of 1-2%, a quantity that is enough to allow the visualisation of the monolayer, but is not perturbing its properties. In all experiments, hydrophobic silica particles are added to act as tracers and allow measuring the monolayer velocity.

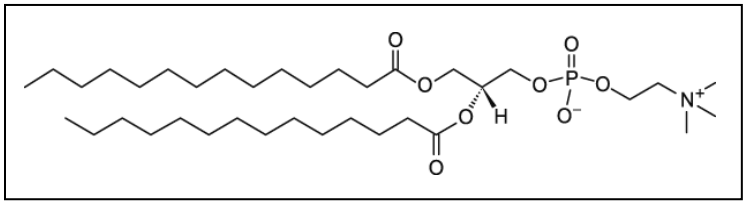

Figure 1. Molecular structure of DMPC.

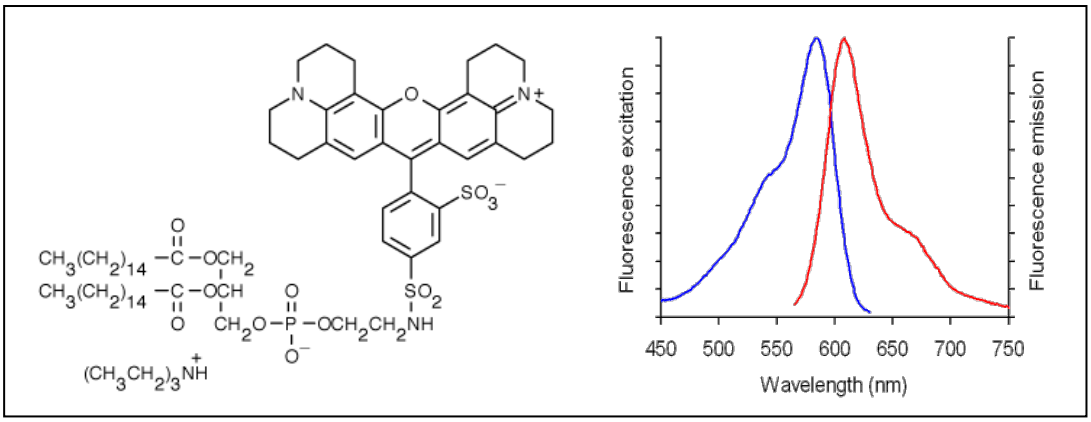

Figure 2. Molecular structure of the fluorescent dye Texas Red DHPE, and its fluorescence spectra [4].

Two-dimensional dissolution

For the observation of the dissolution of a "solid-like" monolayer by a "liquid-like" monolayer, we have used the expanded phase formed by DMPC as a solvent, and a hexatic monolayer formed by 1-monopalmitoyl-rac-glycerol (C16:0) (MPG, Aldrich) as a solute. MPG is a saturated fatty acid, a carboxylic acid with a long aliphatic tail, linked to a glycerol molecule, which, when spread on the water surface, undergoes a phase transition upon compression of the monolayer. At appropriate surface pressures ($\pi > 9$ $mN \cdot m^{-1}$), MPG forms a hexatic phase (Figure 3).

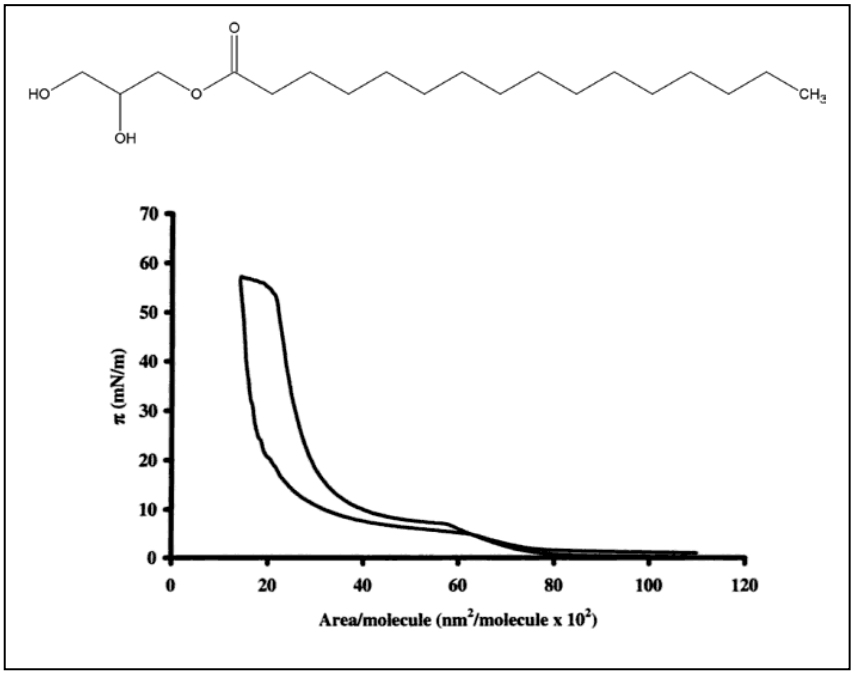

Figure 3. Chemical structure of MPG, and surface pressure-molecular area isotherm [5].

Two-dimensional reaction

In order to observe a reaction in the contact line between different monolayers, we have chosen two amphiphilic molecules that would presumably react to form a precipitate, inspired in the chemical reaction of copper (II) sulfide precipitation in bulk. Those molecules are 1-Octadecanethiol ($C_{18}H_{37}SH$, 98%, Aldrich), and the custom synthesized (Cu^{2+})EDTA-C_{18} diamide, which is a modified EDTA molecule with two alkyl chains to turn it amphiphilic, and which is encapsulating a Cu^{2+} atom (Figure 4) [6].

Another system explored to visualize a reaction in the interface between monolayers involves the chiral molecules *R* and *S*-7'Az3, introduced in chapter 3 (see section 3.1.1), that would presumably undergo a heterochiral molecular recognition to form a more condensed racemic phase.

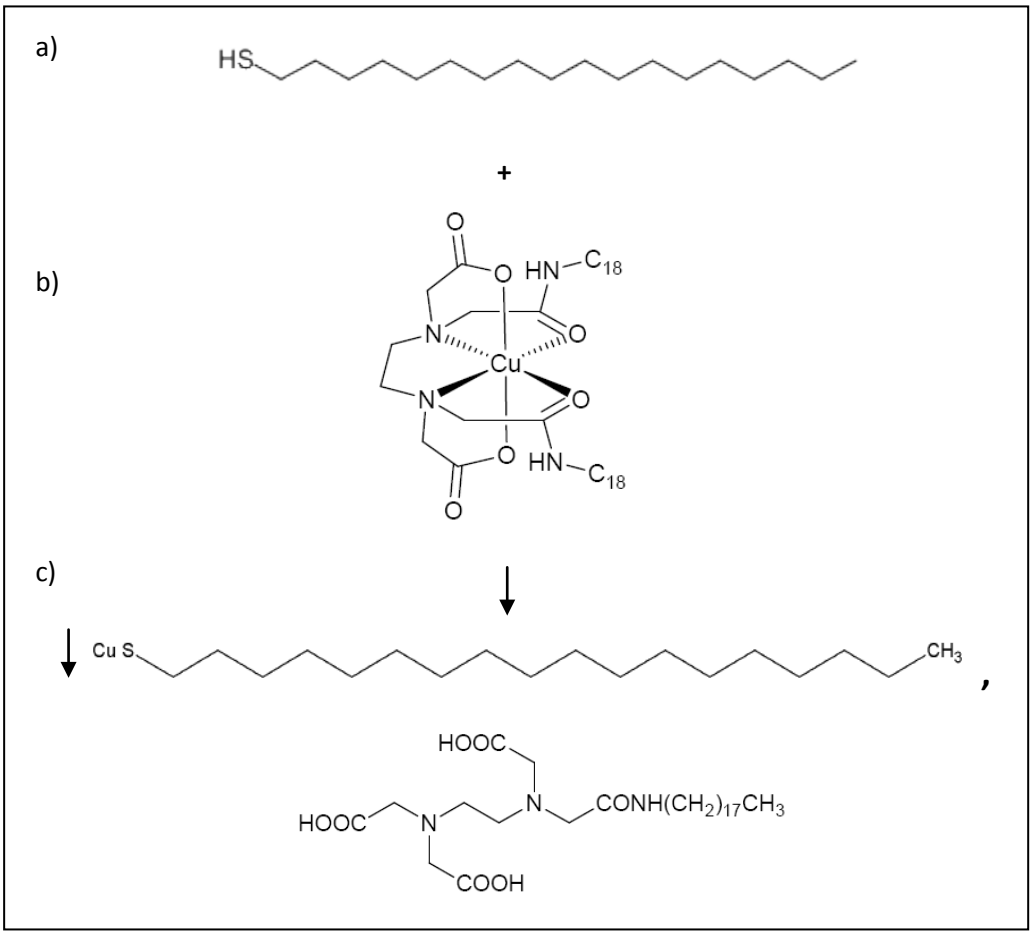

Figure 4. Molecular structure of (a) 1-Octadecanethiol and (b) (Cu^{2+})EDTA-C_{18} diamide. (c) Schematic representation of the hypothetical reaction products.

4.1.2 Experimental protocols

On what follows, a general explanation for the spreading of monolayers that will flow through a circuit, and the different protocols involved in the preparation of the experiments are given.

Production of wettability contrast circuits

In order to perform a two-dimensional microfluidics experiment, where monolayers will flow through a channel, different types of circuit design and materials were used. For circuits with an engraved pattern, materials like brass or Delrin were machined to obtain the desired design, but for the production of flat wettability

contrast circuits a specific protocol, involving photolithographic techniques and the formation of self-assembled monolayers (SAMs), has to be followed [7, 8].

The circuits are produced on top of a brass plate (75 x 55 x 1 mm^3), which is carefully sanded down with small grain sandpaper (Struers, waterproof Silicon Carbide paper, P#1000), and subsequently immersed in a 50% nitric acid solution in MilliQ water for several seconds. After rinsing it with ultrapure MilliQ water and blow drying it with pure nitrogen, a deposition reaction is done by immersion of the substrate in an $AgNO_3$ solution (0.01 $mol \cdot dm^{-3}$) during 20 seconds. Then, it is rinsed and blow dried again. In this step, the brass plate surface is covered by a black rough layer of metallic Ag, coming from the SGDR reaction (Spontaneous Galvanic Displacement Reaction) [9],

$$Cu + 2Ag^{+} \longrightarrow Cu^{2+} + 2Ag$$

Once the substrate is covered with an Ag layer, a positive photoresist AZ1512 HS is spread onto it by spin-coating (Spin coater, Laurell Technologies Corporation, WS-650MZ-23NPP/LITE), in two acceleration steps. The first is carried out at 500 rpm during 5 seconds, and the second at 4000 rpm during 30 seconds. By this procedure, the obtained photoresist layer has a thickness of 1.4 – 1.66 µm. After coating with the photoresist, a post-bake step is needed in order to attach it to the substrate and eliminate volatile components. Thus, the brass plate is heated at 95 °C during 1 minute in the hot plate.

The following step is to imprint the circuit designed on an acetate mask, on the photoresist layer by means of a 5 seconds UV light exposure (365 nm, 25 $mW \cdot cm^{-2}$), using a Mask Aligner (SÜSS Mask Aligner MJB4, SÜSS Microtec). By this method, any circuit design can be first drawn using the software Macromedia FreeHand MX, tanking into account that the desired pattern should be black in the case of a positive photoresist to protect it from irradiation, and then printed on an acetate sheet with a high resolution laser printer. After UV exposure, the brass plate is developed immersing it into a 726 MIF Developer solution (AZ Electronic Materials), during 20 seconds. When the plate is rinsed with MilliQ water and dried with pure nitrogen, one can appreciate that the entire photoresist layer has been removed, except the one

that was covered by the mask pattern and that is now drawing the circuit design on the plate.

Once the circuit shape is drawn by the photoresist, we proceed to turn the Ag free surface superhydrohobic [9]. It is done by immersing the plate into a 1 mM solution of the fluorinated thiol 3,3,4,4,5,5,6,6,7,7,8,8,9,9,10,10,10-Heptadecafluoro-1-decanethiol ($CF_3(CF_2)_7CH_2CH_2SH$, >96%, Fluka) in dichloromethane (CH_2Cl_2, ACS spectrophotometric grade >99.5%, Sigma-Aldrich), during 5 minutes. In this step, a thiol self-assembled monolayer (SAM) is formed on top of the brass plate turning its surface superhydrophobic (contact angles ≈160°).

Finally, the photoresist that is still covering part of the plate is removed by immersing it in acetone (CH_3COCH_3, 99.8%, Panreac), gently shaking during several seconds. Then, the plate is rinsed with MilliQ water and dried with pure nitrogen. We have now, on the brass plate, a hydrophilic Ag trail, surrounded by a superhydrophobic environment (Figure 6).

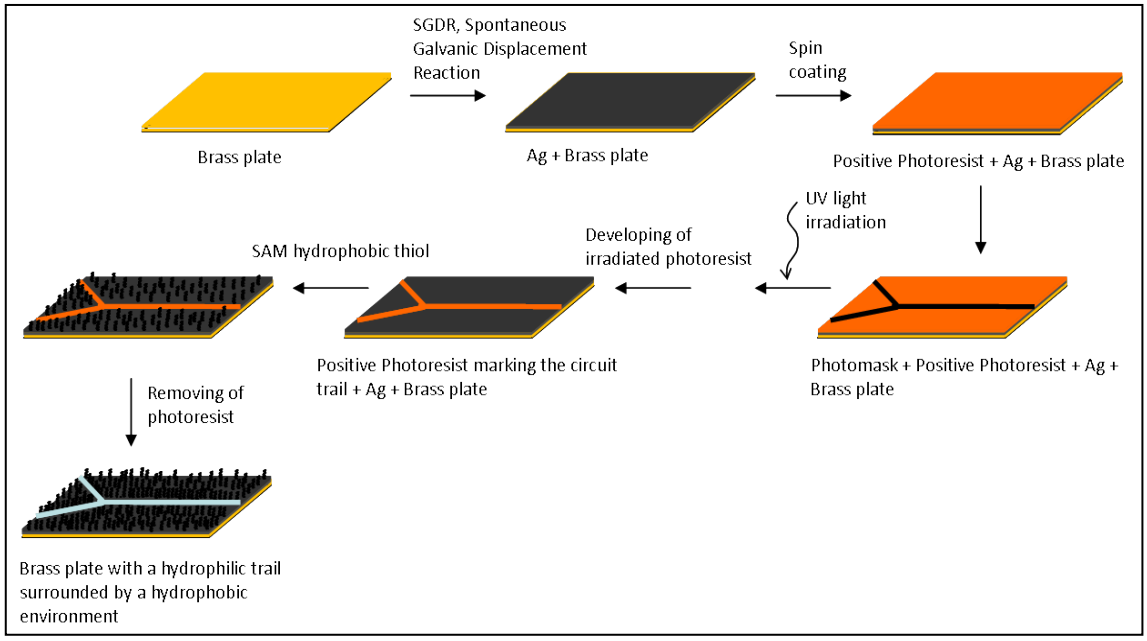

Figure 6. Schematic representation of the production of a circuit of wettability contrast.

Particle silanization

In order to be able to trace particles that are dispersed in the monolayer present at the air/water interface, and ensure they do not sink into the underlying subphase, they were treated to cover their surface with the water-soluble hydrophobic surfactant [3-(Trimethoxysilyl)propyl] octadecyldimethylammonium chloride, 72% (DMOAP, Aldrich) (Figure 5).

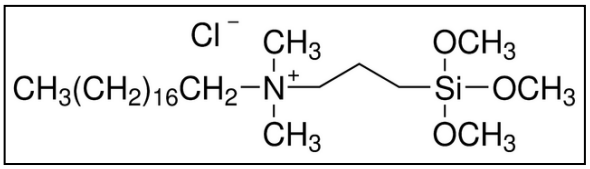

Figure 5. Chemical structure of the hydrophobic surfactant DMOAP.

The commercial silica particles used (400 nm, surface plain, Kisker), are suspended in water. As we know the exact amount of particles that are present in the suspension, we add an excess quantity of hydrophobic surfactant in order to cover their surface. Next, the suspension is heated up to 60°C, under stirring, between 3 to 3.5 hours. In this step, a surfactant layer covers the particles and a thermal treatment is done to promote the formation of a covalent bond between the silane and the silica particles [10,11]. The next step, as we will need to use the particles with solutions typically prepared with chloroform as solvent, is a solvent change. To allow the aspiration of solvent and the spare surfactant remaining in it, the particle suspension is centrifuged during 1 hour at 5000 rpm. Then, the supernatant is removed with a Pasteur pipette and 5 ml of the desired solvent are added (methanol in this case). After the addition of the new solvent, particles are re-suspended by sonication (taking great care to maintain the room temperature in the sonication bath using ice) and by means of a vortex stirrer (IKA, MS 3 Basic). In order to ensure that no water and unbound surfactant remain in the sample, the changing solvent step is repeated six times.

During all the silanization process, the test tube containing the particle suspension must be sealed with various layers of Teflon tape in order to avoid

contamination and solvent evaporation. Glass stoppers are not recommended because they could be soldered to the particle suspension container during the sonication step.

Water meniscus shape measurement by structured laser light

In section 4.3, the shape and height of the water meniscus standing above the hydrophilic channel will be needed. This was monitored by means of a structured laser light source mounted on top of the circuit placement, in order to illuminate from the top a perpendicular section of the water layer in the channel with a laser stipe. Frontal images of this section were obtained with a camera placed at a certain angle, due to the experimental impossibility to place it at an observation angle equal to 0°. Further calculations were made to obtain the real observation angle (θ = 36.59°), in order to correct the height measurements derived from the images (Figure 7)[12].

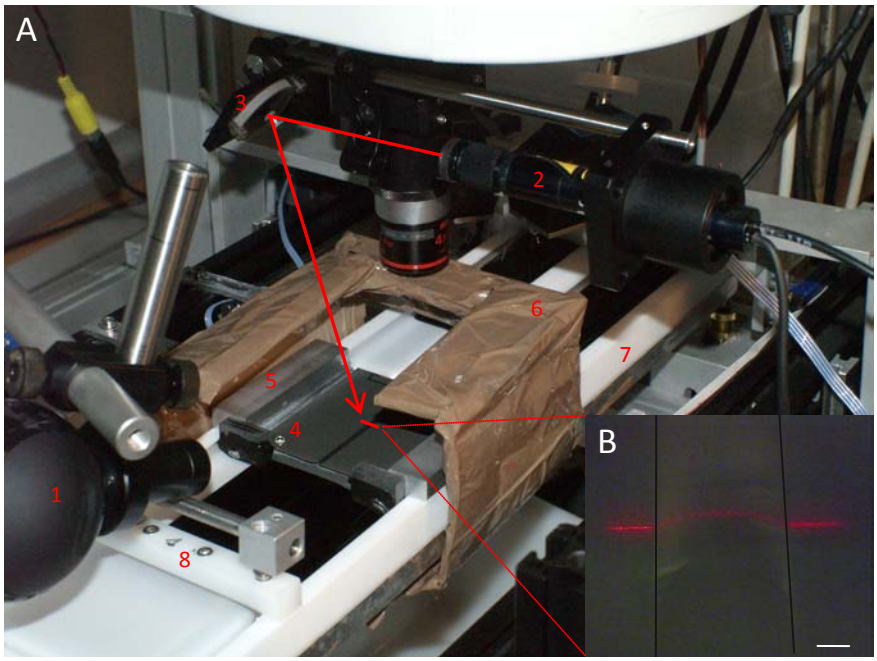

Figure 7. (A) Experimental setup for the perfilometry measurement of the cross section profile of the water meniscus. (1) Frontal camera, (2) structured laser light source, (3) mirror, (4) wettabilitty contrast circuit, (5) aluminium support for the wettability contrast circuit, (6) handmade enclosure to avoid air currents during the co-flow experiments, (7) thermostatic Teflon Langmuir trough, (8) barriers. Red solid line represents the structured laser beam light. (B) Frontal image of the water layer meniscus on the circuit (without correction). Ruler in B is 0.5 mm long.

Two-dimensional mircofluidics experimental system

The experimental system used in this section is similar to the one introduced in chapter 3 (section 3.1.2.1), but a custom made Fluorescence Microscopy module was mounted on the Brewster Angle Microscope (BAM) XYZ motorized translation stage, in order to allow simultaneous visualization by BAM and FM. The module is equipped with a Nikon super high pressure mercury lamp (100 W), a Q-imaging Exi-Blue high sensitivity camera (controlled with a custom-made application in LabView), and a Nikon fluorescence filter set for specific visualisation of the Texas Red-DHPE dye (excitation filter 559 nm, emission filter 630 nm, and dicroic mirror with a reflection band from 533 to 580 nm and a transmission band from 595 to 800 nm). Apart from that, a Langmuir Teflon trough (377 x 90 x 5 mm^3) inside of which a circuit plate can be fitted in order to create three independent compartments is used. When the circuit is fitted inside the trough, the water level is carefully increased until water from the different compartments enters the circuit trail and makes the flow of monolayers laying on the water surface possible. In order to avoid unwanted monolayer leaks, hydrophilic Delrin blocs are used to seal the different compartments and block the pass of the monolayer. As three different compartments are created, three independent movable barriers are used to force the flow of the different monolayers spread on the different compartments, at different velocities ranging from 1 to 960 mm/min (Figure 8). The surface pressure in each compartment is measured using a filter paper Wilhelmy plate attached to an electrobalance (R&K, GmbH). The temperature in the subphase is controlled by circulating water from a thermostatic bath (Julabo F12 MV) through an embedded coil attached to the Teflon trough. The system is computer-controlled with a National Instruments DAQ board (NI MSeries USB 6229) and customized software designed with LabView. Digital image analysis is performed with the software ImageJ [13].

The methods to prepare the system and spread monolayers in this case are the same as those explained in chapter 3 (section 3.1.2.1). Working surface pressure and temperature are approximately 1-2 $mN \cdot m^{-1}$, and from 20 to 25 °C depending on the

experiment. All solutions (~1mM) are prepared using chloroform (Baker, p.a.) as solvent.

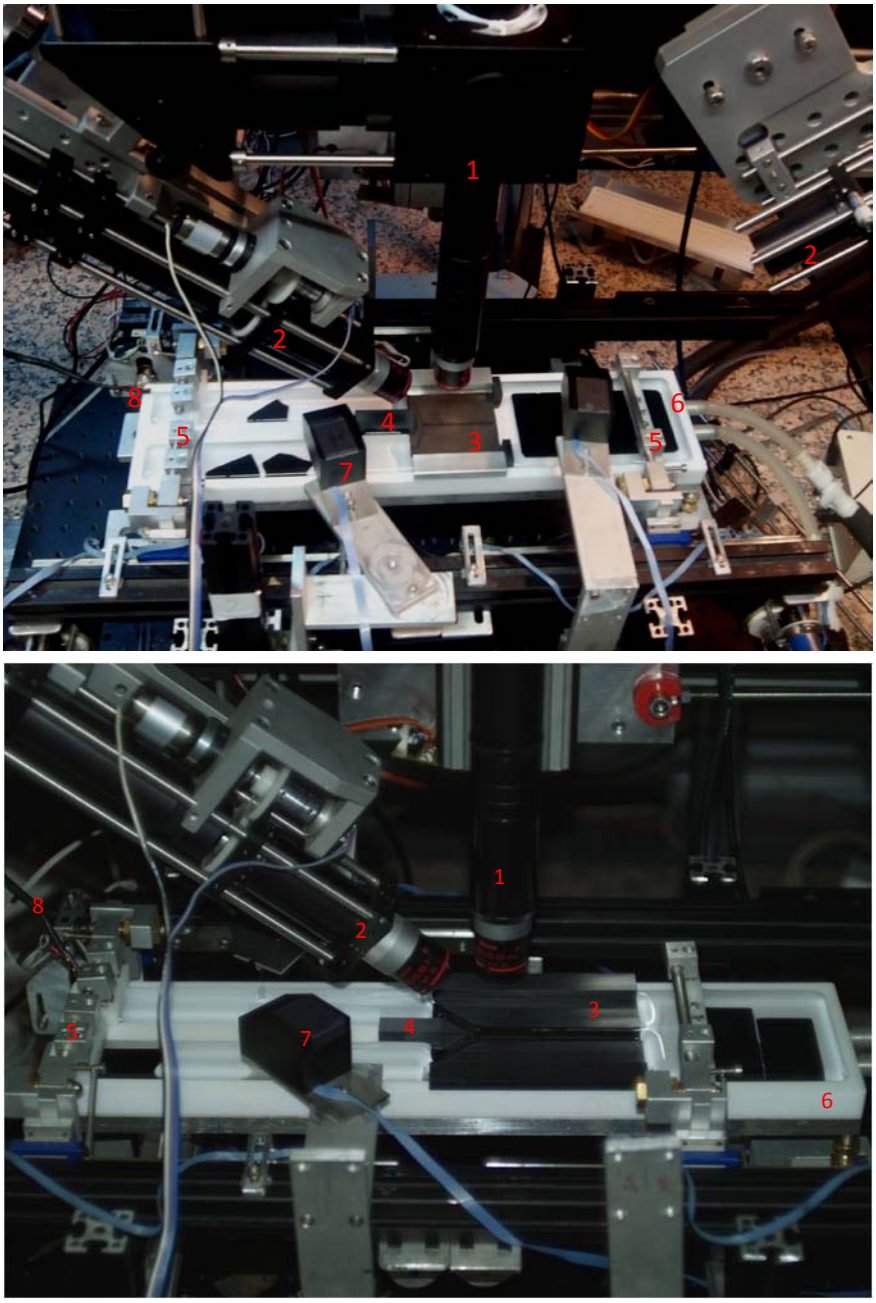

Figure 8. Experimental setup for two-dimensional microfluidics experiments. Top: setup with a wettability contrast circuited fitted in the trough. Bottom: setup with a fitted Delrin circuit, used when BAM observations are required (a wider circuit is used to have a flat surface that allows observation by BAM). (1) Fluorescence microscopy module, (2) BAM, (3) circuit, (4) Delrin block, (5) barriers, (6) thermostatic Teflon Langmuir trough, (7) filter paper Wilhelmy plate attached to a R&K electrobalance, (8) thermistor to monitor and control water subphase temperature.

4.1.3 References

[1] C. S. Gross, P. J. Simms, R. W. Towne, R. E. Miller. *Journal of Chromatography B*, **744**, 407-413 (2000).

[2] R. Wüstneck, N. Wüstneck, B. Moser, U. Pison. *Langmuir*, **18**, 1125-1130 (2002).

[3] A. Ahmad, J. B. Ghasemi. *Anal Bioanal Chem,* **387** (8), 2737–2743 (2007).

[4] http://www.lifetechnologies.com/es/en/home/brands/molecular-probes.html.

[5] K. L. Mittal, P. Kumar. *Emulsions, Foams, and Thin Films*. CRC Press, New York (2000), p. 299.

[6] Molecule synthesized by J. González, J. A. Farrera. Unpublished material.

[7] P. Burriel, J. Ignés-Mullol, J. Claret, F. Sagués. *Langmuir*, **26** (7), 4613-4615 (2010).

[8] P. Tabeling. *Introduction to microfluidics*. Oxford University Press, New York (2005), pp. 248-257.

[9] I. A. Larmour, S. E. Bell, G. C. Saunders. *Angewandte Chemie International Edition*, **46**, 1710-1712 (2007).

[10] J. A. Howarter, J. P. Youngblood. *Langmuir*, **22**, 11142-11147 (2006).

[11] F. J. Kahn. *Applied Physics Letters*, **22**, 386-388 (1973).

[12] J. M. Bennett, L. Mattsson. *Introduction to Surface Roughness and Scattering*. Optical Society of America, Washington, D. C. (1989).

[13] C. A. Schneider, W. S. Rasband, K. W. Eliceiri. *Nature methods*, **9** (7), 671-675 (2012).

SECTION 4.2

ENHANCING DIFFUSION AND MIXING IN CO-FLOWING SURFACTANT MONOLAYERS

4.2.1 Introduction

The manipulation of two-dimensional fluid flows at the submillimeter scale can afford new tools to control surface patterning for biological or chemical purposes, after transferring the resulting monolayer on an appropriate solid support [1-9]. In this context, the co-flowing of different Langmuir monolayers is a crucial step involving interfacial transport phenomena and, eventually, chemical reactions. In this last case, the achievement of good mixing conditions is essential to optimize and control the yield of any two dimensional chemical reaction [10-13].

In a previous work by *P. Burriel et al.*, a facile technique to study the coflow of independent Langmuir monolayers by confining them in circuits of wettability contrast of arbitrary shape was reported [14]. This technique enabled to mimic different strategies earlier developed in the field of microfluidics, thus it was denoted as two-dimensional microfluidics. As a first application, it was shown how such a setup enabled a direct and precise measurement of the lateral diffusion constant of a fluorescent dye in a phospholipid monolayer. Here, we have explored for ways to enhance the mixing of two coflowing monolayers by means of geometrical modifications with respect to the original straight coflow channel or by maximizing the concentration gradients across the monolayer contact line. We find that only a marginal enhancement over passive mixing can be achieved, and that more active mixing can only be achieved when the coflow takes place over deeper channels. While we focus on mixing between monolayers in the same aggregation state (expanded monolayers), we have also studied the co-flow of a condensed and an expanded monolayer, which act as the solute and the solvent, respectively, in this two-dimensional generalization of the dissolution process. In addition, we have explored

different approaches to perform a chemical reaction along the contact line between two monolayers, which are flowing through a channel.

This section begins by describing the materials and experimental methods employed in our experiments. Next, the changes in the mixing of two-coflowing monolayers compared with the baseline experiment of diffusion in a rectilinear channel of wettability contrast, when the channels are curvilinear or include constrictions and expansions, are explained. In the latter case, we find that enhanced diffusion due to the onset of vortex flow is only possible for deeper channels. The absence of vortices in flow over shallow channels correlates with the presence of anomalous velocity profiles, suggesting the presence of backflow effects due to the coupling between the monolayer and subphase flows (see section 4.3). Finally, a two-dimensional dissolution process and preliminary studies on the achievement of a chemical reaction between monolayers are shown.

4.2.2 Experimental section

For diffusion and mixing experiments, DMPC and the fluorescent probe Texas Red-DHPE were used. The diffusion of TR-DHPE into DMPC has been followed by means of epi-fluorescence microscopy (FM) using a custom build fluorescence module. Shallow channels are based on circuits of wettability contrast (see section 4.1.2) [14, 15]. For flow over deeper channels, copper plates where mechanically engraved with the desired pattern. The surrounding copper surface was rendered hydrophobic using the technique reported above. In all experiments, silica particles treated to cover their surface with the hydrophobic surfactant DMOAP where used as tracers dispersed with the spreading solution prior to monolayer preparation [16].

For dissolution experiments we worked with a lipid monolayer, MPG, which forms an hexatic phase, and a DMPC expanded monolayer. The dissolution of the hexatic phase (solid-like phase) into the expanded phase (liquid-like phase) took place during monolayer coflow through a mechanically engraved black Delrin channel. The process was monitored by Brewster Angle Microscopy (BAM) using a custom-made device. The BAM analyzer was set at 60 degrees from the incidence plane, and images

are recorded with a CCD camera (JAi, CV-M50 IR). The same experimental system was used for experiments involving the reaction between 1-octadecanethiol ($C_{18}H_{37}SH$, 98%, Aldrich) and (Cu^{2+})EDTA-C_{18} diamide [17], and between the chiral enantiomers *R* and *S*-7'Az3 [17].

4.2.3 Results and discussion

Baseline experiment: diffusion across a straight boundary

As a reference for passive mixing, the diffusion of the fluorescent probe TR-DHPE dispersed in a DMPC Langmuir monolayer (2% of TR-DHPE) is measured when such monolayer is co-flowing with a pure DMPC monolayer in rectilinear circuits of wettability contrast. Obtaining images along the channel by epi-fluorescence microscopy, we can follow the diffusion of TR-DHPE at different times of the experiment. Analyzing the obtained images by means of the software ImageJ, and assuming that the digitalized fluorescence intensity is linear in dye concentration profiles, we get the concentration profiles of the diffusive species at each position, which we fit to the Fickian diffusion equation,

$$\frac{c}{c^{O}} = \frac{1}{2} erfc\left(\frac{x - x_{O}}{2\sqrt{Dt}}\right) \Rightarrow I = I^{O} + B\ erfc\left(a\left(x - x_{O}\right)\right) \tag{1}$$

After measuring the diffusion time, *t*, at each position from the flow velocity of the monolayer at the centre of the path and the distance to the Y-junction (see Figure 1), the diffusion constant is calculated from the following relationship,

$$a^{-1} = 2\sqrt{Dt} \tag{2}$$

Diffusion constant values in the range $(8 \pm 2)\cdot 10^{-7}$ $cm^2\,s^{-1}$ have been obtained which are in good agreement with previous results.

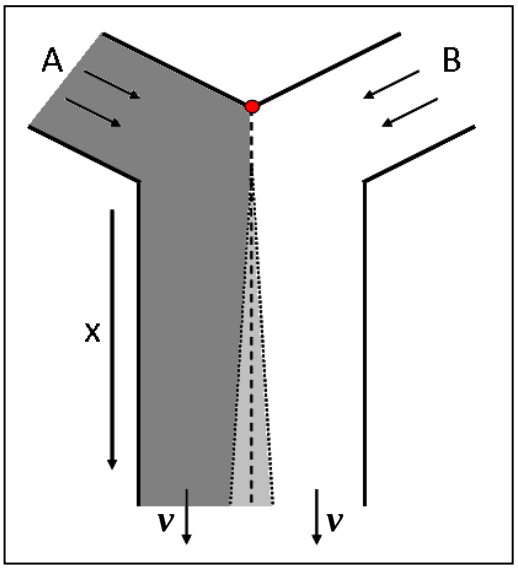

Figure 1. Schematics of the monolayer coflow system. Monolayers A and B meet at the Y-junction (marked with a red dot) that corresponds to t=0, and flow through a rectilinear path with a certain velocity v. The dashed line is depicting the interface between monolayers, and the dotted lines enclose the diffusion zone that is wider as the monolayers move forward through the cannel. The diffusion time t at different channel positions is calculated by t=x/v.

An extreme scenario for passive mixing corresponds to two miscible liquids being put into contact. We have addressed the two-dimensional equivalent of this situation by means of the co-flow of two different pure Langmuir monolayers through a rectilinear channel: DMPC and TR-DHPE monolayers, both in the LE phase. Figure 2 shows fluorescence images recorded at different positions along the channel, i.e., at different diffusion times from the contact point at the Y-junction. Contrarily to what was observed in the standard diffusion experiment above, we have found that the pure dye monolayer has a very low fluorescence, and only a thin bright stripe appears along the contact line between both monolayers. This is a consequence of the self-quenching effect for large concentrations of the fluorescence probe. This bright stripe widens as distance from the Y-junction increases, a signature of the diffusion processes occurring at the contact of the DMPC and TR-DHPE monolayers. In order to check for any enhancement in the passive diffusion with respect to the baseline experiment reported above, we had to perform an accurate calibration of the fluorescence intensity with respect to dye concentration (Fig. 2d). Having measured the calibration curve, we found that a maximum in fluorescence intensity appears at a dye concentration of approximately 10% wt., separating two differentiate branches in the

graphic corresponding to concentration values below and above the maximum. These two branches were fitted to two different polynomial functions, which were used to obtain concentration profiles from the fluorescence intensity profiles obtained experimentally, which present two differentiate zones as well, below and above the maximum. Once the concentration profiles are obtained, we followed the experimental procedure shown in the previous diffusion measurement, and we find that the process can also be described by a Fickian diffusion mechanism, leading to a diffusion constant of $(8 \pm 1)\cdot 10^{-7}$ $cm^2\ s^{-1}$. This value is consistent with the one obtained before for TR-DHPE dispersed in a DMPC monolayer. Therefore, we can conclude that diffusion is not enhanced even when the concentration gradient is extremely increased.

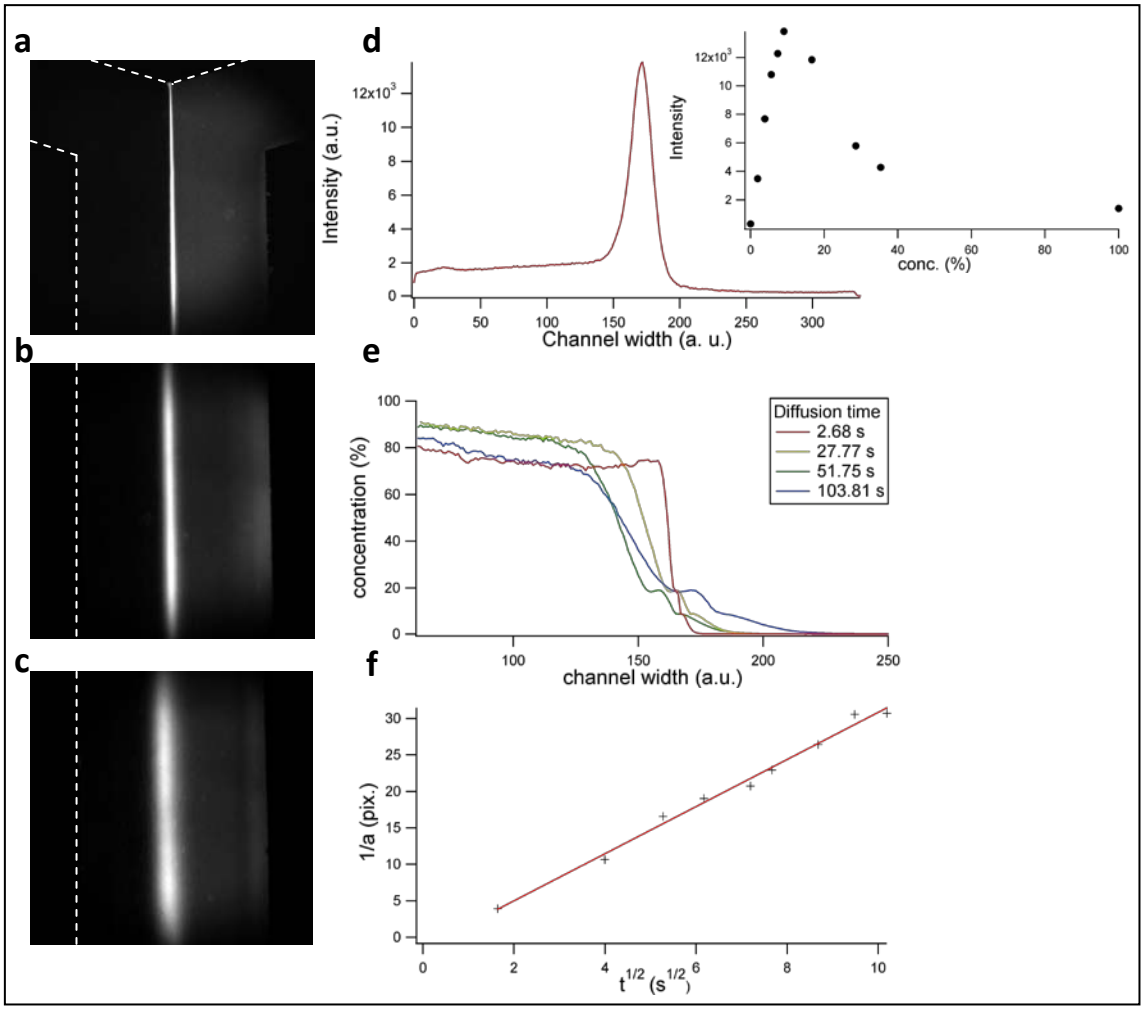

Figure 2. (a, b, c) Fluorescence microscopy images at different channel locations for a co-flow experiment. (d) Representation of the fluorescence intensity across the channel width, and the fluorescence intensity for different dye concentrations. (e) Concentration profiles across the channel width at different diffusion times. (f) Dependence of the diffusion distance a^{-1} with time.

Enhanced diffusion in curvilinear channels

It has been known for a long time that passive mixing inside droplets flowing through a microfluidic channel can be enhanced by inserting appropriate loops along the co-flow ducts [12, 13]. These geometrical features result in a phenomenon known as chaotic advection, in which secondary transversal flows distort the velocity streamlines and result in an increase in the area across which diffusion occurs. Borrowing from this idea, we have tested the effect of a looped channel on the effective mixing (diffusion) of our co-flowing monolayers (Fig. 3) [18-21].

We have prepared a serpentine channel for this experiment using the protocol described above (Fig. 3a). We have tested different designs, including round loops or straight loops with sharp corners. The results are qualitatively the same, but we have chosen the channel with semi-circular meanders, which is more amenable to further theoretical analysis. We force the co-flow of a DMPC monolayer, and a monolayer of DMPC + 2 % DHPE-Texas Red. We adjust the flow of both monolayers so that the mixing line runs along the center of the initially rectilinear part of the channel under steady-state flow conditions (Fig. 3a). In the curved part of the channel, we observe that the mixing line is displaced towards the center of curvature. This indicates that the constraint of equal flow rate is satisfied, so, as the trajectory along the curved part scales with the radius of curvature, the velocity of the monolayer in the innermost part of the curved channel is higher than the velocity of the monolayer flowing through the outer part, then, to maintain an equal flow rate, the monolayer width has to be different. The analysis of the transversal TR-DHPE concentration gradients enables to characterize the diffusion process (Fig. 3b), yielding an effective diffusion constant $D = (1.9 \pm 0.4)\cdot 10^{-7}$ $cm^2\,s^{-1}$. This value is roughly twice the one determined for diffusion of the same monolayer species along rectilinear channels. We thus conclude that the continuous compression/expansion cycles during flow along curved channels produces a detectable enhancement of passive mixing in during monolayer co-flow.

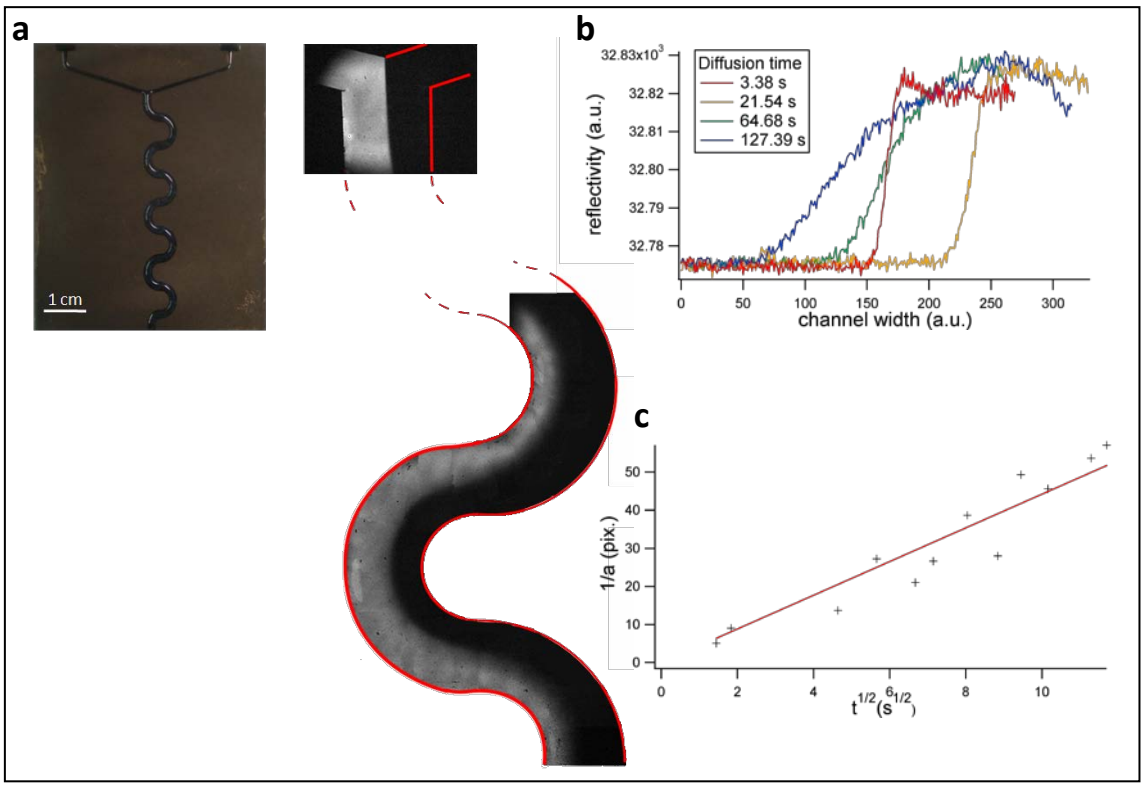

Figure 3. (a) Picture of a serpentine channel and fluorescence microscopy image of the flow through it, when the monolayer in the left is doped with a 2% of DHPE-TR. (b) Fluorescence intensity profiles across the channel at different diffusion times. (c) Representation of a^{-1} with time, which allows obtaining the diffusion coefficient (D).

Passive mixing in the presence of channel constrictions and expansions

An additional strategy to enhance diffusion during flow along micro-channels is the implementation of spatial variations in the duct shape, typically in the form of periodic modulations of the channel cross-section [12]. Even at low Reynolds numbers, this may result in the formation of fluid rolls or vortices that fold the streamlines and significantly enhance diffusive mixing [22]. In fact, the formation of surface vortices has been described by *Fuller* and co-workers in flow of Langmuir monolayers in channels with 1:4 constrictions and expansions using either hexatic or polymeric monolayers [23]. We have thus designed circuits of wettability contrast with a series of 1:4 expansions and constrictions along the channel (Fig. 4a) and have explored the possibility to distort the laminar flow of different monolayers.

We tested the system using single monolayer flow and pushing at different flow rates in order to seek the threshold for the onset of vortex creation. We have been

unable to generate surface vortices even at the highest available flow rates (1200 mm^2/s) using monolayers either in the expanded (DMPC + 2% TR-DHPE) or condensed hexatic (arachidyl alcohol, to compare with the results obtained by *Fuller et. al.*) phases. The water layer in the circuits of wettability contrast is typically 1 mm deep for channels of width 5 mm and above. In contrast, experiments by *Fuller et. al.* were performed on 3 mm deep channels, and this might suggest that the channel depth plays a crucial role in the formation of surface vortices. We have thus performed experiments using channels of two additional depths (0.5 mm, and 5.0 mm) with a single 1:4 expansion (Figure 4b, 4c). In the case of a 5.0 mm depth, the channel is machined on a copper plate that is treated to have a hydrophilic track surrounded by a hydrophobic surface. Notice that in both cases, water level will rise at least 1 mm above the flat surface. Using this configuration, we did observe the formation of surface vortices at the salient corner where the monolayer flows into the deeper expansion chamber (it is deeper because the water meniscus in it is higher), with flow of both a hexatic arachidyl alcohol monolayer and an expanded DMPC + 2% TR-DHPE monolayer. In addition, vortices could be also generated in the constriction area with the expanded monolayer (when the monolayer flows from the expansion chamber to the narrower channel). In the 0.5 mm deep channel, vortices appeared for intermediate flow rates (400 mm^2/s), and in the 5.0 mm deep channel for flow rates as low as 40 mm^2/s.

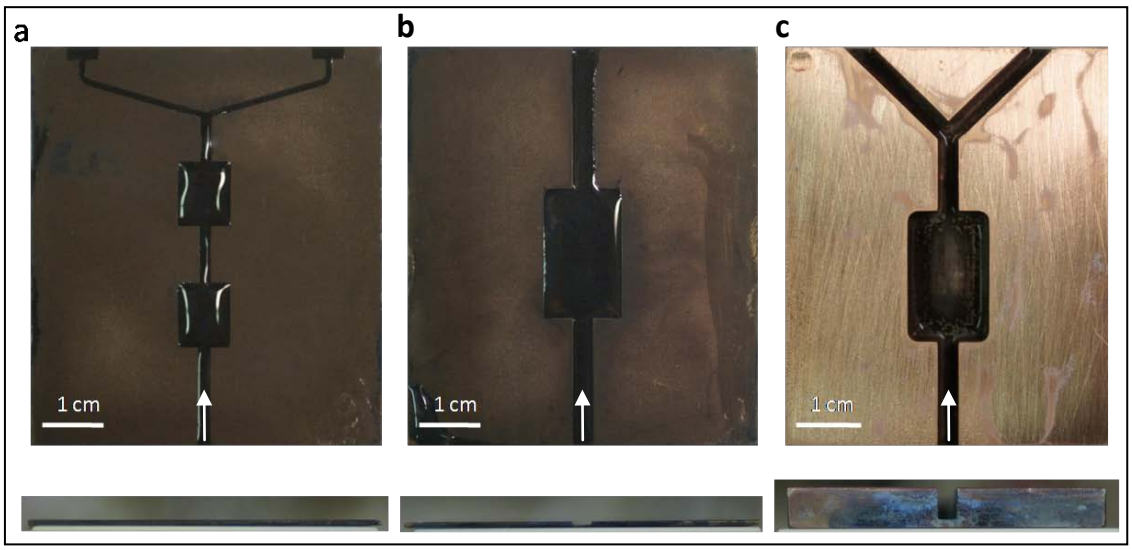

Figure 4. (a) Picture of a wettability contrast channel with 1:4 constrictions and expansions. (b) Picture of a 0.5 mm deep and (c) 5mm deep wettability contrast channel, with a single 1:4 expansion. Below each channel, a cross section picture is shown to evidence the differences in channel depth. Arrows indicate the direction of the monolayer flow.

The observed channel depth dependence in the formation of surface vortices can be correlated with an anomalous flow velocity profile across the channel observed for flow on the thin water layer present in circuits of wettability contrast. While the velocity profile across a deep channel for an expanded monolayer driven by a pressure gradient has typically a semi-elliptical profile with a maximum at the center of the channel [24], measurements in the circuits of wettability contrast reveal the existence of a depression in the velocity at the center of the channel. An explanation for the existence of this central depression is given in *section 4.3* of the present chapter, and involves the formation of a backflow in the subphase that arise as a response of the drag that the flowing monolayer is exerting on the subphase. The same backflow effects may be acting to quench the formation of surface vortices during flow past constrictions or expansions. In agreement to that, both the expected velocity profile and the formation of vortices are recovered if the water layer has an additional thickness of 0.5 mm.

Taking the above considerations into account, we prepared an experiment with a 5 mm deep channel, which had a Y-junction and a 1:4 constriction in order to make two monolayers (DMPC and DMPC+2% TR) flow together through it. When the interface between these two monolayers enters a vortex, a bigger contact area between monolayers is achieved, so diffusion will be clearly enhanced (see Figure 5).

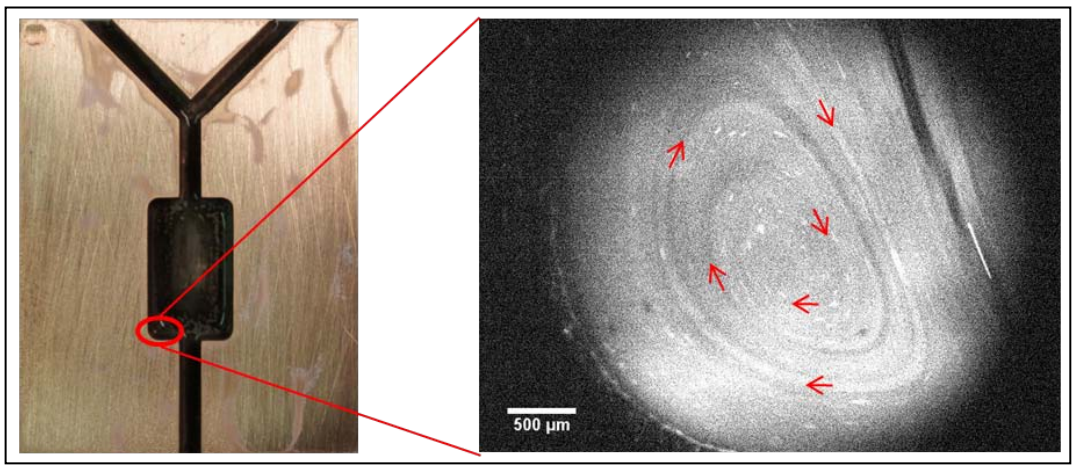

Figure 5. Y-junction channel with a 1:4 constriction through which two different monolayers co-flow. In the corners of the expansion chamber vortices are formed. To the right, a fluorescence microscopy image of the bottom-left corner shows the interface between both monolayers entering a vortex. Arrows represent the vortex flow sense.

Dissolution during the co-flow of monolayers of different phase

Until now, a transport phenomenon between two monolayers featuring the same phase, and co-flowing through a channel has been reported. In order to complement the study, a co-flow experiment between two monolayers featuring different phase states has been designed. We studied the dissolution of a hexatic phase (solid-like phase) into an expanded phase (liquid-like phase), combining Brewster angle microscopy and fluorescence microscopy observations. A lipidic MPG monolayer has been used as a hexatic phase, and a phospholipid DMPC monolayer as an expanded phase.

The experiment consists in the coflow of these two monolayers through a rectilinear path, and we have been able to observe the dissolution of the solid-like phase when it is put in contact with the liquid-like phase. We work at phase transition pressure, where the MPG monolayer is in the coexistence region between hexatic/expanded phases, forming isolated condensed domains surrounded by expanded phase. If the co-flow experiment is done in this pressure conditions, the dissolution of the condensed domains as the expanded monolayer front diffuses towards the condensed monolayer can be recorded with precision (see Figure 6). Figure 6f shows the decrease in domain area with time, which follows the three-dimensional dissolution model proposed by Brunner and Tolloczko (1900) [25], and that we have adapted to our two-dimensional dissolution situation:

$$\frac{dA}{dt} = -k' A^{\frac{1}{2}} \qquad \longrightarrow \qquad A_f = \frac{(k't)^2}{4} - k'(A_o)^{\frac{1}{2}} t + A_o \tag{3}$$

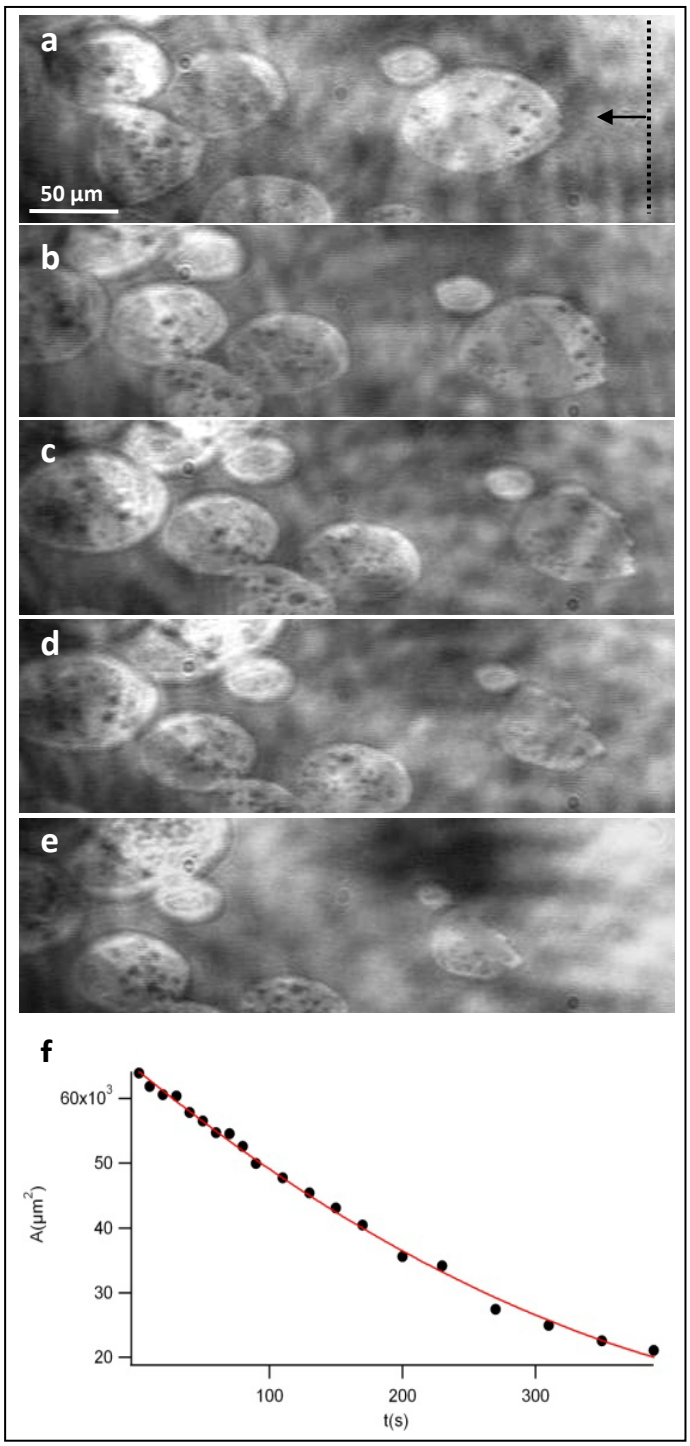

Figure 6. (a-e) BAM micrographs of the dissolution of a condensed isolated MPG domain as the expanded DMPC phase diffuses from the interface towards the MPG monolayer. A dotted line represents the interface and the arrow indicates the diffusion direction. (f) Decrease of the domain area with time and fitting to a parabolic equation (red line).

Reaction in the contact line between co-flowing monolayers

Finally, having studied the main transport phenomenon occurring at the interface between two monolayers, we have explored different systems involving

amphiphilic molecules in order to promote a reaction between two co-flowing monolayers.

The first system under consideration consists in a 1-octadecanethiol ($C_{18}H_{37}SH$, 98%, Aldrich) monolayer, and a custom synthesized (Cu^{2+})EDTA-C_{18} diamide, which has an extremely low equilibrium spreading pressure and forms tridimensional structures when spread at the air/water interface. For this reason, it is mixed with a phospholipid forming expanded phases to obtain a monolayer (10% of Cu(EDTA) in weight with respect to DMPC). When both monolayers are put into contact flowing through a rectilinear channel, a "precipitation" of the copper thiolate is expected to happen at the interface (see Figure 4 in section 4.1.1).

At this point, a substantial problem arises from the metastable nature of the thiol monolayer [26]. To avoid its collapse at low surface pressures we work at 22 °C, were the collapse occurs at 15 mN m^{-1}, and only a few three-dimensional nuclei are present in the monolayer [27]. Even in this case, when both monolayers co-flow through the channel, the friction between them is enough to cause the collapse of the thiol monolayer. This results in a bright line appearing in the interface as the monolayers flow, and avoiding the reaction between the two molecules, as they cannot diffuse through the collapsed line (Figure 7). These results haven been verified with a different thiol monolayer with the same metastable nature (1-hexadecanethiol, $C_{16}H_{33}SH$ 92%, Aldrich), and forcing a 1-octadecanethiol monolayer to flow in contact with a pure DMPC monolayer, to dismiss the hypothesis of the bright line being the solid copper thiolate precipitate. In all cases, we can see the monolayer collapse before having any evidence that the precipitation reaction is happening.

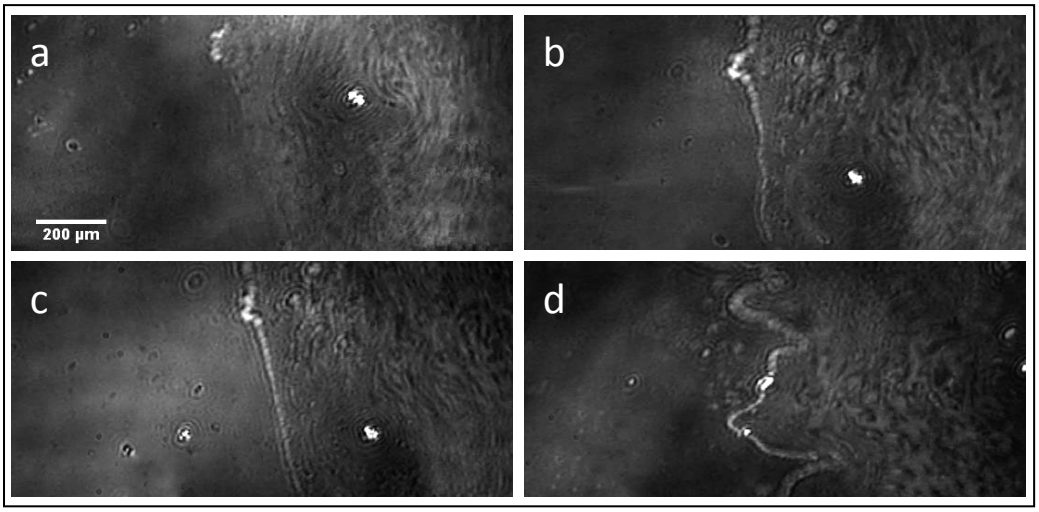

Figure 7. (a-d) BAM micrographs of the collapse of the interface with time, when a 1-octadecanethiol monolayer (monolayer at the right of the images) co-flows with a DMPC + 10% Cu(EDTA) monolayer (isotropic monolayer at the left of the images). (a) Is recorded when the two monolayers are put in contact, and (d) corresponds to an image taken 25 minutes later.

Another system under study involved monolayers of two quiral enantiomers, *R* and *S*-7'Az3 studied in chapter 3, which form isotropic monolayers when they are spread separately, but form a mesophase when a mixture of both isomers is spread. This reorganisation of molecules to form a mesophase entails recognition between the two enantiomers to form a more condensed phase. In order to visualize the formation of the mesophase in situ, two monolayers of the pure enantiomers were made to flow through a rectilinear channel. The mesophase was expected to appear in the interface between both monolayers, as the molecules diffuse towards the complementary monolayer. Unfortunately, we have not been able to monitor the formation of the mesophase, even at long experiment times (1 hour), probably due to the formation of a thin condensate line between the monolayers, product of the association of enantiomers, that would block or hinder the diffusion of molecules through the interface.

4.2.4 Conclusions

In this section, we have reported on different ways to try to enhance the transport phenomenon occurring when different two-dimensional fluids become into

contact. Based on a previous work by *Burriel et al*., where the concept of 2D-microfluidics is introduced, we attempted to enhance the diffusion between co-flowing monolayers trying different channel geometries, while controlling and maintaining adequate flow conditions. We have obtained a slight enhancement for the values of the lateral diffusion coefficient when working with curvilinear channels, and when introducing vortices in the monolayer flow, through expansions and constrictions in the channel geometry, an enhancement of diffusion can be predicted too. On the other hand, when working with two different expanded monolayers where high concentration gradients are achieved, the obtained values for the diffusion coefficient are similar to the ones obtained in the baseline experiment of diffusion in a rectilinear channel.

To complement the work, we have visualized the two-dimensional dissolution process of a condensed solid-like phase by a liquid-like expanded monolayer, in the co-flow experimental system. Moreover, we have reported on different attempts to visualize a chemical reaction in the contact line of two co-flowing monolayers, highlighting the main problem arising from the low-dimensionality of the system, the product of the reaction hinders the diffusion of the reactants and prevents the progress of the reaction.

4.2.5 References

[1] I. Czolkos, J. K. Hannestad, A. Jesorka, R. Kumar, T. Brown, B. Albisson, O. Orwar. *Nano Letters*, **9** (6), 2482-2486 (2009).

[2] D. K. Schwartz, C. M. Knobler. *Physical Review Letters*, **73** (21), 2841-2844 (1994).

[3] M. L. Kurnaz, D. K. Schwartz. *Physical Review E*, **56** (3), 3378-3384 (1997).

[4] A. Ivanova, M. L. Kurnaz, D. K. Schwartz. *Langmuir*, **15**, 4622-4624 (1999).

[5] P. Cicuta, E. M. Terentjev. *The European Physical Journal E*, **16**, 147-158 (2005).

[6] J. Ignés-Mullol, J. Claret, R. Reigada, F. Sagués. *Physics Reports*, **448**, 163-179 (2007).

[7] R. Miller, R. Wüstneck, J. Krägel G. Kretzschmar. *Colloids and Surfaces*, **111**, 75-118 (1996).

[8] H. A. Stone. *Physics of Fluids*, **7**, 2931-2937 (1995).

[9] M. Sacchetti, H. Yu, G. Zografi. *The Journal of Chemical Physics*, **99**, 563-566 (1993).

[10] G. M. Whitesides*. Nature*, **442**, 368-373 (2006).

[11] H. A. Stone, A. D. Stroock, A. Ajdari. *Annual Review of Fluid Mechanics*, **36**, 381-411 (2004).

[12] T. M. Squires. *Reviews of Modern Physics*, **77**, 977-1026 (2005).

[13] H. Song, D. L. Chen, R. F. Ismagilov. *Angewandte Chemie Int. Ed.*, **45**, 7336-7356 (2006).

[14] P. Burriel, J. Ignés-Mullol, J. Claret, F. Sagués. *Langmuir*, **26** (7), 4613-4615 (2010).

[15] I. A. Larmour, S. E. J. Bell, G. C. Saunders. *Angewandte Chemie Int. Ed*., **46**, 1710-1712 (2007).

[16] J. A. Howarter, J. P. Youngblood. *Langmuir*, **22**, 11142-11147 (2006).

[17] Both compounds were custom synthesized by colleagues from the Organic Chemistry department (*Departament de Química Orgànica, UB)*, as a result from different collaborations. (Cu^{2+})EDTA-C_{18} diamide was synthesized by *J. Gonzalez* and *J. A. Farrera,* and *R*/*S*-7'Az3 by *J. Garcia-Amorós.*

[18] S. A. Berger, L. Talbot. *Annual Review of Fluid Mechanics*, **15** (1), 461-512 (1983).

[19] J. Eustice. *Proceedings of the Royal Society A*, **85**, 119-131 (1911).

[20] J. Thomson, W. Thomson. *Proceedings of the Royal Society A*, 5-8 (1876).

[21] D. J. McConalogue, R. S. Srivastava. *Proceedings of the Royal Society A,* **307**, 37-53 (1968).

[22] R. Muruganathan, Y. Zhang, T. M. Fischer. *Journal of the American Chemical Society*, **128**, 3474-3475 (2006).

[23] D. J. Olson, G. G. Fuller. *Journal of Non-Newtonian Fluid Mechanics*, **89**, 187-207 (2000).

[24] P. Burriel, J. Claret, J. Ignés-Mullol, F. Sagués. *Physical Review Letters*, **100**, 134503 (2008).

[25] A. Dokoumetzidis, P. Macheras. *International Journal of Pharmaceutics*, **321**, 1-11 (2006).

[26] M. Broniatowski. *Journal of Colloid and Interface Science*, **337**, 183-190 (2009).

[27] P. Burriel, J. Claret, J. Ignés-Mullol, F. Sagués. *European Physical Journal- Special Topics*, **143**, 165-170 (2007).

SECTION 4.3

MEASUREMENT OF STRUCTURED BACKFLOW IN AN OPEN MICROCHANNEL INDUCED BY SURFACE TENSION GRADIENTS

4.3.1 Introduction

Flow control in microfluidic systems has been the subject of intense research in recent years, owing to the potential widespread applicability of miniaturized flow systems in material science, chemistry, and biomedicine [1–5]. Typical experimental arrangements involve narrow pipes carrying fluids into a mixing region where the relevant physicochemical processes take place. Recently, the prospect of designing open-channel alternatives has been explored [6–9] in order to address some of the drawbacks of the standard methods, such as increasing flow resistance and clogging of narrow pipes. Under the confined, low dimensionality conditions of open channel microfluidics, flow control might be exerted through interfacial processes arising at the open interface. For instance, the induction of surface vortex flow through local heating of a phospholipid monolayer could be employed to promote mixing in the underlying subphase, given the coupling between surface and bulk flow [10].

The analysis of laterally bound surfactant monolayer flow along microchannels driven by surface tension gradients has been performed in detail [11,12]. A Poiseuille like behavior is often observed in monolayers, and the coupling between monolayer and subphase flow determines whether the velocity profile is elliptic or parabolic, depending on the monolayer to subphase viscosity ratio [11]. On the other hand, anomalous flow profiles are reported in the case of viscoelastic surfactant phases [13–16]. In all the performed studies, subphase velocity is simply assumed to decay towards a nonslip condition at the flat bottom of the channel, without much regard to the precise bulk hydrodynamics. Because of mass conservation, continuous monolayer drag should result in a hydrostatic pressure buildup in the subphase downstream,

which in turn should trigger a restoring backflow [17]. This process, which might significantly alter the transport patterns in microchannels, both on the monolayer and in the subphase, has been traditionally overlooked in the monolayer flow literature.

In this section, experiments of flow in open microchannels driven by surface tension gradients at an air-water interface decorated with surfactant monolayers are reported. We demonstrate that drag at the interface and lateral confinement determine the formation of backflow patterns that carry the aqueous subphase upstream through self-organized microducts bound by velocity stagnation surfaces. We report surface and bulk particle image velocimetry measurements that, combined with a simple model, allow us to relate the interfacial flow profiles with the shape and location of the stagnation surface. We demonstrate that the observed backflow patterns depend on channel geometry, which can be tuned by adjusting the water level in microfluidic circuits of wettability contrast. The robustness of the reported phenomena is illustrated in a coflow system built on serpentine microchannels.

4.3.2 Experimental section

We control the flow of Langmuir monolayers of DMPC across a channel that connects two Teflon troughs of dimensions 25 x 125 x 3 mm^3 (upstream compartment) and 75 x 125 x 3 mm^3 (downstream compartment), respectively, in a computer controlled, custom-made assembly [6]. Spring-loaded Delrin barriers are moved independently on both sides of the channel in order to set the surface pressure gradients that drive the interfacial flow. The channels are imprinted on a 1.0 mm thick brass plate as circuits of wettability contrast as described in section 4.1.2 [19]. For deeper channels, a groove of known cross section is machined on the brass plate prior to the chemical processing. The shape of the water meniscus standing above the hydrophilic channel is monitored by means of structured laser light (see section 4.1.2). For surface velocimetry measurements, the monolayer is doped by 2% w/w of the fluorescent dye Texas-Red DHPE and 400 nm silica nanoparticles are dispersed along with the surfactant after being made hydrophobic through self-assembly coating with DMOAP. For bulk velocimetry measurements, 3 μm fluorescent hydrophilic

polystyrene particles (micromer red-F-COOH, Micromod GmbH) are added to the subphase during monolayer flow experiments.

4.3.3 Results and discussion

We have studied the monolayer velocity profiles under three different straight channel geometries with a width ranging between 1.6 and 2.0 mm (see Figure 1) and a length of 62 mm. For grooved channels, the maximum depth is 0.5 mm both for round and for rectangular grooves. In the latter case, the monolayer velocity adopts an elliptic profile (see Figure 1(a)), as expected when subphase drag determines flow resistance. This is true regardless of the height of the water meniscus above the level defined by the surrounding hydrophobic surface. On the other hand, velocity profiles over smooth tracks of wettability contrast reveal an anomalous profile, characterized by a local minimum of the velocity at the center of the channel surrounded by two symmetric maxima (see Figure 1(b)). Similar profiles are obtained regardless of the height of the water meniscus, which can be tuned in the range of 0.15 to 0.24 mm by adjusting the height of the water level in the troughs in contact with the channel plate. The same anomalous profiles can be obtained for the case of a groove with a curved cross section and a flat water meniscus (see Figure 1(c)). Increasing the water level results in this case in a progressive change towards the elliptic flow profile.

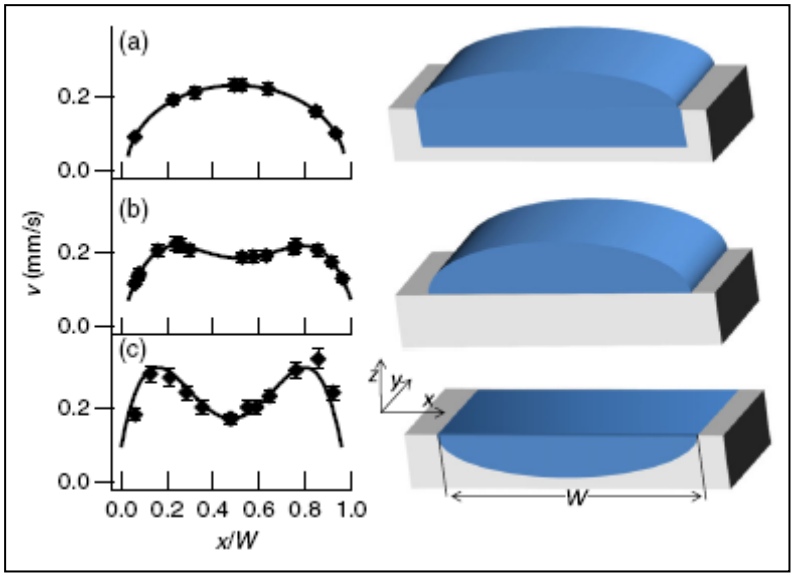

Figure 1. Measured velocity profiles across the channel for three different subphase geometries in flow of DMPC monolayers driven by surface pressure gradients (a)–(c). Subphase cross section is shown to the right of each velocity profile. In all cases, water is laterally bound by a superhydrophobic surface. An elliptic flow profile fits the data in (a). Anomalous flow profiles are obtained for geometries (b) and (c). A fourth degree polynomial fit is performed on these data as a guide to the eye and to assist in the analysis of the model detailed in the text.

In all cases, viscous drag with the moving monolayer results in the downstream transport of the subphase, building up a hydrostatic pressure gradient that generates a restoring backflow [17]. We have visualized backflow profiles by dispersing fluorescent hydrophilic microparticles in the subphase. Bulk flow follows the monolayer velocity at the interface, and is damped deeper in the subphase, until a stagnation point (zero velocity) is attained. At higher depths, tracer microparticles move upstream. Although we cannot precisely resolve the vertical location of the particles or the stagnation points, we have obtained a semiquantitative assessment of the backflow distribution by measuring at different positions across the channel the maximum upstream velocity of tracer particles (see Figure 2). In order to estimate the dispersion of these data, we have assumed a smooth upstream velocity profile and included a shaded region in each plot with the 99% confidence interval for the data points. We observe that backflow distribution is correlated with the interfacial flow. Indeed, the former spans almost evenly across the full width of the channel for configurations with an elliptic velocity profile (see Figure 2(a)) while it is confined inside a backflow band for anomalous velocity profiles (see Figures 2(b) and 2(c)). In fact, these bands are bound between the points at which the interfacial flow features the two local maxima (see Figure 1).

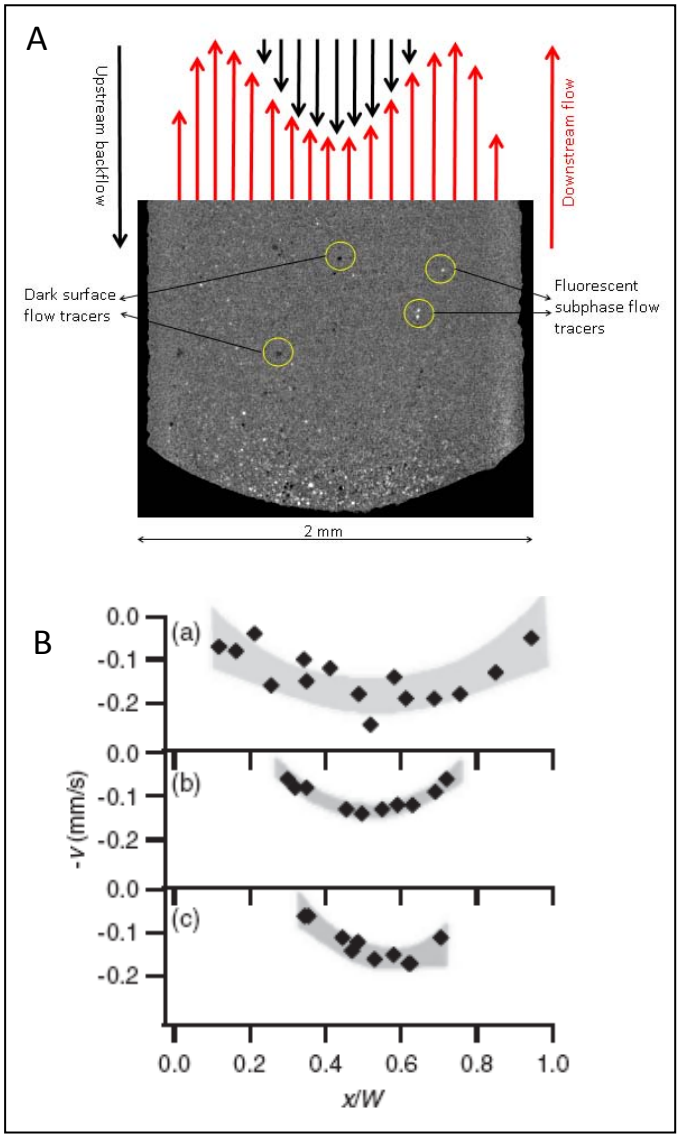

Figure 2. A) Simultaneous surface flow and backflow are visualized by means of dark surface tracers and fluorescent particle tracers, during an experiment B) Measured maximum subphase backflow velocity as a function of the relative position across the channels for the same channel geometries reported in Figs. 1(a)–1(c), respectively. Shaded regions correspond to the 99% confidence bands of the fit to a second degree polynomial.

The spatial backflow confinement can be qualitatively understood by considering that the subphase upstream flow, which in the steady state should compensate downstream transport caused by drag with the monolayer, follows the path of least resistance. For rectangular grooves and high water level (0.24 mm), the deepest region in the channel centre (0.75 mm) is just 50% deeper than the shallowest regions at the channel edges (0.5 mm). In this case, the backflow band spreads almost evenly across the channel width (see Figure 2(a)). On the other hand, for flow over circuits of wettability contrast (see Figure 1(b)) and over curved grooves with low water levels (see Figure 1(c)), the depth is almost zero at the channel edges, so

subphase backflow resistance will be significantly diminished in the central region, resulting in the self-organized confinement of the backflow.

The observed correlation between interfacial velocity profiles and backflow patterns can be employed to estimate the actual geometry of the backflow duct for a given velocity profile. The monolayer velocity across the channel (*X* direction) due to a surface pressure gradient along the channel (*Y* direction) satisfies the equation [11]

$$\mu_m \frac{d^2 v_m}{dx^2} = \mu \frac{\partial v}{\partial z}\Big|_{z=0} + \frac{d\Pi}{dy}, \tag{1}$$

where v_m is the monolayer velocity, v is the bulk velocity, Π is the surface pressure, μ = 1 cP is the viscosity of the aqueous subphase, and $\mu_m \approx 10^{-10} - 10^{-8}$ kg/s is the shear viscosity of our phospholipid monolayers in the expanded phase [12]. In the thin sublayer limit (channel width larger than subphase depth), the subphase velocity profile can be approximated by a simple shear flow, $\partial v/\partial z\big|_{z=0} \approx v_m/H$, where *H* is the subphase depth [11]. Here, we will regard *H* as the vertical distance between the interface and the nearest point of zero-velocity in the subphase underneath, so that we will be able to estimate *H(x)* using Eq. (1) after measuring the flow profile across the channel, namely,

$$H(x) = \frac{\mu v_m(x)}{\mu_m \frac{d^2 v_m}{dx^2} - \frac{d\Pi}{dy}} \tag{2}$$

We have computed *H(x)* for the experimentally measured interfacial velocity profiles, $v_m(x)$ under different channel geometries (see Figure 1) and we have obtained the corresponding loci of stagnation by subtracting *H(x)* to the cross section profile of the water meniscus, obtained from perfilometry measurements. In Eq. (2), *H(x)* is very sensitive to the value of $d\Pi/dy$, which is too small to be determined with precision using typical surface pressure probes. For this reason, we have resorted to estimating this value so that the computed locus of stagnation has a width consistent with the backflow velocimetry measurements (see Figure 2). This way, the fitted surface

pressure gradients are 1.3 mN/m^2 for flow over a smooth substrate, and 0.66 mN/m*2* for the curved channel profile (see Figures 3(b) and 3(c), respectively). These values correspond to a pressure drop of 0.1 and 0.04 mN/m along the respective channels, comparable to the 0.1 mN/m resolution of the surface pressure probe, which prevents a precise direct measurement of the surface pressure drop along the channels. For the rectangular channel profile, the backflow extends across the full width of the channel, which results in an estimation for $d\Pi/dy$ in the range of 0.4–1.6 mN/m^2.

In the cases corresponding to the anomalous monolayer velocity profiles, our calculations indicate that backflow is conducted through an immaterial duct, bound by the stagnation region above and by the channel bottom below. Notice that the distance between the interface and the stagnation region is the lowest at the centre of the channel (see Figures 3(b) and 3(c)). As a result, the vertical gradient of the flow velocity, which partially compensates the driving surface pressure gradient (Eq. (1)) is maximum at the centre of the channel, resulting in an increased friction for monolayer flow that leads to the reported anomalous flow profiles featuring a local minimum at the centre of the channel.

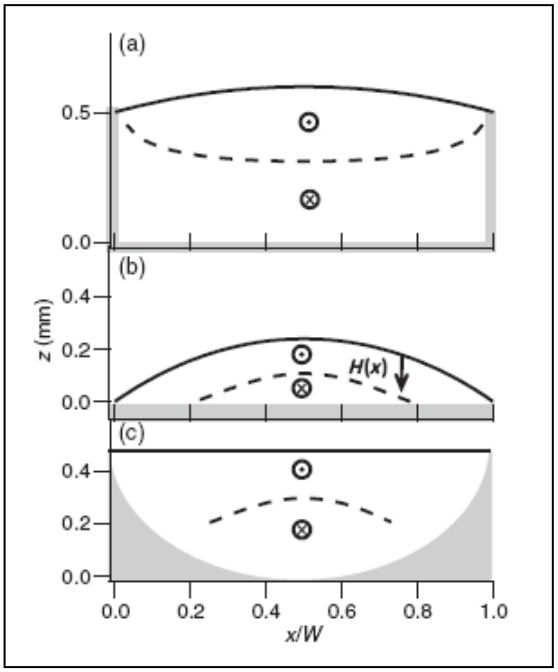

Figure 3. Cross section with the estimated loci of stagnation confining the region with subphase backflow for the different channel geometries and measured interfacial velocity profiles, corresponding to data in Figs. 1(a)–1(c), respectively, and calculated with Eq. (2). In these diagrams, donwstream flow is pointing towards the reader. Solid lines represent the position of the interface while dashed lines represent the locus of stagnation points.

In order to test the robustness of the described phenomena, we have analyzed the velocity profile in the serpentine channel described in section 4.2 of the present chapter (see Figure 4). With this arrangement, both interfacial and subphase flow can be measured independently. The flow rates are equal, so the contact line between the coflowing monolayers is located at the centre of a rectilinear portion of the channel. The measured interfacial velocity profile adopts a skewed version of the anomalous profile reported above for rectilinear circuits of wettability contrast. Since interfacial flow is driven by the pressure difference between the two ends of the channel, and the trajectory along the curvilinear paths scales with the local radius of curvature, the average velocity of the outer monolayer will be smaller than that of the inner monolayer when flowing along a bend. Evidence for this is the fact that the width of the outer monolayer is higher than that of the inner one on a bend, so that the constraint of equal flow rate is satisfied. Moreover, a robust scaling of the velocity with the radius of curvature is satisfied even for the inhomogeneous flow profile present in this configuration (see the inset in Figure 4(b)). We have also measured the maximum upstream backflow velocity at different positions across the channel width (see Figure 4(c)), and we have calculated the locus of stagnation points that best match the observed backflow profile, as explained above, yielding a surface pressure gradient of 3.6 mN/m^2. The asymmetry of the velocity profile is reflected in the backflow pattern, both in the bulk velocimetry measurements and in the calculated locus of stagnation points.

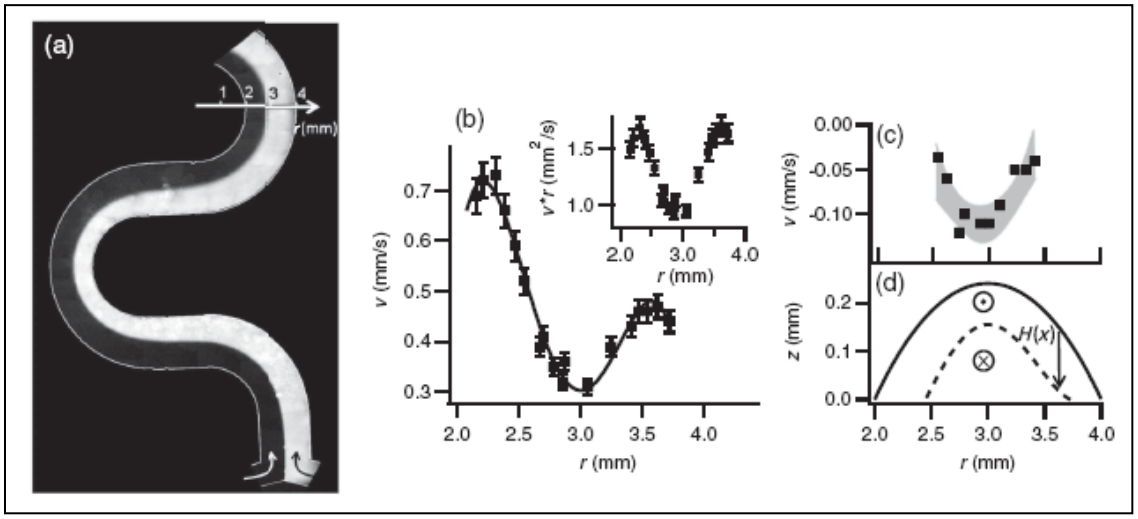

Figure 4. (a) Interfacial flow and subphase backflow profiles for two monolayers symmetrically coflowing on a serpentine circuit of wettability contrast. The water channel is 2.0 mm wide. (b) Velocity profile along the arrow segment in (a), and radial scaling (inset). (c) Measured maximum backflow velocity across the channel. (d) Calculated locus of stagnation using Eq. (2) for the flow profile in (a). The solid line represents the position of the interface while the dashed line is the locus of stagnation points.

4.3.4 Conclusions

In summary, we have reported experiments on open microfluidic systems in which the confined flow is driven by interfacial pressure gradients. The steady state in this system is the result of a feedback between interfacial and bulk flow patterns, and is characterized by anomalous interfacial flow profiles coupled with the self-organization of the subphase into an immaterial microduct that transports liquid upstream. We have provided a semiquantitative assessment of the three-dimensional flow profile, although a full solution of the hydrodynamic problem that includes the self-sustained backflow is still a pending challenge. Our findings might be employed in open channel microfluidics by dynamically adjusting the self-organized upstream duct, which would be a practical alternative to predesigned chemical channels [9]. On the other hand, tuning the flow profile obtained with a constant interfacial tension gradient by modifying the thickness of the subphase layer can be employed to control the interaction of coflowing monolayers of biomolecules.

4.3.5 References

[1] H. Song, J. D. Tice, R. F. Ismagilov. *Angewandte Chemie Int. Ed. Engl.*, **42**, 768 (2003).

[2] D. J. Beebe, G. A. Mensing, G. M.Walker. *Annual Review of Biomed. Eng*. **4**, 261 (2002).

[3] H. A. Stone, A. D. Stroock, A. Ajdari. *Annual Review of Fluid Mechanics*, **36**, 381 (2004).

[4] T. Squires, S. Quake. *Review of Modern Physics*, **77**, 977 (2005).

[5] P. Tabeling. *Introduction to Microfluidics,* (Oxford University, New York, 2005).

[6] P. Burriel, J. Claret, J. Ignés-Mullol, F. Sagués. *Physical Review Letters*, **100**, 134503 (2008).

[7] I. Czolkos, J. K. Hannestad, A. Jesorka, R. Kumar, T. Brown, B. Albinsson, O. Orwar. *Nano Letters*, **9**, 2482 (2009).

[8] R. Ledesma-Aguilar, R. Nistal, A. Hernández-Machado, I. Pagonabarraga. *Nature Materials*, **10**, 367 (2011).

[9] M. Rauscher, S. Dietrich, J. Koplik. *Physical Review Letters*, **98**, 224504 (2007).

[10] R. Muruganathan, Y. Zhang, T. M. Fischer. *Journal of the American Chemical Society*, **128**, 3474 (2006).

[11] H. A. Stone. *Physics of Fluids*, **7**, 2931 (1995).

[12] C. Barentin, C. Ybert, J.-M. Di Meglio, J.-F. Joanny. *Journal of Fluid Mechanics*, **397**, 331 (1999).

[13] M. L. Kurnaz, D. K. Schwartz. *Physical Review E*, **56**, 3378 (1997).

[14] D. J. Olson, G. G. Fuller. *Journal of Non-Newtonian Fluid Mechanics*, **89**, 187 (2000).

[15] P. Nghe, S. M. Fielding, P. Tabeling, A. Ajdari. *Physical Review Letters*, **104**, 248303 (2010).

[16] G. G. Fuller, J. Vermant. *Annual Review of Chemical Biomol. Eng.*, **3**, 519 (2012).

[17] V. G. Levich. *Physicochemical Hydrodynamics*, Prentice- Hall International Series in the Physical and Chemical Engineering Sciences (Prentice-Hall, Englewood Cliffs, NJ, 1962).

[18] P. Burriel, J. Ignés-Mullol, J. Claret, F. Sagués. *Langmuir*, **26**, 4613 (2010).

CHAPTER 5

PROTEIN-LIPID MONOLAYER INTERACTION

SECTION 5.1

EXPERIMENTAL SYSTEM

5.1.1 Langmuir monolayers and protein for insertion experiments.

In the following section, the different compounds involved in the experiments testing the interaction between Langmuir monolayers and a protein will be introduced.

Langmuir monolayers

Expanded phospholipid monolayers have been chosen to mimic the cellular membrane in which membrane proteins insert, since lipids are the major component of all cell membranes. These monolayers present an expanded phase at the working pressure and at ambient temperature, and are stable at the air/buffer interface. They are composed of DMPC, introduced in section 4.1.1, and of 1,2-dimyristoyl-sn-glycero-3-phospho-(rac-1-glycerol) (DMPG, Sigma, ≥99%, MW=688.85 g·mol^{-1}), a phospholipid with a negatively charged headgoup based on glycerol. These glycerol-based phospholipids are one of the main components of biological membranes and can be found in the pulmonary surfactant [1] (Figure 1). In experiments where the phospholipid monolayer needs to be doped to allow visualization by epi-fluorescence microscopy, the fluorescent dye Texas Red DHPE is used (see section 4.1.1).

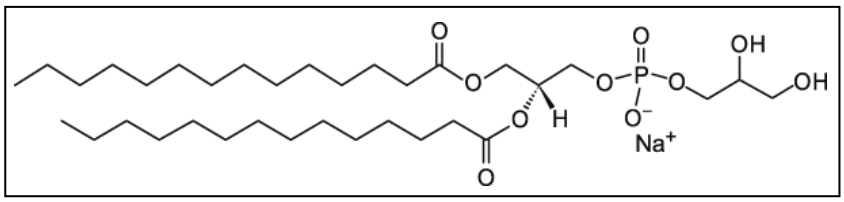

Figure 1. Molecular structure of DMPG.

The Protein

Src belongs to a family of 11 nonreceptor tyrosine kinases known as the SRC family kinases (SFKs), which regulate cell growth, differentiation and adhesion [2-9]. They are composed of the same functional domains: a myristoylated or palmitoylated N-terminus, the SH3 and SH2 regulatory domains that maintain the SFKs in an inactive state or interacting with other proteins, the kinase (catalytic domain) and C-terminal regulatory region. The largest difference between the SFK members is in the intrinsically unfolded N-terminal region, which comprises the SH4 and unique domains, called USrc. The myristoyl or palmitoyl groups located at this region allow these kinases to attach to the cellular membranes, and the charged SH4 domain contributes to the permanent anchoring of the protein to the membrane via electrostatic interactions, due to its hydrophilic positively charged aminoacids [10-12].

The protein used in our experiments is the myristoylated USrc (MyrUSrc, Figure 2A), which, compared to non-myristoylated USrc, allows studying the Unique Domain closer to the biological reality through the analysis of its insertion in phospholipid membranes. For experiments that require a fluorescent protein, a maleimide reactive fluorophore Alexa Fluor 488 (Excitation=496 nm, Emission=519 nm, Life Technologies) has been coupled to the C-terminal of MyrUSrc (Figure 2B and 2C).

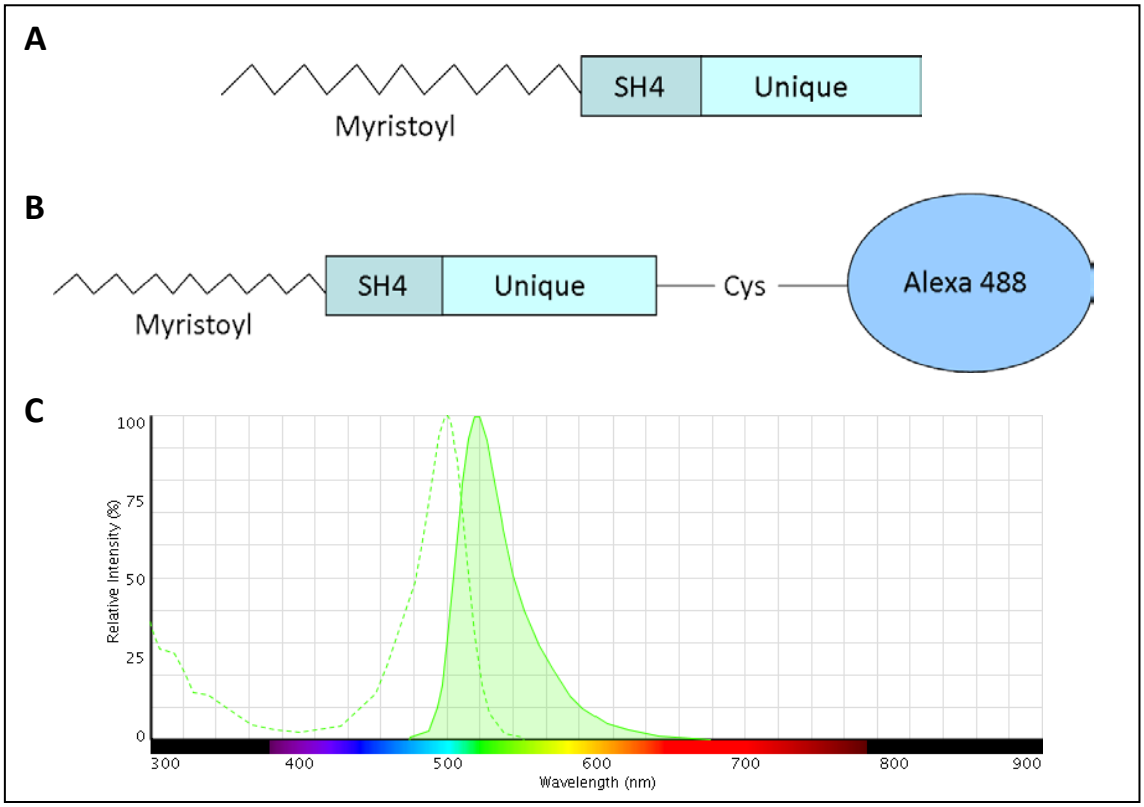

Figure 2. (A) and (B) schematic representation of myristoylated USrc, and fluorescent MyrUSrc. (C) Adsorption and emission spectra of the Alexa Fluor 488 dye. The dotted line corresponds to the excitation peak, while the peak shadowed in green corresponds to the emission [13].

5.1.2 Experimental protocols

Experimental set up for protein insertion experiments

The same experimental set up used for the microfluidics experiments in chapter 4 (section 4.1.2), has been used here. In this case in order to overcome some of the limitations of using a Langmuir trough designed for only Langmuir film experiments, a new trough was designed. It has three independent Teflon compartments (125x25, 125x25, 125x75 mm^2) which are not connected through the subphase as a difference with the previous cuvettes, avoiding possible subphase fluxes from one compartment to another. It can fit a circuit imprinted in a metallic plate to perform two-dimensional microfluidic experiments, thus connecting the three compartments only through the circuit track. The compartments are 2 mm deep, reducing substantially the volume of subphase needed, and so the amount of protein needed to ensure a determinate

concentration in the subphase buffer. One of the compartments, where the incubation of protein for its insertion in the monolayer is done, has two lateral holes with a diameter of 1 mm, to allow the entrance of a syringe needle to exchange the subphase adding a certain volume through one of the holes and removing the same amount through the other (Figure 3).

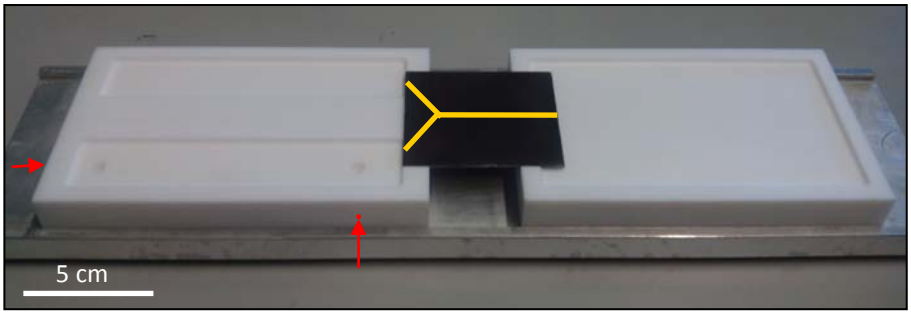

Figure 3. Photograph of the Langmuir tough used for incubation and insertion of the protein in a phospholipid monolayer. A wettability contrast circuit is fitted, connecting the three compartments and allowing two-dimensional microfluidic experiments. For the sake of clarity, the circuit track has been highlighted. Red arrows indicate the position of the lateral holes that allow subphase exchange.

Surface pressure in the compartments is measured by means of a filter paper Wilhelmy plate attached to a Kibron DeltaPi-4x balance (Kibron Inc.), controlled by the software DeltaGraph4X 1.13 (Kibron Inc.). These experiments are carried out at room temperature, and the methods to prepare the system and spread monolayers in this case are the same explained in chapter 3 (section 3.1.2.1).

Langmuir-Blodgett and Langmuir-Schaefer films

In order to transfer the monolayer with the inserted protein onto a solid support to further analyse it by Atomic force microscopy, the Langmuir-Blodgett (LB) and Langmuir-Schaefer (LS) techniques have been used. For a detailed explanation of the protocol, materials and experimental system involved in the process, see chapter 3 section 3.1.2.3 were the LB technique has been described. Langmuir-Schaefer is often seen as a variant of the LB deposition, being the horizontal deposition in LS the only difference between them (see Figure 4).

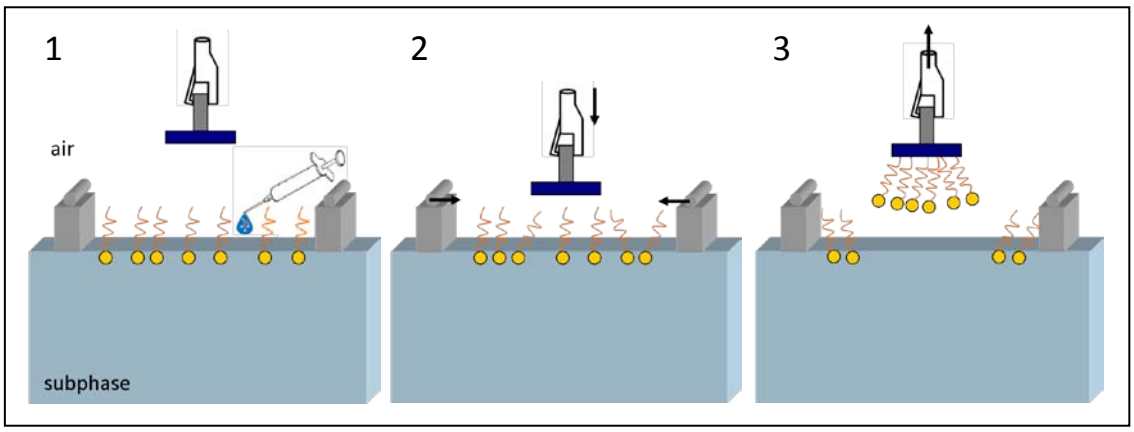

Figure 4. Schematic representation for the preparation of an LS film from a Langmuir monolayer. (1) A clean glass substrate is held with the dipper clip in a horizontal position, and the monolayer is spread on the interface. (2) The monolayer is compressed until the desired pressure, and the substrate is approached to the surface until contact is achieved. (3) While the substrate is withdrawn, the monolayer is adsorbed onto it.

DMOAP silanization of glass plates

When the LB or LS transference requires a hydrophobic substrate into which to transfer a monolayer, the following protocol has been used in order to cover the surface of the glass plate with a hydrophobic silane monolayer of DMOAP (introduced in section 4.1.2) [14]. This surface functionalisation is performed by immersing the clean glass substrate (cleaned with piranha as described in chapter 3, section 3.1.2.3) into a diluted aqueous solution of DMOAP (< 2% wt., 7 drops of DMOAP in 50 ml of water). The substrate is soaked in this solution contained in a stain trough for approximately 40 minutes. Afterwards, the glass plates are rinsed with MilliQ water and dried with pure nitrogen. In order to ensure the formation of a covalent bonding between the silane and the glass plate, the substrates are cured at 115 ˚C during 1hour 30 minutes.

5.1.3 References

[1] R. J. King, M. C. MacBeth. *Biochimica et Biophysica Acta (BBA)-Biomembranes*, **647**, 159-168 (1981).

[2] M. Donepudi, M. D. Resh. *Cellular Signaling*, **20**, 1359-1367 (2008).

[3] S. M. Thomas, J. S. Brugge. *Annu. Rev. Cell. Dev. Biol.*, **13**, 513-609 (1997).

[4] G. S. Martin. *Nat. Rev. Mol. Cell. Biol*., **2** (6), 467-475 (2001).

[5] B. Sen, F. M. Johnson. *Journal of Signal and Transduction*, Review Article (2011).

[6] Y. Pérez, M. Gairí, M.Pons, P. Bernadó. *J. Mol. Biol.*, **391**, 136-148 (2009).

[7] M. T. Brown, J. A. Cooper. *Biochimica et Biophysica Acta*, **1287**, 121-149 (1996).

[8] T. J. Yeatman. *Nat. Rev.*, **4**, 470-480 (2004).

[9] S. J. Parsons, J. T. Parsons. *Oncogene*, **23**, 7906-7909 (2004).

[10] P. Patwardhan, M. D. Resh. *Molecular and Cellular Biology*, **30** (17), 4094-4107 (2010).

[11] D. Murray, L. Hermida-Matsumoto, C. A. Buser, J. Tsang, C. T. Sigal, N. Ben-Tal, B. Honig, M. D. Resh, S. McLaughlin. *Biochemistry*, **37**, 2145-2159 (1998).

[12] Y. Pérez, M. Maffei, A. Igea, I. Amata, M. Gairí, A. R. Nebreda, P. Bernadó, M. Pons. *Scientific Reports*, **3** (1295), (2013).

[13] http://www.lifetechnologies.com/es/en/home/brands/molecular-probes.html.

[14] F. J. Kahn. *Applied Physics Letters*, **22**, 386-388 (1973).

SECTION 5.2

INTERACTION BETWEEN A DISSOLVED AMPHIPHILIC PROTEIN (MyrUSrc) AND TWO-DIMENSIONAL PHOSPHOLIPID MONOLAYERS

5.2.1 Introduction

During the last decades, biological membranes have been key objects of biophysical research [1,2]. They are important dynamic structures that not only provide structural support and protect the cell interior from the outside environment, but are also implicated in a variety of cellular processes including cell signalling and protein and lipid trafficking [3-6]. When an exogenous agent comes in contact with a living cell, it has to interact with the external biomembrane before it can reach subcellular targets [7-9], what has provided biological membranes vast attention from the scientific community, interested in gaining insight into the mechanisms of physiological activity of biomolecules acting at the cellular membrane level [10-12]. In general terms, biological membranes consist of lipid bilayers in which proteins ensure the selective transport of nutrients, waste, ions, etc. [13-15], and to better understand the various roles they play, it is important to study their major components: lipids and proteins. To do so, different membrane model systems can be applied [16-21], being the Langmuir monolayer technique a frequently applied method for mimicking cellular membranes [22-29], and useful to study biomolecule-membrane interactions [30-34], despite being limited by several instrumental features [35]. Specifically, we have used this model to study the adsorption of a protein at the phospholipid interface, a topic which is relevant from a biological and a physicochemical point of view, as well as it may have applications in the fields of bio-material implants [36, 37] and chromatographic systems [38].

In this chapter, we present a preliminary study of the interaction of MyrUSrc (see section 5.1.1) with phospholipid monolayers, where surface pressure measurements have been used to prove the adsorption of the myristoylated unique domain of Src onto DMPC and DMPG monolayers. For these experiments, we have used the product obtained from the expression of MyrUsrc by the method briefly described in section 5.2.2, where DNA is apparently copurifying with Myristoylated USrc. In addition, AFM, and Fluorescence microscopy images have been obtained. To carry out the experiments, a new Langmuir trough improving some of the typical limitations of this system such as high subphase volume consumption or possible contamination from different subphase present in adjacent compartments, had to be designed (see Figure 3, section 5.1).

This work was carried out in collaboration with the BioNMR group (Parc Científic de Barcelona), associated to the *Departament de Química Orgànica* (UB), with the objective to adapt the experimental system and protocols to be able to study whether a different affinity of MyrUSrc to a determinate phospholipid monolayer composition appears, when the monolayer composition is varied. In this regard, the monolayer coflow system presented in chapter 4 would be used to measure the diffusion of MyrUSrc inserted in a phospholipid monolayer, towards a phospholipid monolayer with a composition closer to the real biomembrane that is co-flowing through the same channel. In the next part, the main experimental results will be commented.

5.2.2 Experimental section

For protein insertion experiments, DMPC and DMPG monolayers were used. The fluorescent probe Texas Red-DHPE was used to dope the corresponding phospholipid monolayer (2% w/w of the fluorescent dye), to be able to visualize by epi-fluorescence microscopy (FM) the insertion of non fluorescent protein in the fluorescent monolayer. To obtain the different compression isotherms, the monolayers were compressed at 0.5, 2 and 6 mm min^{-1}. Glass plates were used as substrates for the transference of the monolayer onto a solid substrate and subsequent AFM analysis.

The protein used for these experiments consists in the myristoylated unique domain of Src (MyrUSrc), expressed and purified by A.-L. Le Roux (BioNMR group, Parc Científic de Barcelona), using a dual gene expression vector (pETDuet-1) carrying two cloning sites, in which N-myristoyl Transferase (NMT) and USrc are inserted. USrc and NMT are coexpressed in Rosetta cells in the presence of myristic acid, and the myristoylation of USrc is done in these conditions by NMT. Then, purification of MyrUSrc is performed via the pass through a Streptactin column due to the presence of a StrepTagII sequence at the C-terminal of the protein, eluting it with Desthibotin. Final purification is achieved using a Sepharose 75 column. To be able to visualize MyrUSrc by Fluorescence microscopy, an alternative construction was done in order to covalently couple a fluorescent dye (Alexa Fluor 488, Life Technologies) to a cysteine termination added to the protein. Further characterisation carried out after the expression of the protein (SDS-PAGE, Western Blot and light scattering) indicates the presence of the purified protein apparently forming supramolecular aggregates (several times the weight of non-myristoylated MyrUSrc), that cannot be broken in the presence of SDS. Light scattering measurements indicate polydispersity of the sample, with a mean radius value of 65 nm. An agarose gel of the protein sample reveals the presence of DNA that is copurified with MyrUSrc in the expression method, explaining the formation of supramolecular aggregates that we will refer to as *MyrUSrc containing bodies* (MCB).

The protein is obtained dissolved in a phosphate buffer solution (50 mM Na_2HPO_4/NaH_2PO_4, 0.02mM EDTA, pH≈7), and all the experiments are carried out with the same buffer solution as subphase.

5.2.3 Results and discussion

The phospholipids

As a reference, DMPC and DMPG compression isotherms on buffer have been obtained to ensure that in such conditions of ionic strength and at room temperature, the monolayers remain in a non-structured expanded phase, and no phase transition appears in the explored range of surface pressures (Figure 1).

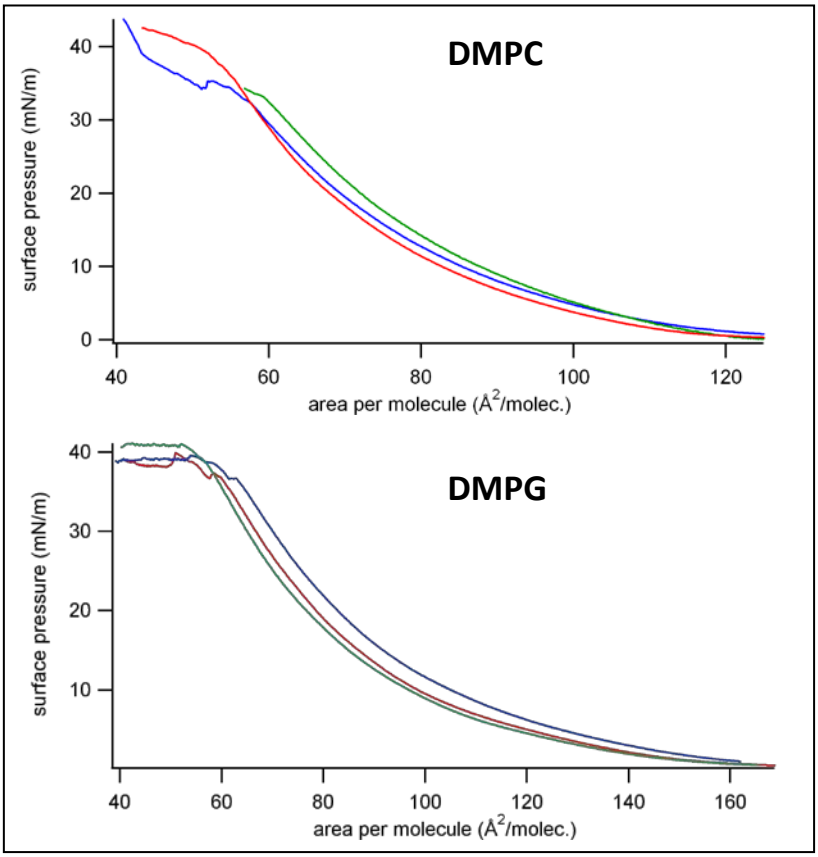

Figure 1. DMPC and DMPG compression isotherms on the phosphate buffer subphase. Each graph shows three different experiments. Collapse of the monolayer occurs at a surface pressure close to 40 mN/m.

MyrUSrc

In order to study the surface activity of the protein on the phosphate buffer solution-air interface, a surface pressure vs. time curve (π - t) was measured (Figure 2). The Langmuir trough is filled with buffer solution and the surface pressure is adjusted to zero. Then, the subphase is simultaneously removed and replaced by the same amount of a 1 µM protein solution in buffer. At this point, the surface pressure is allowed to stabilize and, with time, a gradual increase in its value is observed ($\Delta\pi \approx 10$ mN m^{-1} after approximately 3.5 hours), indicating a slow adsorption of the protein on the interface. In order to test the stability of the protein adsorbed at the interface, the same exchange method is used to extract the protein from the subphase. To ensure that no protein remains after the exchange, the process is repeated three times creating three spikes in the $\pi - t$ curve, considered as artefacts due to changes in the subphase volume during the exchange process. After this step, the surface pressure

remains constant, a signature of a stable protein monolayer adsorbed at the interface, with a non-significant loss of matter going to the subphase.

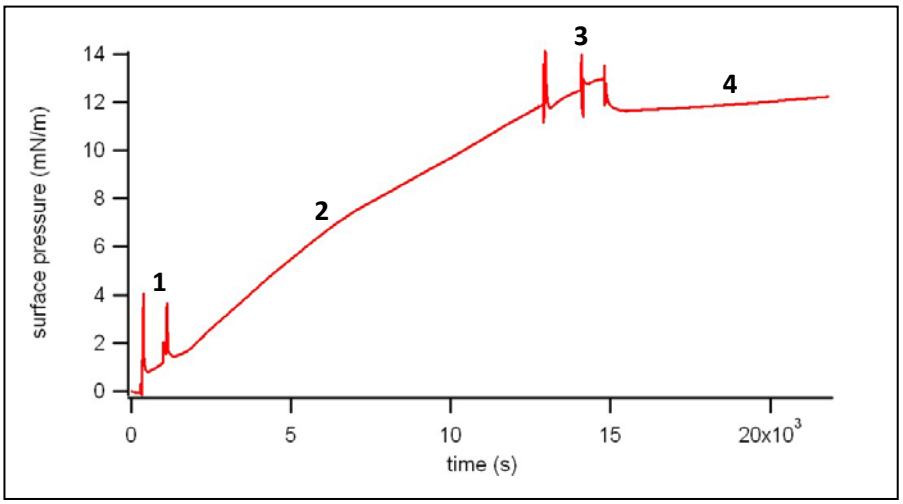

Figure 2. π – t curve of protein adsorption at a bulk protein concentration of 1μM. (1) Peaks in surface pressure created during the exchange of subphase to introduce the protein in the system. (2) Protein incubation (protein is adsorbing at the interface). (3) Artifacts in surface pressure during the exchange of the subphase to extract the protein. (4) Surface pressure is considered to remain constant, since the slight increase observed here can be attributed to a subphase evaporation.

In general, all experiments in the present chapter involving the addition of a protein solution in the subphase have been carried out taking care to have a final protein concentration in the Langmuir trough of 1 μM. This value was chosen through a $\pi - c$ isotherm to be the optimal to have a substantial surface pressure increase, using the minimum amount of protein. In Figure 3, an increase of π with protein concentration in the subphase, tending to a limiting value between 20-25 mN m^{-1} at c > 1 μM, can be observed. At 1 μM, the surface pressure is within 50% of the saturation value.

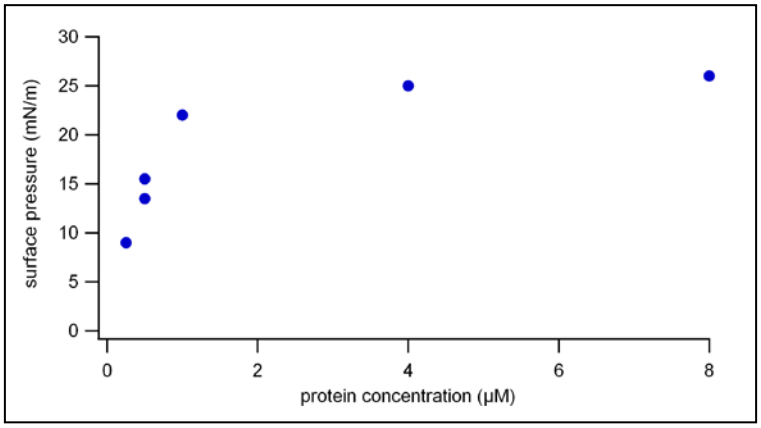

Figure 3. $\pi - c$ Gibbs adsorption isotherm of the protein at the buffer subphase (protein activity). Data supplied by the BioNMR group, Parc Científic de Barcelona.

Since the protein can be adsorbed in the air-buffer interface, and it is not substantially desorbing and diluting into the subphase, compression isotherms were recorded (Figure 4). In this case, in order to accelerate the adsorption step, the protein was deposited directly on the air-buffer interface spreading droplets of protein solution with a micro-syringe, and waiting until the surface pressure remained at a constant value. Then, successive expansion-compression cycles were performed, stopping the barriers movement at different points of the cycle, and at different barrier velocities. A significant hysteresis can be observed, and the compression-expansion paths overlap after several cycles, as well as at different barrier velocities. The effect of stopping the barrier motion depends on the surface pressure value, π, at which barriers are stopped. When the barrier movement is stopped at low π values, surface pressure increases, but if the movement is stopped during the compression step, the surface pressure change is minor and becomes negative at large enough π values, so the monolayer relaxes to lower surface pressures. During the expansion step, an increase in π when the movement is stopped is usually observed. This behaviour could be explained considering the tendency of the protein to form aggregates in the buffer solution, which would presumably be adsorbed on the aqueous buffer surface, giving rise to a Gibbs-like monolayer. During compression of these adsorbed aggregates, when barriers are stopped and the surface pressure value is low, they are probably reorganizing into a more expanded configuration causing an increase in surface pressure. When barriers are stopped at higher surface pressure values, the

tendency of these aggregates seems to be to reorganise into a less area demanding configuration, causing a relaxation in the surface pressure of the system.

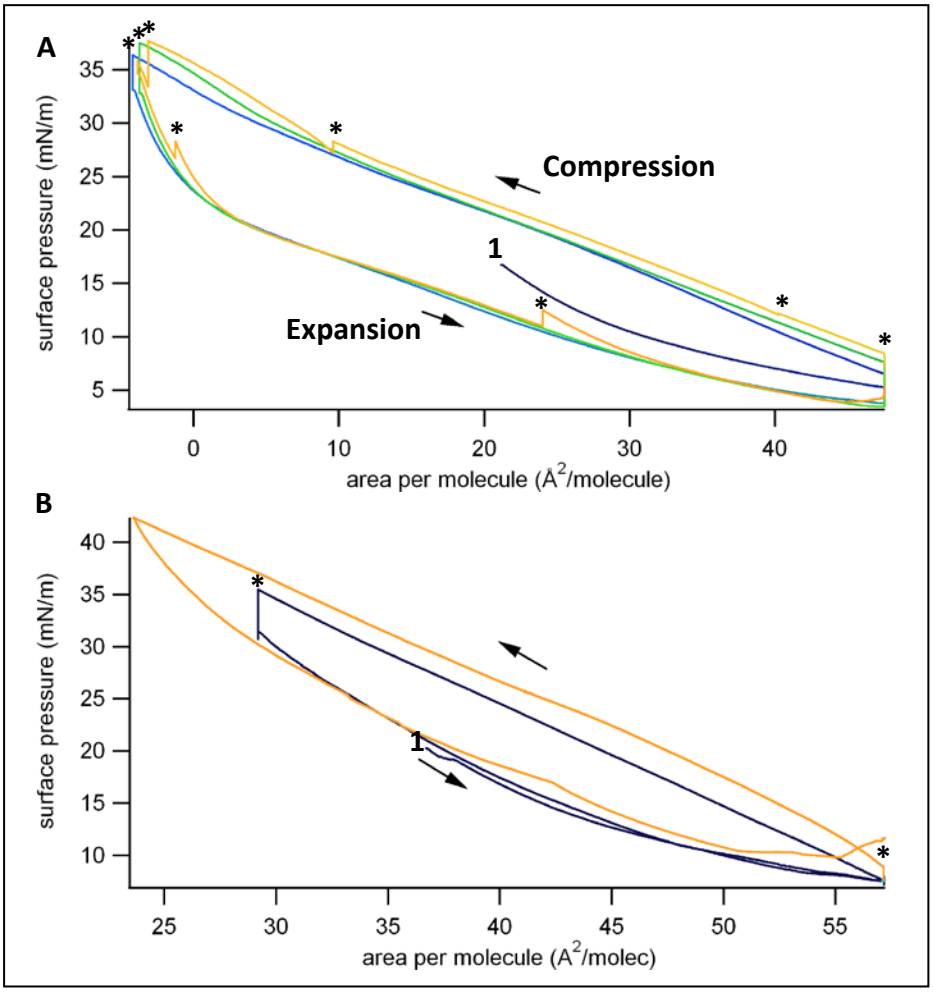

Figure 4. Compression isotherms of the protein monolayer at the phosphate buffer/air interface. The different colours correspond to different compression-expansion cycles of the same monolayer. In both graphs (1) indicates the beginning of the cycle, and (*) indicates when the barrier motion is stopped. (A) All compression-expansion cycles are carried out at a barrier velocity of 6 mm min^{-1}. (B) The blue cycle is carried out at a barrier velocity of 2 mm min^{-1}, and the orange cycle at 0.5 mm min^{-1}.

In order to investigate the morphology of the protein monolayer, it has been transferred onto a solid support by means of the Langmuir-Blodgett technique, and observed by Atomic Force microscopy. The substrate used in this case is a clean glass plate (10 x 25 mm^2). The main characteristic of the obtained images is the presence of a granular structure formed by spherical entities with a diameter close to 250-300 nm and a height of (60-70 nm), which confirms the hypothesis of the MCBs present in the buffer solution being adsorbed on the interface (Figure 5). These aggregates are

transferred to the solid support without an important perturbation of their structural characteristics, and their size is comparable to the value obtained by light scattering measurements. AFM analysis of the aggregates gives bigger values for their diameter, but smaller values for their height, which could be explained taking into account that their transference from an aqueous solution to a solid support and being observed in an air environment could result in a "flattening" of the aggregates losing their spherical shape.

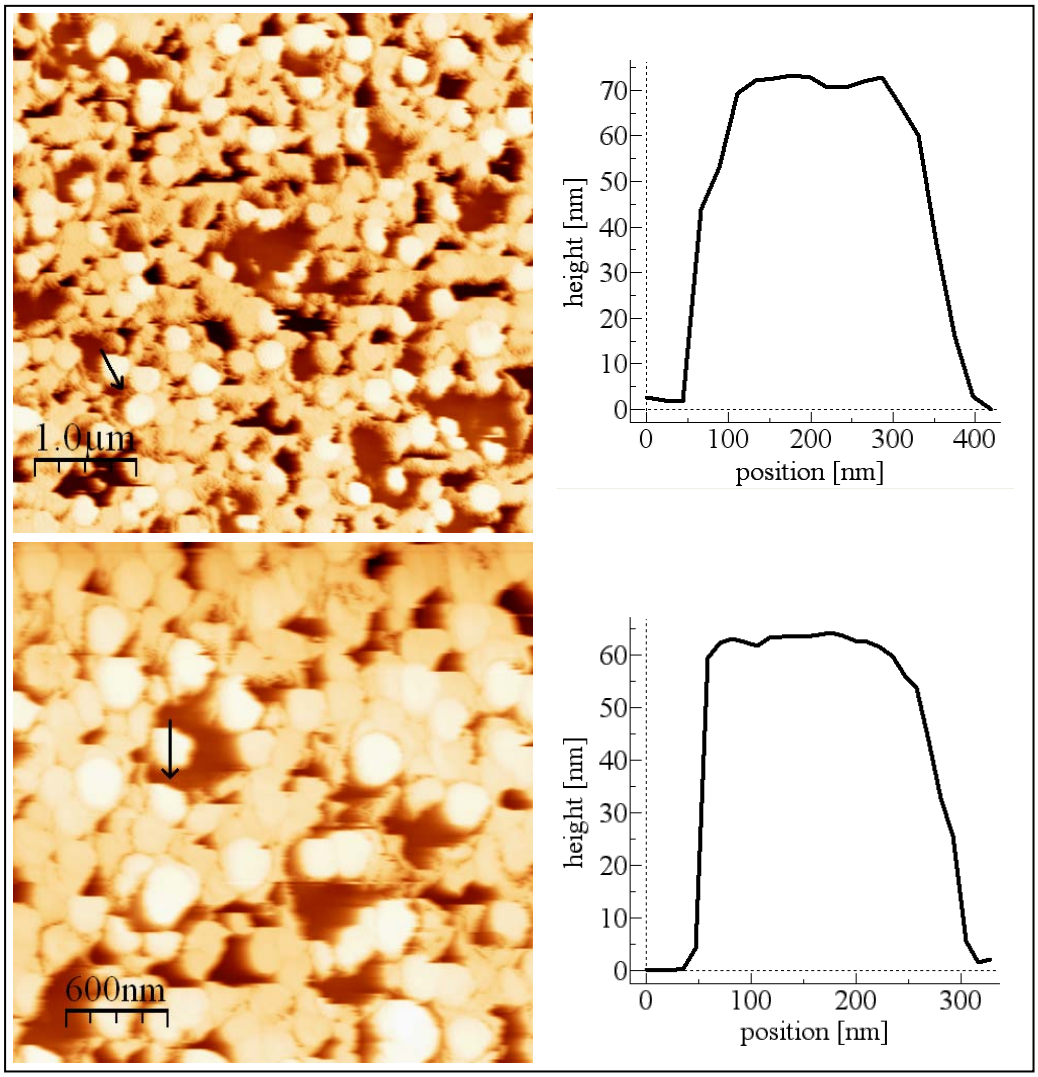

Figure 5. AFM images of a transferred protein monolayer on a clean glass substrate, at π= 20 mN m^{-1} and room temperature. The height profile along a linear path, marked by an arrow on the AFM image, is included to the right of the image.

Interaction of MyrUSrc with phospholipid monolayers

In this part of the chapter, the adsorption of the protein on a phospholipid monolayer will be discussed. The phospholipid monolayer used to test the capability of myristoylated USrc to insert in it is spread on top of the phosphate buffer solution by the deposition of a chloroform solution of the phospholipid. The initial state of the monolayer has been chosen to be at $\pi \approx$ 7-10 mN m^{-1}, a value that allows enough surface pressure range to work before reaching $\pi \approx$ 32 mN m^{-1}. The latter corresponds to the maximum pressure value at which no protein can be inserted in the monolayer, working with a protein concentration of 1µM (see Figure 6). When the phospholipid monolayer remains at a constant pressure and enough time has been left to allow chloroform evaporation, a protein solution is injected in the subphase by means of the exchanging method described above. Protein insertion is monitored measuring the change of surface pressure with time (π-t curves, Figure 7), showing that the presence of a phospholipid monolayer at the interface concerns mainly the kinetics of the adsorption process. Thus, a $\Delta\pi \approx$ 10 mN m^{-1} is attained in this case after approximately 40 minutes of insertion time. Step 5 in Figure 7 shows that the insertion of the protein has an irreversible character since it remains adsorbed after removing the protein present in the subphase.

Moreover, the insertion kinetics of MyrUSrc and fluorescent MyrUSrc has been compared when a DMPC monolayer was spread in the interface, giving very similar trends where no significant difference can be deduced from their behaviour.

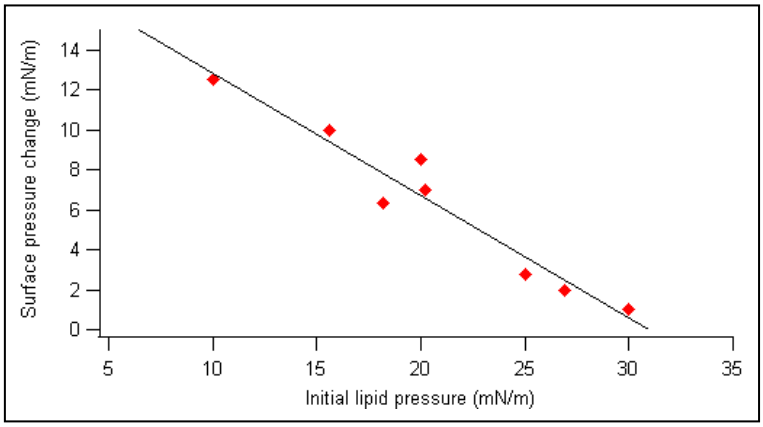

Figure 6. Surface pressure change for protein insertion experiments at different initial lipid pressures. For a $\pi \approx 32$ mN m^{-1}, no surface pressure increase is expected. Black line is a linear fit. Data supplied by the BioNMR group, Parc Científic de Barcelona.

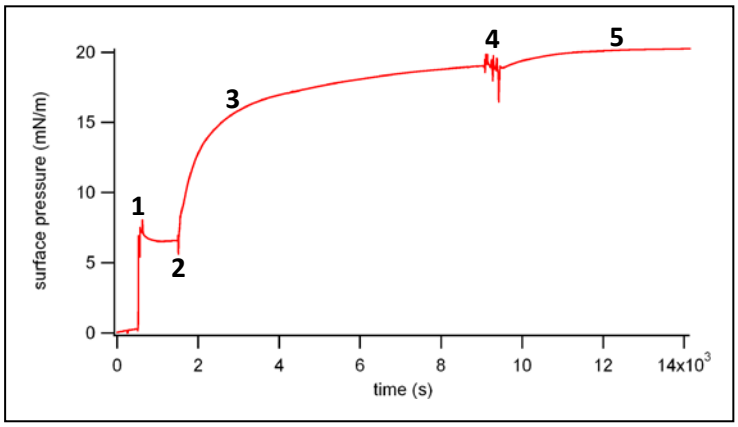

Figure 7. Example of a π-t curve of the insertion of protein in a DMPC monolayer. (1) DMPC monolayer deposition, (2) subphase exchange to introduce the protein, (3) surface pressure increase due to protein insertion, (4) subphase exchange to remove the protein from the system, (5) protein remains adsorbed after subphase cleaning.

In order to record images of the inserted protein in the DMPC monolayer, two different experimental approaches haven been done. In a first batch of experiments, the insertion of fluorescent MyrUSrc was carried out following the process described for Figure 7, and the inserted protein was visualized by means of epi-fluorescence microscopy after having removed the fluorescent protein remaining in the subphase. In a second experimental approach, the DMPC solution was doped with a 1% of the fluorescent probe Texas Red DHPE, and spread on the interface forming a fluorescent monolayer. Subsequent insertion of non fluorescent MyrUSrc creates dark spots of a few microns in size in the fluorescent monolayer, allowing to monitor it during all the insertion process by epi-fluorescence microscopy. Figure 8 shows images where fluorescent and non-fluorescent inserted MCBs can be detected, and, with time, these

aggregates grow in size and self-organize leading to threads or filaments that merge forming bundles of tenths of microns. When the experiment is carried out at an initial surface pressure of the DMPC monolayer of π = 32 mN m^{-1}, no pressure increase is observed and no protein clusters appear in the interface, meaning that the protein is not able to insert at this high surface pressures (in agreement with what is derived from Figure 6). In this case, if some of the lipids are removed from the surface (aspiration using a Pasteur pipette connected to a pump) and surface pressure is decreased until π = 12 mN m^{-1}, the appearance of aggregates can be followed with time.

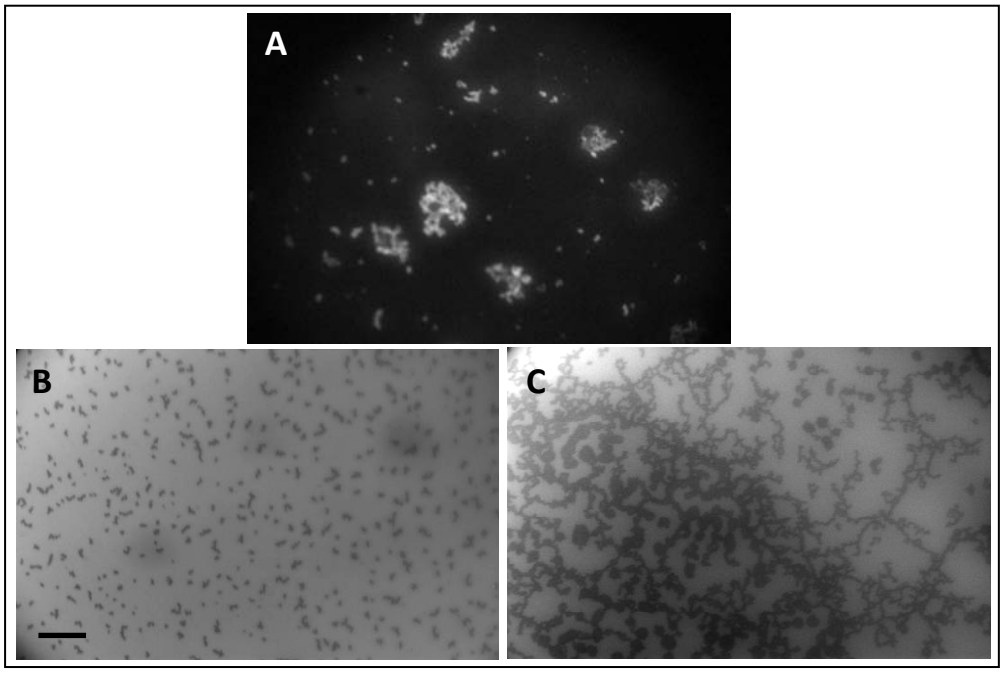

Figure 8. Epi-fluorescence microscopy image of a DMPC monolayer with inserted fluorescent MCBs (A), and a fluorescent DMPC monolayer with inserted non-fluorescent MCBs after 1 hour and 3 hours of insertion time (B and C respectively). Scale bar is 50µm.

The fact that the protein is aggregated in the bulk and in the interface, creates a different situation from what is expected to happen when working with a pure protein solution. In this scenario, the protein insertion could happen homogeneously, allowing the measurement of protein diffusion coefficients through analysis of fluorescence intensity profiles, as shown in chapter 4.

To complement the study, compression isotherms ($\pi - A_m$) of the phospholipid monolayer with the inserted MCBs are recorded (Figure 9). The system has been

prepared spreading a DMPC monlayer and the protein has been injected following the subphase exchange method explained above. After the protein insertion curve has reached saturation, the subphase is cleaned through the exchange method in order to remove all the remaining protein, and compression-expansion cycles are started.

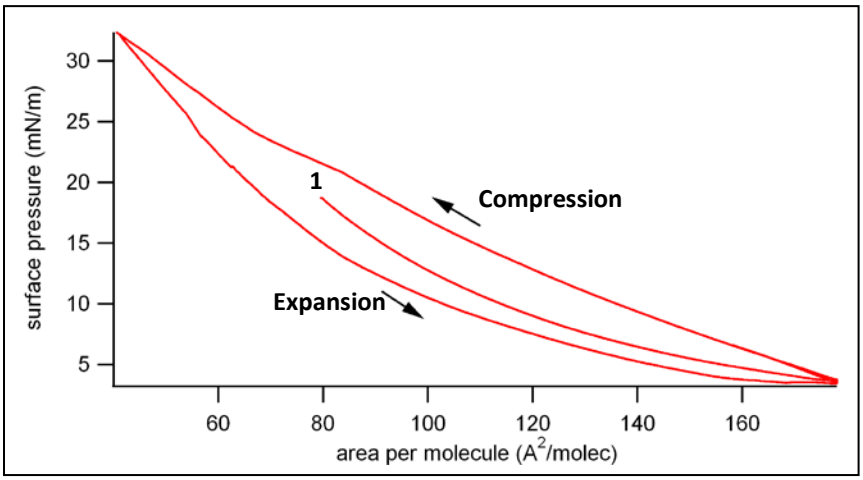

Figure 9. Compression isotherms of a DMPC+MCB monolayer at the phosphate buffer/air interface. (1) Indicates the beginning of the cycle.

To image the morphology of MCB-DMPC monolayer, it has been transferred onto a hydrophobic glass treated with DMOAP, by the Langmuir-Schaefer technique, and spherical entities have also been observed in this case (Figure 10).

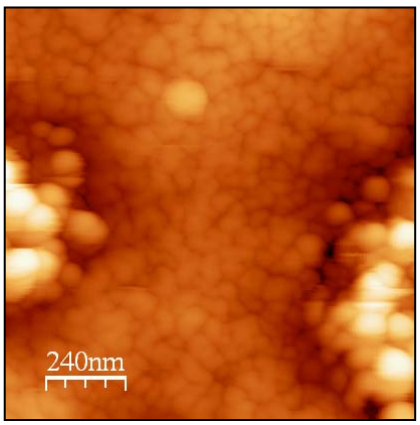

Figure 10. AFM image of a DMPC+MCB Langmuir-Schaefer film. The substrate is a glass plate with a hydrophobic surface treatment (DMOAP self-assembled monolayer).

Apart from exploring the effect of having a fluorescent label on the protein, the difference in the insertion kinetics depending on the nature of the phospholipid monolayer has been tested, comparing the insertion of the MCBs in a DMPC and in a DMPG monolayer. In Figure 11, one can clearly observe the faster kinetics of the insertion process as well as a greater $\Delta\pi$ when a negatively charged DMPG monolayer is present in the surface. For this reason, a mixed phospholipid monolayer with a composition of, for example, DMPC/DMPG 2:1, may be used in future experiments.

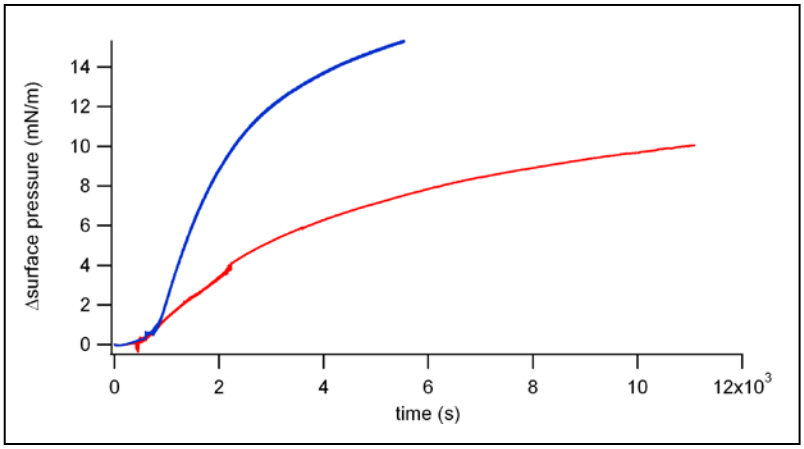

Figure 11. Comparison of the protein insertion in a DMPC (red line) and in a DMPG monolayer (blue line).

5.2.4 Conclusions

We have adapted the two-dimensional microfluidics experimental system and protocols to study the interaction of MyrUSrc with phospholipid membranes. This will enable to explore its affinity to different phospholipid compositions through the measurement of its diffusion coefficient during the diffusion from one monolayer to another.

The product of the myristoylation of USrc in vivo has been found to aggregate in bulk and at the interface. The present work is a preliminary study of the surfactant character of the *MyrUSrc containing bodies* (MCB), in the presence and absence of a phospholipid monolayer at the air-buffer interface. In addition, we report on AFM and epi-Fluorescence microscopy images that show the appearance of such aggregates.

Further experiments are needed to fully characterize the used proteins and to optimize the expression and purification methods to obtain pure MyrUSrc.

5.2.5 References

[1] S. Morandat, S. Azouzi, E. Beauvais, A. Mastouri, K. El Kirat. *Anal. Bioanal. Chem.*, **405**, 1445-1461 (2013).

[2] L. A. Bagatolli, J. H. Ipsen, A. C. Simonsen, O. G. Mouristen. *Prog. Lipid Res.*, **49**, 378-389 (2010).

[3] S. Nathoo, J. K. Litzenberger, D. C. Bay, R. J. Turner, E. J. Prenner. *Chemistry and Physics of Lipids*, **167-168**, 33-42 (2013).

[4] Z. T. Schug, C. Frezza, L. C. A. Galbraith, E. Gottlieb. *Acta Oncologica*, **51**, 301-310 (2012).

[5] C. Dietrich, L. A. Bagatolli, Z. N. Volovyk, N. L. Thompson, M. Levi, K. Jacobsen, E. Graton. *Biophysical Journal*, **80**, 1417-1428 (2001).

[6] K. Simons, E. Ikonen. *Nature*, **387**, 569-572 (1997).

[7] L. J. Johnston. *Langmuir*, **23**, 5886-5895 (2007).

[8] E. I. Goksu, J. M. Vanegas, C. D. Blanchette, W. C. Lin, M. L. Longo. *Biochimica et Biophysica Acta*, **1788**, 254-266 (2009).

[9] K. El Kirat, S. Morandat, Y. F. Dufrene. *Biochimica et Biophysica Acta*, **1798**, 750-765 (2010).

[10] A. Wnetrazk, K. Latka, P. Dynarowicz-Latka. *J. Membrane Biol.*, **246**, 453-466 (2013).

[11] B. Gzyl-Malcher, J. Handzlik, E. Klekowska. *Colloids and Surfaces B: Biointerfaces*, **112**, 171-176 (2013).

[12] S. Kundu, H. Matsouka, H. Seto. *Colloids and Surfaces B: Biointerfaces*, **93**, 215-218 (2012).

[13] H. Sprong, P. van der Sluijs, G. van Meer. *Nat. Rev. Mol. Cell. Biol*., **2**, 504 (2001).

[14] Y. W. Hsueh, M. Zukermann, J. Thewalt. *Concept. Magn. Reson. A*, **26A**, 35 (2005).

[15] D. M. Owen, K. Gaus, A. I. Magee, M. Cebecauer. *Immunology*, **131**, 1 (2010).

[16] R. Maget-Dana. *Biochimica et Biophysica Acta*, **1462**, 109-140 (1999).

[17] C. Peetla, A. Stine, L. Labhasetwar. *Mol. Pharm.*, **6**, 1264-1276 (2009).

[18] Y-HM. Chan, S. G. Boxer. *Curr. Opin. Chem. Biol.*, **11**, 581-587 (2007).

[19] D. B. Kell. *Trends Biochem. Sci.*, **6**, 8-9 (1981).

[20] A. L. Ottova, H. T. Tien. *Bioelectrochem. Bioenergy*, **42**, 141-152 (1997).

[21] R. P. Richter, R. Berat, A. R. Brisson. *Langmuir*, **22**, 3497-3505 (2006).

[22] H. Brockman. *Curr. Opin. Struct. Biol*., **9**, 438-443 (1999).

[23] K. Hac-Wydro, P. Dynarowicz-Latka. *Ann. UMCS Chem*., **63**, 47-60 (2008).

[24] H. L. Brockman. *Chemistry and Physics of Lipids*, **73**, 57-79 (1994).

[25] B. Gzyl, M. Paluch. *Progr. Colloid Polym. Sci.*, **118**, 22 (2001).

[26] B. Gzyl, M. Paluch. *Appl. Surf. Sci*., **246**, 357 (2005).

[27] F. He, Y. Lin, R. Li, G. Tang, D. Wu. *Colloids Surf. B*., **87**, 164 (2011).

[28] L. Lin, A. Liu, Y. Guo. *J. Phys Chem. C*., **116**, 14863 (2012).

[29] B. Juskowiak, A. Swiatkowska. *Colloids Surf. A*., **417**, 250 (2013).

[30] G. A. Borioli, B. L. Caputto, B. Maggio. *Biochemical and Biophysical Research Communications*, **280**, 9-13 (2001).

[31] H. Lavoie, B. Desbat, D. Vaknin, C. Salesse. *Biochemistry*, **41**, 13424-13434 (2002).

[32] H. Lavoie, J. Gallant, M. Grandbois, D. Blaudez, B. Desbat, F. Boucher, C. Salesse. *Materials Science and Engineering*, **10**, 147-154 (1999).

[32] D. Vollhardt, V. B. Fainerman. *Advances in Colloid and Interface Science*, **86**, 103-151 (2000).

[33] J. Rubio-Magnieto, S. V. Luis, M. Orlof, B. Korchowiec, G. Sautrey, E. Rogalska. *Colloids and Surfaces B: Biointerfaces*, **102**, 659-666 (2013).

[34] T. Keszthelyi, K. Hill, E. Kiss. *J. Phys. Chem. B*., **117**, 6969-6979 (2013).

[35] G. Chwastek, P. Schwille. *ChemPhysChem*, **14**, 1877-1881 (2013).

[36] R. E. Baier, R. C. Dutton. *J. Biomed. Mater. Res.*, **3**, 191 (1969).

[37] L. Vroman, A. J. Adams. *J. Colloid Interface Sci*., **111**, 391 (1985).

[38] F. J. DeLuccia, M. Arunyart, L. J. Cline. *Anal. Chem.*, **57**, 1564 (1985).

CONCLUSIONS

CONCLUSIONS

- Isotherms of *trans*-8Az5COOH monolayers show a greater dependence of the phase change surface pressure on temperature than the shorter homologue 8Az3COOH, allowing the thermodynamic analysis of the phase transition by means of the two-dimensional Clausius-Clapeyron equation, determining an enthalpy and entropy value for the phase change. The analysis of a mixed *cis/trans*-8Az5COOH monolayer, where labile condensed domains rich in *trans* isomer surrounded by a *cis*-rich phase are formed, suggests that the line tension existing between the two phases is much lower than in the case of the homologue azobenzene molecule 8Az3COOH.

- In the absence of a chiral influence, the isolated *trans* rich domains of a mixed *cis/trans*-8Az5COOH monolayer are achiral. However, in the presence of a small amount of the chiral azobenzene derivative 7'Az3, the orientational chirality inside the labile domains can be selected. Moreover, when the chiral influence is a vortex flow applied in the subphase, the enantiomorphic excess of domains with a particular sign is directly related to the stirring sense applied.

- Monolayers of the chiral azobenzene derivative (R/S)-7'Az3 do not form mesophases when the pure enantiomer is used. When the monolayer is prepared with the racemic mixture, a significant heterochiral recognition leading to the formation of a mesophase is observed. The hexatic nature of this mesophase is characterized by analyzing the inner textures of isolated trans-rich domains. At all compositions, monolayers above the collapse surface pressure organize into stacks of odd-numbered multilayers, forming submillimeter birefringent domains with a well-defined microstructure that has been analysed by AFM.

- In the field of 2D-microfluidics, studies of the diffusion between co-flowing monolayers have resulted in a slight increase in the diffusion coefficient value for

experiments with curvilinear channels, and when vortices are introduced in the system. In contrast, increasing the concentration gradient between co-flowing monolayers has not been succesful at producing a noticeable impact in the measured diffusion coefficient values. On the other hand, a two-dimensional dissolution process has been visualized, with a rate that follows a classic dissolution model. Any attempt to realize a chemical reaction between coflowing monolayers has been unsuccessful because the obtained condensed product hinders diffusion of reactants across the contact line.

- The flow of monolayers in open microchannels driven by surface tension gradients has been studied, determining that drag at the interface and lateral confinement result in the formation of backflow patterns that carry the subphase liquid upstream through self-organized micro-ducts. This backflow patterns depend on channel geometry and are bound by velocity stagnation surfaces, whose shape and location has been related to the interfacial velocity profiles by means of the combination of a simple model and particle image velocimetry measurements.

- The surfactant character of myristoilated protein aggregates has been tested in the presence and absence of a phospholipid monolayer at the interface, showing a tendency of the aggregates to irreversibly adsorb onto it. This work has stablished the protocols for further studies with the pure protein.

APPENDIX

SYMBOLS AND ACRONYMS

A	Molecular area
ΔS	Phase change entropy
ΔH	Phase transition heat
ε_{II}	Dielectric coefficient for light polarised parallel to the alkane chain
$\varepsilon_{\perp}$	Dielectric coefficient for light polarised perpendicular to the alkane chain
ee	Enantiomorphic excess
ee_{CW}	Enantiomorphic excess of clockwise domains
ϕ	Azimuthal angle
F_v	Vertical force
γ_0	Surface tension of the pure subpahse liquid
γ	Surface tension of the monolayer-subphase system
H	Subphase depth
I	Reflectivity function
k_v	Vertical spring constant of an AFM cantilever
λ	Wavelength
LE	Liquid expanded phase
LC	Liquid condensed phase
LB	Langmuir-Blodgett film
LS	Langmuir-Schaefer film
μ	Viscosity of the aqueous subphase
μ_m	Monolayer shear viscosity
n	Refractive index
n_T	Total number of analyzed domains
n_{CW}	Number of clockwise domains
n_{CCW}	Number of counter-clockwise domains
Ω	Stirring rate
π	Surface pressure
π_e	Equilibrium spreading pressure
π_c	Surface pressure during the phase change

R_p	Reflectivity of p-polarised light
R_S	Reflectivity of s-polarised light
S	Solid phase
θ	Tilt angle of the molecules
θ_B	Brewster angle
θ_i	Angle of incidence
θ_r	Angle of refraction
T	Temperature
t	Time
v_m	Monolayer velocity
v	Bulk velocity
8Az5COOH	4-octyl-4'-(5-carboxy-pentamethyleneoxy) azobenzene
8Az3COOH	4-[4-[(4-octylphenyl)azo]-phenoxy] butanoic acid
(*R/S*)-7'Az3	(R/S)-4-[4-[(4-(1-methylheptyloxyphenyl)azo]phenoxy] butanoic acid
AFM	Atomic force microscopy
BAM	Brewster angle microscopy
CW	Clockwise
CCW	Counter-clockwise
DMOAP	[3-(Trimethoxysilyl)propyl]octadecyldimethylammonium chloride
DMPC	1,2-dimyristoyl-sn-glycero-3-phosphocoline
DMPG	1,2-dimyristoyl-sn-glycero-3-phospho-(rac-1-glycerol)
DNA	Desoxyribonucleic acid
FM	Fluorescence microscopy
MCB	MyrUSrc containing bodies
MPG	1-monopalmitoyl-rac-glycerol
MyrUSrc	Myristoylated unique domain of the Src protein
NMT	N-myristoyl Trasferase
SAM	Self-assembled monolayer
SDS-PAGE	Sodium dodecyl sulphate polyacrylamide gel electrophoresis
SFKs	Src family kinases
SGDR	Spontaneous galvanic displacement reaction
TR-DHPE	N-(Texas Red sulfonyl)-(1,2-dihexadecanoyl-sn-glycero-3-phosphoethanolamine, triethylammonium salt)
UHV	Ultra high vacuum

UV	Ultraviolet

RESUM

1. Introducció

El termes “matèria tova” o fluids complexos engloben unA gran varietat de sistemes tal com polímers, col·loides, gels, cristalls líquids, tensioactius, micel·les i vesícules, solucions de macromolècules, etc. Tots aquest sistemes presenten característiques interessants d’estudiar no només des d’un punt de vista fonamental, sinó que també tecnològic, degut a que posseeixen aplicacions pràctiques en un ampli ventall de disciplines.

Un exemple de sistema emmarcat dins del camp d’estudi de la “matèria tova”, i en el qual es centra aquesta tesi, el constitueixen les monocapes de Langmuir. Des del 1774, quan Benjamin Franklin experimentava sobre l’efecte que tenia una pel·lícula d’oli estesa sobre la superfície de l’aigua, passant pels estudis fets per Agnes Pockels (1891) o Irving Langmuir (1917), que van desenvolupar conceptes teòrics i experimentals per tal d’entendre el comportament de molècules formant monocapes insolubles, les monocapes de Langmuir han esdevingut un sistema de gran interès degut a la seva rellevància com a sistemes model en dues dimensions. Les seves aplicacions passen per camps científics tant diversos com són la nanotecnologia, la biologia, la química o la física, i van des de l’estudi de les propietat reològiques del tensioactiu pulmonar, fins al seu ús com a sistema model de membranes biològiques o com a material estructurat per a aplicacions òptiques, electròniques o per a biosensors, un cop han estat transferides sobre un substrat sòlid mitjançant la tècnica de Langmuir-Blogett.

1.1 Monocapes de Langmuir

Determinades molècules orgàniques tenen la capacitat d’adsorbir-se i organitzar-se en les interfases gas/líquid (aire/aigua en el cas d’aquesta tesi) per tal de minimitzar la seva energia lliure, formant com a resultat pel·lícules monomoleculars

anomenades monocapes de Langmuir. Aquestes molècules són amfifíliques, és a dir, presenten dues parts amb una afinitat per l'aigua diferent: un grup funcional hidrofílic en un extrem, el *cap*, i una *cua* hidròfoba, generalment formada per una o més cadenes hidrocarbonades. Aquesta asimetria *cap-cua,* és el que les fa situar-se en la superfície de l'aigua, amb el *cap* polar submergit en la subfase i la *cua* no-polar dirigida cap a l'aire.

Per tal de caracteritzar l'estat d'una monocapa de Langmuir, s'han de tenir en compte les següents variables: la pressió superficial, π, l'àrea per molècula, *A*, i la temperatura, *T*. La pressió superficial es defineix com la caiguda de tensió superficial del líquid pur, quan una monocapa s'estén en la seva superfície, $\pi = \gamma_o - \gamma$, on γ_o és la tensió superficial del líquid pur, i γ és la tensió superficial del sistema aigua-monocapa. La tensió superficial té unitats de força per unitat de longitud, típicament [mN m^{-1}], i l'àrea per molècula es defineix com la superfície ocupada per una molècula, i habitualment té unitats de [$Å^2$ $molecula^{-1}$].

Un cop la monocapa està dipositada sobre la superfície de l'aigua, es pot caracteritzar mitjançant isotermes de compressió (pressió superficial, π, enfront de l'àrea per molècula, *A*), que es realitzen comprimint la monocapa mitjançant dues barreres mòbils a velocitat constant, i registrant els canvis de pressió produïts (Figura 1). La informació extreta d'una isoterma revela l'existència de diferents estat d'agregació, que representen diferents graus d'ordre molecular com a resultat de les interaccions entre les cadenes hidrofòbiques i entre els caps polars i la subfase.

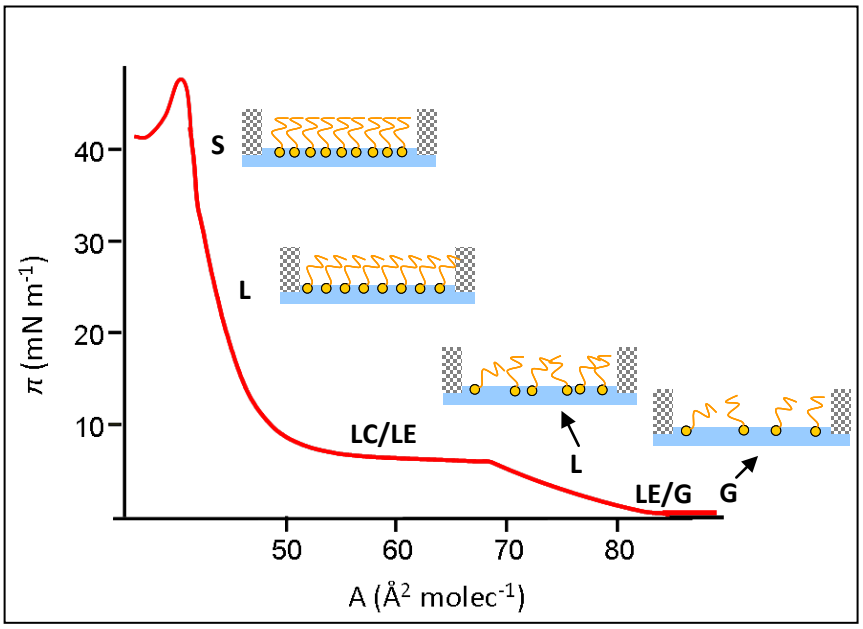

Figura 1. Isoterma π-A d'una monocapa de Langmuir, i representació esquemàtica dels diferents estats d'agregació (G: gas, LE: líquid expandit, LC: líquid condensat, S: sòlid).

En el marc d'aquesta tesi, s'han adreçat diferents aspectes relacionats amb el camp de les monocapes de Langmuir, com són la quiralitat en monocapes, el flux de monocapes o l'ús de monocapes com a sistemes model de membranes biològiques.

1.2 Objectius

Els objectius principals d'aquesta tesi es poden resumir en els següents punts:

1. Caracterització de monocapes de Langmuir d'un derivat azobenzènic que forma dominis condensats en la interfase aire/aigua, i inducció i selecció d'una quiralitat orientacional dins dels dominis condensats, mitjançant l'ús d'una força quiral química i una força quiral física.

2. Estudi del reconeixement heteroquiral en monocapes de Langmuir, degut a la interacció de dos enantiòmers quirals d'un derivat d'azobenzè.

3. Utilitzar la microfluídica bidimensional per tal d'estudiar diferents processos de transport que tenen lloc en la interfase entre dues monocapes que co-flueixen per un canal.

4. Estudiar la formació de perfils de velocitat anòmals durant el flux de monocapes, i caracteritzar la formació d'un flux de retorn en els canals microfluídics, relacionant-lo amb els perfils de velocitat obtinguts.

5. Adaptar els protocols utilitzats en la microfluídica bidimensional, per tal d'estudiar la inserció i la difusió d'una proteïna en una monocapa de fosfolípids

2. Monocapes de derivats azobenzènics

2.1 Introducció

Les monocapes de derivats azobenzènics han estat àmpliament estudiades degut a la seva potencial aplicació en el camp dels aparells fotomecànics, com a interruptors òptics, o en l'emmagatzemament d'imatge. En aquesta secció, es fa una caracterització de les monocapes de Langmuir de dues substàncies amfifíliques insolubles, el 8Az5COOH i el (*R/S*)-7'Az3 (en notació abreujada), que són dos derivats d'azobenzè. Aquestes molècules, degut a la presència del grup azobenzè, són fotosensibles, i quan s'exposen a llum UV se'ls indueix una isomerització de la forma *trans* a la *cis*. D'altra banda, quan la forma *cis* es exposada a la llum visible, o simplement degut a una relaxació tèrmica, la molècula isomeritza a la forma *trans*. Aquesta isomerització dóna lloc a canvis en les propietats de la molècula depenent de la forma isomèrica en la qual es trobi, com per exemple en l'àrea que ocupa, la conformació molecular o el moment dipolar. Com a resultat, ambdós isòmers s'organitzen de manera diferent en la interfase aire/aigua. L'isòmer *cis,* forma monocapes isòtropes que no presenten cap textura quan són observades per microscòpia d'angle Brewster (BAM), d'altra banda, l'isòmer *trans* forma mesofases birefringents. Quan la monocapa es prepara en les condicions per a que amdós isòmers siguin presents en la interfase aire/aigua, té lloc una separació de fases on es formen dominis circulars de molècules *trans*, envoltats per una matriu isòtropa de l'isòmer *cis*. Les molècules de l'isòmer *trans* s'organitzen dins del domini amb una inclinació constant respecte la normal a la interfase, i amb una variació de l'angle azimutal.

En la primera part d'aquest estudi, s'han analitzat monocapes de 8Az5COOH obtenint isotermes de compressió, que han permès una anàlisi termodinàmica de la transició de primer ordre present en el sistema, i d'altra banda s'han fet observacions mitjançant microscòpia d'angle Brewster per tal de descriure les diferents fases per les quals el sistema evoluciona, així com per caracteritzar la configuració molecular dins

dels dominis aïllats que apareixen en monocapes de la mescla fotoestacionària dels dos isòmers.

En la segona part de l'estudi, s'ha explorat el comportament de dos enantiòmers, (*R/S*), del derivat quiral d'azobenzè 7'Az3. En aquest cas, trobem que els enantiòmers purs no formen mesofases, a diferència del que caldria esperar si un pren com a referència el comportament de la molècula anàloga 8Az3COOH. En canvi, quan una mescla racèmica dels dos enantiòmers s'escampa en la interfase aire/aigua, una mesofase ordenada apareix a pressions superficials baixes, formada a partir de l'autoensamblatge dels dos enantiòmers. Aquest fenomen, representa un exemple de reconeixement heteroquiral en monocapes, on un alt grau d'ordre s'obté a partir de la interacció de dues molècules quirals complementàries.

D'altra banda, s'ha fet un estudi preliminar de l'efecte que té el 7'Az3 actuant com a dopant quiral, en monocapes fotoestacionàries de 8Az5COOH, en comparació amb un estudi fet per *Petit-Garrido et al*. amb la molècula anàloga 8Az3COOH.

2.2 Procediment experimental

En tots els casos l'aigua que constitueix la subfase és aigua pura de qualitat Millipore MilliQ, continguda en una cubeta de Tefló termostatitzada. Les solucions utilitzades es preparen amb cloroform com a dissolvent, i tot el procés es fa a les fosques quan es vol treballar amb l'isòmer *trans*, o es deixa a llum ambient si es vol treballar amb una mescla fotoestacionària dels dos isòmers. En aquest últim cas, també es pot treballar amb la solució de partida en la forma *cis* o *trans*, i un cop sobre la interfase aire/aigua s'irradia amb llum de la longitud d'ona necessària, per tal d'afavorir l'aparició de l'isòmer complementari.

Per a preparar una monocapa de Langmuir, un cop l'aigua de subfase ha arribat a la temperatura desitjada, i la balança que mesurarà canvis en la pressió superficial ha estat correctament calibrada, es van dipositant gotes de la solució determinada fins que s'arriba a la pressió de treball. Un cop la solució esta escampada en la superfície de l'aigua, es deixa un període de 10 minuts aproximadament per a que el cloroform

s'evapori, i es procedeix a la compressió de la monocapa mitjançant unes barreres mòbils si s'escau.

En experiments on l'efecte de l'agitació de la monocapa per mitja d'un vòrtex s'ha estudiat, es fa servir una cubeta circular de Delrin negre, que s'encaixa dins d'una cubeta de Tefló termostatitzada per tal de poder controlar la temperatura de la subfase. Tot el muntatge es posiciona a sobre d'un agitador magnètic reversible, que permet controlar la velocitat d'agitació en ambdós sentits. Les monocapes sota agitació es preparen dins de la cubeta circular seguint el procediment explicat en el paràgraf anterior, mentre l'aigua de subfase és agitada a velocitat constant gràcies a un nucli magnètic cilíndric recobert de Tefló.

2.3 Resultats i discussió

2.3.1 Organització mesoscòpica i estudi termodinàmic de monocapes del derivat azobenzènic 8Az5COOH

S'han obtingut isotermes de compressió de monocapes *trans* de 8Az5COOH, a diferents temperatures entre 15 i 35 °C. En les isotermes, es pot observar que la pressió superficial va augmentant a mesura que es comprimeix la monocapa, fins una pressió determinada on la monocapa pateix un canvi de fase indicat per una zona de *plateau* plana on la pressió superficial no varia. Si es continua comprimint la monocapa, s'arriba a una pressió determinada on aquesta col·lapsa, fent un pic en la isoterma.

Les imatges BAM obtingudes mostren gradients de reflectivitat en la monocapa, que es poden relacionar amb canvis espacials en la orientació molecular. A mesura que la monocapa es va comprimint, quan s'arriba a la pressió de canvi de fase les imatges BAM mostren la transició a una textura totalment diferent, on els dominis formats s'organitzen en forma de mosaic.

L'anàlisi de les isotermes per mitjà de l'equació de Clausius-Clapeyron, ha permès estimar els valors d'entropia i entalpia del canvi de fase, que s'han pogut correlacionar amb valors d'estudis similars.

Treballant amb monocapes mixtes *cis/trans*, s'ha pogut caracteritzar la textura interna d'un domini *trans* aïllat, ajustant la reflectivitat BAM a una distribució azimutal espacial determinada, utilitzant un model òptic que assumeix que la monocapa es comporta com un medi òptic uniaxialment birefringent (Figura 2).

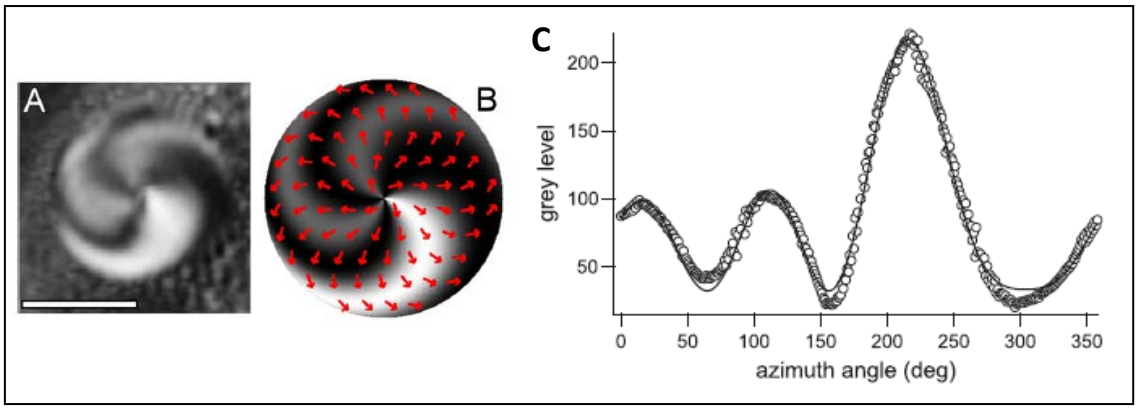

Figura 2. (A) Domini ric en isòmer *trans* del 8Az5COOH. (B)Camp azimutal proposat, i textura BAM corresponent al domini en (A). (C) Nivell de gris en funció de l'angle polar, al voltant d'una circumferència de 52.5 µm de diàmetre, centrada en el defecte central del domini. La línia és un ajust a les dades de reflectivitat.

2.3.2 Reconeixement heteroquiral en monocapes d'un derivat azobenzènic quiral

En aquest apartat s'han mesurat isotermes de compressió de monocapes *trans* dels dos enantiòmers purs, i de la mescla racèmica de dos tensioactius quirals: *R* i *S*-7'Az3.

Les imatges BAM mostren que les monocapes dels enantiòmers purs són isòtropes a totes les pressions fins al col·lapse de la monocapa, però en canvi la mescla racèmica d'ambdós presenta una textura amb regions de diferent reflectivitat que canvía amb la rotació de l'analitzador del BAM. Això, és un signe de birefringència òptica típica de fases hexàtiques, i ha estat comprovat estenent una monocapa en la forma de dominis *trans* aïllats, que presenten una textura determinada que indica la presència de fases hexàtiques (Figura 3).

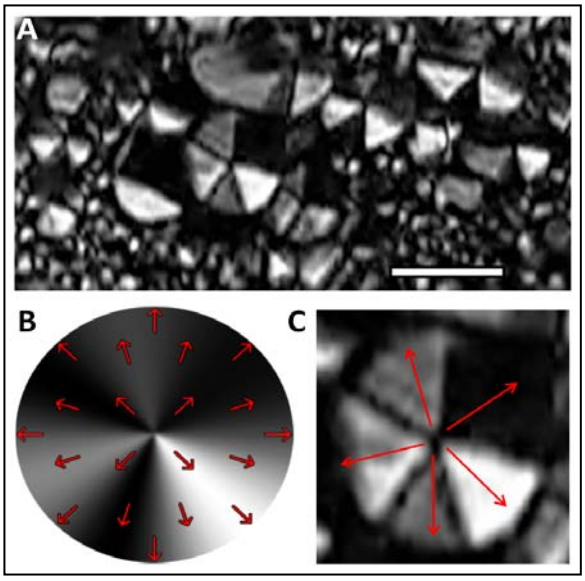

Figura 3. (A) Imatge BAM d'una monocapa de la mescla racèmica d'azobenzens quirals, on dominis aïllats *trans* estan envoltats per una matriu de *cis*. Una anàlisi òptica del patrons de reflectivitat, permet modelar l'ordre molecular (B), i permet obtenir l'orientació molecular promig en el pla. El marcador en (A) fa 100µm.

Per totes les composicions de monocapa, quan aquesta es comprimida fins passat el col·lapse, s'organitza formant dominis que contenen un número imparell de capes, amb una nanoestructura interna que s'ha estudiat amb Microscòpia de força atòmica (AFM), després de transferir-los sobre un substrat sòlid mitjançant la tècnica de Langmuir-Blodgett.

2.3.3 Inducció i selecció de quiralitat en una monocapa de 8Az5COOH

Hem estudiat la resposta de les monocapes de 8Az5COOH a l'addició d'un dopant quiral químic, i a l'acció d'una força quiral física, com és un vòrtex. Ens hem centrat en monocapes *cis/trans*, on apareixen dominis aïllats de l'isòmer *trans*, que presenten una textura tipus *doble boojum*, i són aquirals. Quan la monocapa es dopa amb una certa quantitat de modificador quiral, els dominis formats passen a tenir una textura tipus *boojum*, que presenta una quiralitat ben definida amb una distribució dels azimuts horària (*clockwise, CW*) o antihorària (*counter-clockwise, CCW*). Aquesta quiralitat, és seleccionada totalment depenent de l'enantiòmer utilitzat com a dopant (*R* o *S*) (Figura 4), i es determina calculant l'excés enantiomèric obtingut respecte el

nombre de dominis horaris (CW): $ee = \frac{2n_{CW} - n_T}{n_T} 100$, on n_{CW} representa el número de dominis quirals horaris i n_T el número total de dominis.

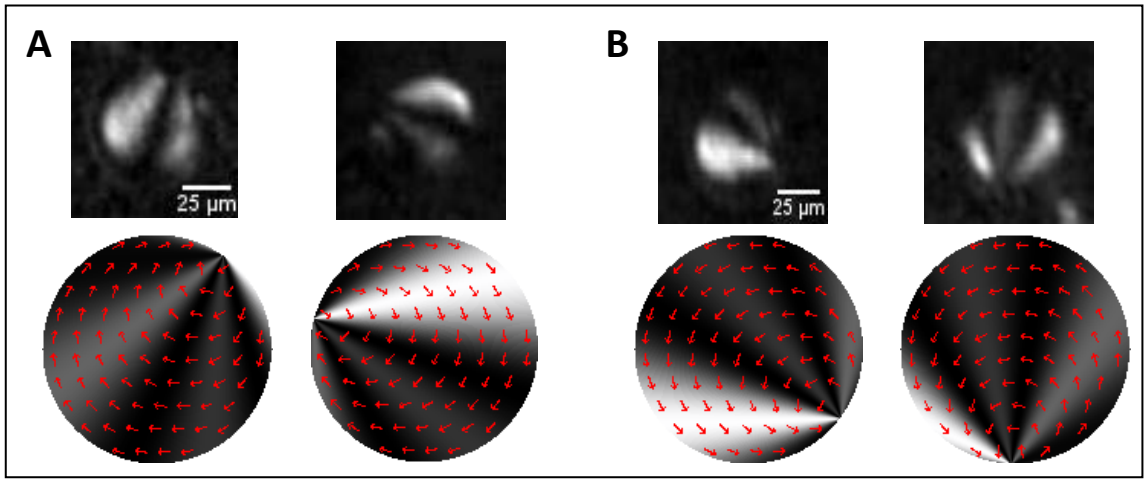

Figura 4. Imatges BAM de dominis tipus boojum CW (A), i boojum CCW (B), i esquema de l'orientació molecular en el pla, amb la corresponent textura BAM simulada.

L'efecte de l'acció d'un vòrtex present en la subfase, s'ha pogut comprovar dipositant la monocapa sota agitació, i deixant-la evolucionar. Passat un temps s'ha comptabilitzat el número de dominis que presenten una quiralitat relacionada amb el sentit de gir del vòrtex, corroborant la seva majoria.

D'altra banda, quan l'efecte del dopant quiral i el del vòrtex competeixen, es a dir, la monocapa es dopa amb el modificador quiral i s'estén sota agitació de la subfase, el seu acoblament pot ser constructiu i seleccionar totalment una certa quiralitat, o bé enfrontar-se, on es veu un clar efecte predominant del dopant quiral.

3. Microfluídica bidimensional

3.1 Introducció

La manipulació de fluxos de sistemes bidimensionals a escala submil·limètrica, representa una nova eina per al control de superfícies estructurades per a aplicacions químiques o biològiques, un cop el sistema es transfereix a un substrat sòlid. En aquest context, el flux paral·lel de dues monocapes de Langmuir és un pas crucial que involucra fenòmens de transport interficial, i fins i tot reaccions químiques.

En aquesta secció, s'han abordat diferents maneres d'incrementar la mescla i difusió de dues monocapes que flueixen paral·lelament al llarg d'un canal microfluídic de contrast de mullat, concloent que només s'aconsegueix un petit augment en la difusió entre monocapes quan es treballa amb canals poc profunds. També s'ha estudiat un procés de dissolució bidimensional, i s'ha intentat visualitzar una reacció que tingui lloc en la interfase entre dues monocapes que flueixen al llarg d'un canal.

D'altra banda, s'ha determinat el perfil de velocitats d'una monocapa fluint al llarg d'un canal de contrast de mullat, obtenint un perfil anòmal que presenta un mínim de velocitat en el centre del canal. Aquest, s'ha relacionat amb l'aparició d'un flux de retorn en la subfase quan la monocapa s'empeny, que flueix en sentit contrari al del flux superficial. S'ha demostrat que el flux de retorn creat, que altera els patrons de transport en aquests canals, depèn de la geometria del canal, i que es pot modificar canviant el nivell d'aigua present en el canal.

3.2 Procediment experimental

Per tal de realitzar els experiments de microfluídica bidimensional, on les monocapes fluiran a través d'un canal, es fabriquen diferents tipus de circuit, amb materials com Delrin o llautó. En els experiments on un canal amb certa profunditat és necessari, la pista es grava mecànicament en el material, però en el cas d'utilitzar

circuits plans de contrast de mullat, es fan servir diferents tècniques fotolitogràfiques i d'autoensamblatge de molècules per tal de produir-los.

La fabricació de circuits de contrast de mullat es fa a sobre d'una placa de llautó que prèviament es poleix, i es submergeix en una solució d'àcid nítric al 50%. Després, un cop ben esbandida amb aigua MilliQ, es submergeix en una solució de nitrat de plata durant 20 segons. En aquest pas, la placa queda recoberta per una capa de plata metàl·lica, que li dona un color fosc. Un cop fet això, la placa es recobreix amb una capa de resina fotosensible (AZ1512 HS), i s'irradia amb llum UV cobrint amb una fotomàscara la part del canal que no ha de ser irradiada (la que marcarà la forma del circuit). D'aquesta manera, un cop es revela la placa, la resina que ha estat irradiada es desprèn deixant el patró que hi havia imprès en la fotomàscara, en forma de resina adherida al canal. El següent pas és fer una monocapa autoensamblada (SAM) a sobre de la plata que recobreix el llautó, submergint la placa durant 5 minuts en una solució de tiol. Aquest, confereix a la superfície de la placa un caràcter superhidrofòbic, canviant les seves propietats de mullat. Per últim, es dissol la resina que quedava marcant la forma del canal, deixant lliure la plata metàl·lica que hi ha a sota, i que és hidrofílica. D'aquesta manera, queda un canal hidrofílic on entrarà l'aigua, envoltat d'un entorn superhidrofòbic.

La preparació de monocapes es fa segons el protocol descrit en la secció anterior, utilitzant una cubeta de Tefló on s'encaixa el circuit a utilitzar, creant així tres compartiments independents només connectats per l'aigua de subfase, on es poden dipositar monocapes de diferent naturalesa.

3.3 Resultats i discussió

3.3.1 Augment dels processos de difusió i mescla entre monocapes que co-flueixen per un canal

El coeficient de difusió d'una espècie fluorescent present en una monocapa de lípids, es pot mesurar quan aquesta co-flueix al llarg d'un canal amb una monocapa no-fluorescent. Per mitjà d'imatges de microscòpia de fluorescència, que s'obtenen al llarg del canal, s'observa com la interfase entre les dues monocapes es va eixamplant a

mesura que les molècules fluorescents van difonent d'una monocapa a l'altra. A partir d'aquestes imatges, es poden obtenir perfils d'intensitat de fluorescència al llarg del canal, i, suposant que la intensitat de fluorescència és lineal amb la concentració d'espècie fluorescent, es poden obtenir també perfils de concentració al llarg del canal. Aquests, s'ajusten a l'equació de difusió de Fick, i havent mesurat el temps de difusió experimentalment, es pot calcular el coeficient de difusió (Figura 5).

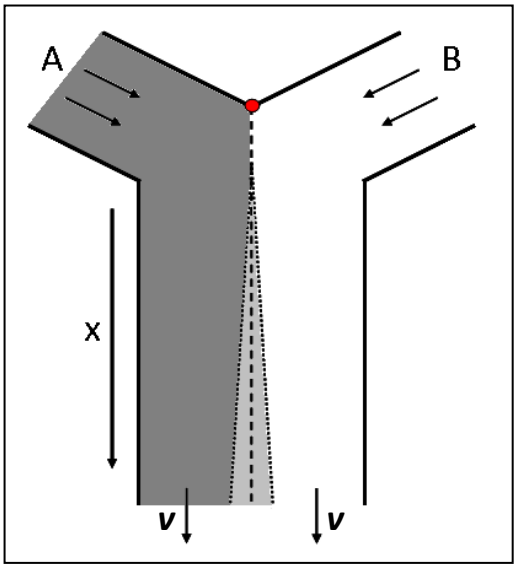

Figura 5. Esquema del sistema de co-flow de monocapes. Les monocapes A i B, es troben en el punt marcat pel cercle vermell, i que correspon al *t=0* de l'experiment, i flueixen de forma paral·lela al llarg del canal amb una velocitat ***v*** determinada. La línia central representa la interfase entre les dues monocapes, i les línies puntejades, la zona de difusió que es va eixamplant a mesura que les monocapes avancen pel canal. El temps de difusió *t* a diferents posicions del canal, es calcula mitjançant ***t=x/v***.

Prenent la situació anteriorment descrita com a punt de partida, s'ha intentat augmentar la difusió entre les dues monocapes creant una situació on el gradient de concentració sigui el més gran possible, utilitzant dues monocapes pures diferents, una d'elles fluorescent, per a calcular el coeficient d difusió. En aquest cas, el valor que s'ha obtingut és comparable al que s'obté en el cas anterior, és a dir, no hem aconseguit una millora en la difusió del sistema.

Una altra estratègia que s'ha abordat per tal d'aconseguir augmentar la difusió en el sistema, consisteix en utilitzar canals amb forma de serpentí. En aquest cas, s'han utilitzat dues monocapes de lípids, una d'elles dopada amb un petit percentatge de sonda fluorescent, i s'ha fet la mateixa mesura del coeficient de difusió, donant, en

aquest cas, valors dues vegades més grans. Pe tant, l'ús de canals amb forma de serpentí, ha ajudat a augmentar la difusió en el sistema.

D'altra banda, s'han introduït contraccions i expansions en la geometria dels canals per tal d'estudiar-ne el seu efecte en la difusió o la mescla de monocapes. Junt amb els canvis en la geometria del canal, també s'ha modulat la seva profunditat, i s'ha pogut relacionar amb la formació de vòrtexs en les cantonades després d'una expansió o d'una compressió del canal. Un cop trobades les condicions en les que un vòrtex és format en cada cantonada quan una monocapa entra dins d'una cambra d'expansió, s'ha fet un experiment on la interfase entre les dues monocapes entra dins del vòrtex, augmentant així la línia de contacte entre elles, i, per tant, augmentant la difusió.

Finalment, s'ha seguit un procés de dissolució en dues dimensions, on una monocapa que forma dominis condensats (tipus sòlid), co-flueix pel canal juntament amb una monocapa expandida (tipus líquid). En aquest cas, s'ha visualitzat mitjançant BAM, a temps real, la dissolució dels dominis condensats per part de la fase expandida.

A part, s'han intentat diverses reaccions a la interfase de dues monocapes, donant sempre com a resultat un bloqueig de la mateixa reacció per part del producte, que queda en la interfase entre les dues monocapes impedint el pas dels reactius.

3.3.1 Mesura del flux de retorn induït per gradients de tensió superficial, en microcanals oberts.

Hem observat la creació d'un flux de retorn en l'aigua de subfase, com a resposta al flux d'una monocapa que s'empeny per a que flueixi al llarg d'un canal de contrast de mullat. La observació s'ha fet per mitja de la microscòpia de fluorescència, i ha permès realitzar mesures de velocitats de partícules traçadores presents en l'aigua de subfase i en la monocapa. Així, s'ha observat com el flux de retorn es crea en sentit contrari al flux de la interfase, per tal de compensar la diferència de pressió hidrostàtica que apareix entre els extrems del canal, en arrossegar la monocapa amb l'ajuda d'unes barreres mòbils. Aquest flux de retorn, que altera els patrons de transport en el canal, s'ha relacionat, amb l'ajuda d'un simple model, amb el perfil de velocitats anòmal que s'obté en aquest tipus de canals, i que presenta un mínim central (Figura 6).

Finalment, hem demostrat que el flux de retorn depèn de la geometria del canal, que hem pogut modular canviant el nivell d'aigua en els canals de contrast de mullat.

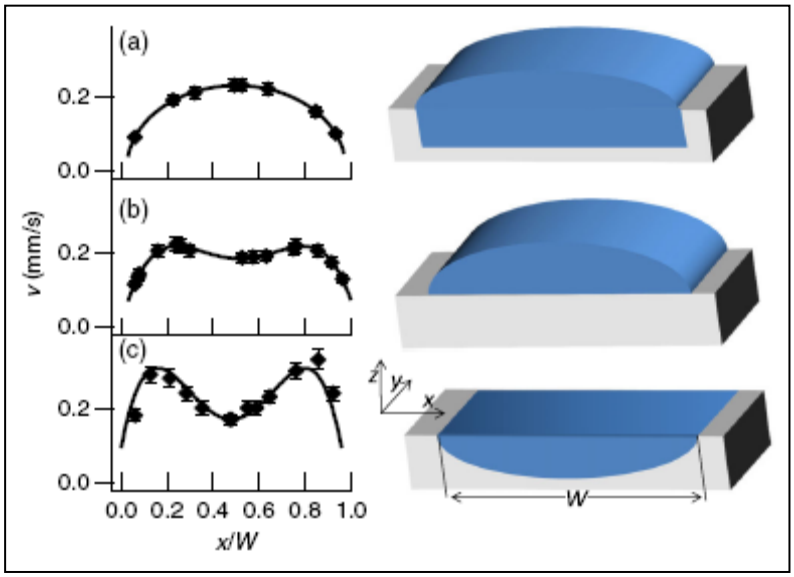

Figura 6. Perfils de velocitat mesurats per tres geometries de subfase diferents (a)-(c). A la dreta de cadascun, es representa una secció perpendicular de la subfase, que es troba continguda lateralment gràcies a una superfície superhidrofòbica.

4. Interacció proteïna-monocapa lipídica

4.1 Introducció

En les últimes dècades, les membranes biològiques han estat objecte d'estudi per part de la comunitat biofísica, degut a la seva rellevància i implicació en una gran varietat de processos cel·lulars. En termes generals, les membranes biològiques estan constituïdes per una bicapa de lípids amb proteïnes, que regulen el transport selectiu de nutrients, ions, etc. Per tal d'estudiar aquestes membranes s'utilitzen diferents sistemes model, essent les monocapes de Langmuir un dels més freqüentment aplicats. En concret, en aquesta secció s'ha estudiat l'adsorció d'una proteïna en una monocapa de fosfolípids. La proteïna utilitzada és un fragment de la Src, una proteïna involucrada en processos cancerosos en humans.

4.2 Procediment experimental

El procediment experimental que s'ha seguit per tal de dipositar les monocapes en la interfase aquosa (tampó/aire en aquest cas), és el mateix descrit en la secció 2.2.

Un cop la monocapa està preparada, s'injecta una solució de proteïna (MyrUSrc) en la subfase, mentre s'extreu la mateixa quantitat de líquid per tal de no fer canviar el nivell de líquid que hi ha en la cubeta, i, per tant, no falsejar la lectura de la pressió superficial. Un cop la proteïna està injectada, el sistema es deixa evolucionar mentre es recullen dades de pressió superficial amb el temps, per a detectar l'adsorció de la proteïna en la monocapa de lípids.

4.3 Resultats i discussió

Per tal d'estudiar l'activitat superficial de la proteïna en una subfase de tampó de fosfat, s'ha enregistrat una corba de pressió superficial enfront del temps, on veiem que en una interfase lliure de monocapa la proteïna tendeix a adsorbir-se. Com que la

proteïna es manté adsorbida a la interfase tampó/aire, i no es desorbeix amb el temps ni canviant el tampó de subfase per tal d'extreure tota la proteïna present en el bulk, s'han enregistrat isotermes de compressió.

S'ha estudiat la morfologia de la proteïna en la interfase, transferint-la a una placa de vidre net mitjançant la tècnica de Langmuir-Blodgett, i analitzant-la per AFM. Les imatges revelen la presència d'agregats esfèrics, que tenen una mida comparable amb els agregats que es detecten en solució, que probablement apareixen per la interacció de la proteïna amb ADN que s'han co-purificat durant l'expressió de la proteïna.

D'altra banda, també s'ha explorat l'afinitat de la proteïna per en una monocapa de lípids present en la interfase, estudiant-ne la seva adsorció. En aquest cas, la corba de pressió superficial enfront del temps mostra una cinètica d'adsorció més ràpida que en el cas d'una interfase lliure de lípids. Per a visualitzar la proteïna adsorbida en la monocapa, aquesta s'ha dopat amb un petit percentatge de sonda fluorescent creant una monocapa fluorescent homogènia, on van apareixent agregats foscos a mesura que la proteïna s'hi va adsorbint (Figura 7). També s'ha intentat l'estratègia complementària utilitzant una proteïna marcada fluorescentment, que crea agregats fluorescents quan s'insereix en la monocapa. Amb aquesta configuració, s'han enregistrat isotermes de compressió, i s'ha transferit sobre un substrat sòlid amb la tècnica de Langmuir-Schaefer. En aquest cas, les imatges AFM també mostren la presència d'agregats esfèrics.

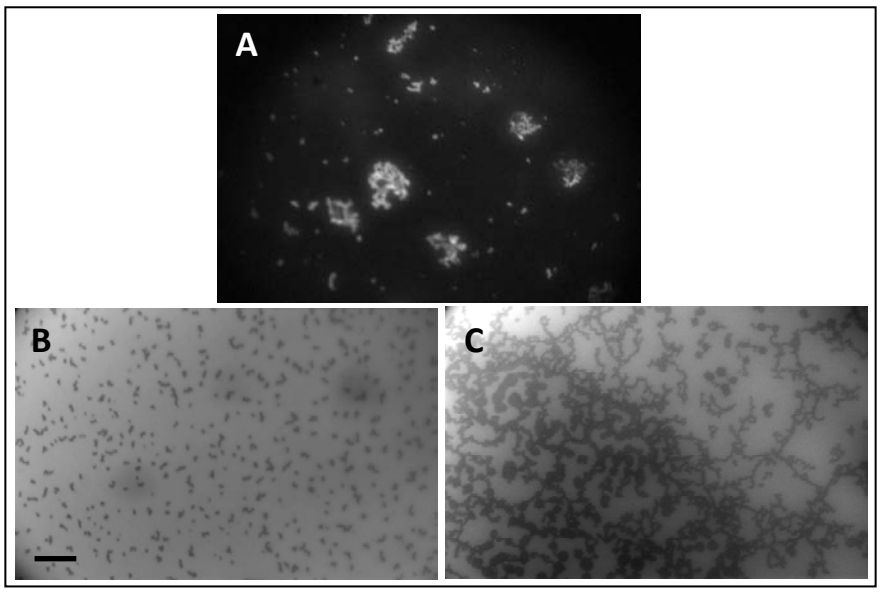

Figura 7. Imatges de microscòpia de fluorescència d'una monocapa de lípids amb agregats de proteïna fluorescent adsorbida (A), i imatges d'una monocapa de lípids dopada amb sonda fluorescent, amb agregats de proteïna no fluorescent adsorbida, després d'una i tres hores d'inserció (B i C respectivament). La barra d'escala equival a 50μm.

4. Conclusions

- Les isotermes de la monocapa *trans* del 8Az5COOH mostren una gran dependència del canvi de fase amb la temperatura, en comaparació al compost homòleg 8Az3COOH, el que ha permès una anàlisi termodinàmica del canvi de fase aplicant l'equació de Clausius-Clapeyron, determinant els valors de l'entalpia i entropia del canvi de fase. L'anàlisi de monocapes mixtes *cis/trans* de 8Az5COOH, que mostren una separació de fases on apareixen dominis aïllats de l'isòmer *trans* envoltat d'una fase rica en isòmer *cis*, suggereix que la tensió de línia existent entre les dues fases és menor que en el cas del compost homòleg 8Az3COOH.

- En absència d'una influència quiral, els dominis *trans* d'una monocapa mixta *cis/trans* de 8Az5COOH són aquirals. En presència d'una petita quantitat del derivat azobenzènic quiral 7'Az3, la quiralitat orientacional dins d'aquests dominis pot ser seleccionada. A més, quan la influència quiral aplicada és un vòrtex en la subfase, apareix un excés enantiomèric de dominis amb una quiralitat determinada, que està directament relacionada amb el sentit de rotació del vòrtex aplicat.

- Les monocapes del compost quiral (R/S)-7'Az3 no formen mesofases quan s'utilitza els enantiòmers purs, però si la monocapa es prepara amb una mescla racèmica d'ambdós enantiòmers, té lloc un procés de reconeixement heteroquiral que resulta en la formació d'una mesofase. La naturalesa hexàtica d'aquesta mesofase es caracteritza analitzant la textura interna dels dominis aïllats rics en isòmer *trans*. Per a totes les composicions, quan la monocapa es comprimida per sobre de la pressió de col·lapse, s'organitza formant dominis submil·limètrics birefringents composts per un número imparell de capes, i que tenen una microestructura ben definida que s'ha analitzat per AFM.

- En el camp de la microfluídica bidimensional s'ha estudiat la difusió entre monocapes que co-flueixen per un canal, obtenint un increment en el valor del coeficient de difusió utilitzant circuits curvilinis, i introduint vòrtexs en el sistema. En canvi, augmentar el gradient de concentració entre les dues monocapes involucrades, no ha produït un efecte detectable en els coeficients de difusió mesurats. D'altra banda, s'ha visualitzat un procés de dissolució bidimensional, que segueix el model de dissolució clàssic. Finalment, s'ha intentat visualitzar una reacció en la línia de contacte entre dues monocapes, trobant sempre un problema degut a la baixa dimensionalitat del sistema; el producte de la reacció impedeix la difusió dels reactius per a que la reacció continuï.

- S'ha estudiat el flux de monocapes degut a gradients de tensió superficial, en microcanals oberts. S'ha determinat que l'arrossegament de la interfase i el confinament lateral, resulten en la formació d'un flux de retorn en la subfase, que flueix en sentit contrari al del flux superficial. Aquest flux de retorn, depèn de la geometria del canal, i la seva forma s'ha relacionat amb els perfil de velocitat interficials mesurats, combinant un model simple amb mesures de velocimetria.

- El caràcter tensioactiu d'agregats de proteïna miristoilada, s'ha estudiat en absència i presència d'una monocapa de fosfolípids en la interfase, mostrant una tendència dels agregats a adsorbir-se en aquesta irreversiblement. D'aquesta manera s'han establert els protocols de treball per a futurs experiments amb la proteïna pura.

AGRAÏMENTS

Voldria agrair per igual a tothom que ha participat d'alguna manera en la realització d'aquesta tesi. Al meu director, el Dr. Jordi Ignés, i als Drs. Josep Claret i Francesc Sagués, per guiar-me en aquesta etapa. A tots els companys i companyes del departament per les bones estones que hem passat. En especial al Sergi, el segon millor inventor de cançons del món (si, si, el segon), per tots el moments compartits, que no han estat pocs, i per ser com ets! Als membres del taller mecànic, que m'han facilitat molt la feina, gràcies! A la meva família i al Michl, per creure en mi. Gràcies també als moments inoblidables viscuts amb "les peroles", a les cerveses després de trapezi i de ballar, a les caminades per la muntanya o les excursions al pantà, a les converses que m'han inspirat i les que m'han consolat, a tots els riures... però sobretot, a tots els que heu fet possibles aquests moments, que m'han ajudat a superar els trams més durs d'aquesta tesi, moltes gràcies!